Design and implementation of an AFM head with tapping mode laser signal demodulation

DIPLOMARBEIT

Ausgeführt zum Zwecke der Erlangung des akademischen Grades eines
Diplom-Ingenieurs (Dipl.-Ing.)

unter der Leitung von

Univ.-Prof. Dr.sc.techn. Georg Schitter

Univ.-Ass. Dipl.-Ing. Mathias Poik
Univ.-Ass. Dipl.-Ing. Thomas Hackl

eingereicht an der
Technischen Universität Wien
Fakultät für Elektrotechnik und Informationstechnik
Institut für Automatisierungs- und Regelungstechnik

von
Peter Traunmüller
Matrikelnummer: 1326142

Wien, im März 2024

Technische Universität Wien
Karlsplatz 13, 1040 Wien, Österreich

Danksagung

Thanks to all the people having enabled this work, if you're reading this you're most certainly one of them.

Thomas Hackl is the main facilitator of all practical implementations, theoretical aspects and luscious inputs. A special thanks to Johannes Wiesböck for sharing his analog and other knowledge. Viktoria Groiß is to be panegyrised for taking the time to read the complete script and educating me on what an infinitive is.

Thanks to Georg Schitter who has enabled this work.

Abstract

The Atomic Force Microscope (AFM) is an instrument with a wide variety of applications, both in scientific as well as industrial contexts. A sharp tip mounted on a small cantilever is used to sample surfaces of many different materials while measuring the resulting forces onto it. The resulting measurements can image physical structures within the nanometer range to investigate and manipulate sample properties.

Due to the increasing sampling frequency of AFM topography measurements caused by the availability of high resonance frequency cantilevers, an increasing burden lays on the demodulation of the resulting output signal from dynamic measurement methods such as the tapping mode. Most commercially available AFM setups use an optical-based cantilever deflection readout, in which case the transimpedance amplifier converts the output current from a reflected laser beam shone onto a photodiode array into a voltage for demodulation.

An external lock-in amplifier is most commonly used for this task, for which there are implementations both in the analog as well as the digital realm. Due to the limited bandwidth, high complexity and additional noise sources, finding alternatives is an active field of research.

By directly demodulating a tapping mode laser signal within a variable gain amplifier, this works goal is to design and evaluate a novel approach for an AFM head cantilever deflection readout. This achieves a high scanning bandwidth while keeping external noise sources small and avoids usage of an external lock-in amplifier.

A full analysis of the measurement path including a redesign of relevant parts is conducted and the newly conceived setup is fully evaluated and specified. Measurements on biological and other samples are undertaken to put the final implementation into a real world application and ensure comparability with other designs.

Kurzfassung

Das Rasterkraftmikroskop (AFM) ist ein Instrument welches in einem weiten Spektrum an Anwendungsfällen, sei es für wissenschaftliche oder industrielle Anforderungen, zum Einsatz kommt. Eine dünne Spitze (tip), welche aus einem Kragarm (cantilever) hervorsteht, wird benutzt um die Oberfläche von Proben abzufahren während die darauf resultierende Kraft gemessen wird. Die daraus ableitbaren Messungen können eine horizontale Auflösung im Nanometerbereich aufweisen, um damit Probeneigenschaften zu messen und beeinzuflussen.

Die zunehmenden Abtastfrequenzen von AFM für Topografiemessungen, begünstigt durch die höhere Verfügbarkeit von Kragarmen mit höheren Resonanzfrequenzen, bürdet der Demodulation des Ausgangssignals von dymanischen Messmethoden, wie der des Tippmodus (tapping mode), zusätzliche Gewichtung auf. Hierfür wird in den meisten Fällen ein Trägerfrequenzverstärker (lock-in amplifier) verwendet, welcher sowohl digital als auch analog realisiert werden kann. Die meisten kommerziell verfügbaren AFM basieren auf einer optischen Auslesung der Kragarmauslenkung (cantilever deflection). Ein Transimpedanzverstärker zur Konvertierung des Ausgangsstromes einer Photodiodenmatrix bedingt durch einen reflektierten Laserstrahl in eine Spannung wird herangezogen, um diese der Demodulation zuzuführen.

Bedingt durch deren limitierte Bandbreite, hohen Komplexitizätsgrad und die zusätzlichen Rauschquellen, ist die Erforschung von Alternativen zu Trägerfrequenzverstärkern ein aktives Feld der Forschung.

Die direkte Demodulation eines Tippmoduslasersignals mittels eines Verstärkers mit variablen Transimpedanzwiderstand (variable gain amplifier) ist der Kern dieser Arbeit, welche sich dem Entwurf und Evaluation dieser neuartigen Kragarmauslenkungsmessung für einen AFM Kopf widmet. Diese Methode erreicht eine hohe Abstastfrequenz, hält das Messrauschen niedrig und vermeidet den Einsatz eines Trägerfrequenzverstärkers. Eine vollständige Analyse des Messpfades mit einer Neuentwicklung von relevanten Teilen wird durchgeführt und der resultierende neuartig konzipierte Aufbau wird vollständig evaluiert und spezifiziert. Messungen an biologischen Proben und Referenzstrukturen werden durchgeführt, um das final implementierte Design einer echten Anwendung auszusetzen und eine Vergleichbarkeit mit anderen Lösungsansätzen zu ermöglichen.

Contents

1 Introduction **1**
1.1 Goal of This Thesis . . . 3
1.2 Outline . . . 3

2 State of the Art **4**
2.1 Cantilever Deflection Readout . . . 5
2.1.1 Capacitive . . . 5
2.1.2 Interferometric . . . 5
2.1.3 Optical Beam Deflection (OBD) . . . 6
2.1.4 Piezo Based . . . 6
2.2 Topography Measurement Modes . . . 7
2.2.1 Contact . . . 8
2.2.2 Non-Contact . . . 8
2.2.3 Tapping . . . 8
2.3 Tapping Mode Demodulation . . . 9
2.3.1 OBD Transimpedance Amplifier (TIA) Bandwidth and Noise . . . 9
2.3.2 Translinear Amplifier (TLA) . . . 11
2.3.3 Lock-In Amplifier . . . 11

3 Theoretical Background **14**
3.1 Dynamic AFM . . . 14
3.1.1 Tip to Sample Interaction . . . 15
3.1.2 Cantilever . . . 15
3.1.3 Oscillation Amplitude and Phase . . . 16
3.1.4 Four Quadrant Photo Detector (QPD) . . . 17
3.1.5 Transimpedance Amplifier (TIA) . . . 18
3.2 Sample Preparation . . . 19
3.2.1 Substrates . . . 19

3.2.2 Immobilisation 20
3.3 Noise Sources 21
3.3.1 Mechanical Noise 21
3.3.2 Laser Source Noise 21
3.3.3 OBD Noise 22
3.4 Voltage Controlled Resistor (VCR) 23
3.4.1 Integrated Circuit (IC) VCR 23
3.4.2 Field Effect Transistor (FET) VCR 24
3.4.3 Photoresistor VCR 25
3.4.4 Summary 26

4 Proposed System **27**
4.1 Optical Path 27
4.1.1 Driver 28
4.1.2 Light Path 28
4.2 Demodulation 30
4.2.1 VG-TIA 30
4.3 Proposed system Overview and Requirements 33

5 System Design and Integration **34**
5.1 Concept 34
5.2 Laser and Optical Path Implementation 35
5.2.1 Laser Driver 35
5.2.2 Laser Setup 35
5.3 QPD Circuitry 37
5.4 TIA with Variable Gain 37
5.4.1 VG-TIA Implementations 38
5.5 $2^{\text{nd}}/4^{\text{nd}}$ Order Low-Pass 43
5.6 Subtracting TIA 43
5.6.1 Dedicated Op-Amp 44
5.6.2 Current Mirror 44

6 Evaluation & Results **46**
6.1 System Characterisation 46
6.1.1 Controlling the Transimpedance Gain 50
6.1.2 Fixed Gain Bandwidth 50
6.1.3 Variable Gain Bandwidth 51
6.1.4 Subtractor VG-TIA Output Linearity 52
6.1.5 Summary 53
6.2 System Evaluation 53
6.2.1 Surface Topography Reference Measurement 54
6.2.2 Biological Sample Measurement 55
6.2.3 Evaluation Summary 56

7 Conclusion **58**
7.1 Outlook 59

Appendix **67**
1 Prototype schematics A 67
2 Prototype schematics B 77
3 Eidesstattliche Erklärung 86
4 Einverständniserklärung zur Plagiatsprüfung 86

List of Figures

1.1 AFM typical block diagram for a 1D movement in the Z axis (adapted from [9]). 2

2.1 Picture of an AFM head from a *Bruker MultiMode V* with the laser path for an optical beam deflection readout. 4

2.2 Cantilever deflection readout based on a micromachined cantilever with integrated capacitive readout detection; (a) shows the readout principle while (b) is a micromachined cantilever with such a capacitive plate shown (adapted from [28]). 5

2.3 Optical readout approaches for cantilever deflection; (a) shows an Fabry-Pérot interferometric sensor (adapted from [26]); (b) shows the most common OBD with a four quadrant photo detector readout (adapted from [23]). 6

2.4 (a) shows a strain gauge sensor added to the cantilever in a bridge configuration (adapted from [24]); (b) shows a piezoelectric tuning fork with attached probe (adapted from [25]). 7

2.5 The three most widely used measurement modes for surface morphology measurements with AFM with the cantilever movement direction and its tip path indicated (adapted from [37]). 8

2.6 (a) TIA built around an operational amplifier with an attached photo diode and the current I resulting from the incoming irradiation converted via the gain resistor R to an output voltage V_{out}. (b) is the same circuit including parasitic capacitances C_{PD}, C_{diff}, C_{wire} and C_M as well as the feedback capacitance C_f. (adapted from [43]). 10

2.7 (a) The oscillating cantilever reflects more light to either the top two QPD cells A&B or the bottom two C&D; (b) TLA readout circuit with a MOSFET based current mirror and an ideal op-amp based TIA; (c) Is a plot of the two sinusoidal currents with an offset and their 180° phase shift shown in addition with their difference fed into the TIA. (adapted from [34]). 11

2.8 Lock-in amplifier functional diagram incl. phase and amplitude calculation (adapted from [50]). 12

3.1 Total tip to sample interaction forces modelled using Lennard-Jones potential for molecular interaction forces (adapted from [9]). 15

3.2 Triangular cantilever top and side view with its mechanical dimensions and tip radius (adapted from [53] [55]). 16

3.3 Dynamic AFM with exitation and output waveforms pictured. The amplitude and phase change of the cantilever oscillation due to different types of surface to sample interactions is shown in yellow [38]. 17

3.4 (a) QPD with each quadrant and output current to show in (b) the small signal equivalent circuit for a QPD and the corresponding currents (adapted from [57]). 18

3.5 Non-inverting closed-loop gain for a TIA with parasitic capacitance C_S and the feedback capacitance C_f with the corresponding noise gain bode plot (adapted from [58]). 19

3.6 Muscovite surface AFM image showing the $AlO3^+$ and $SiO4^+$ hexagonal rings with bridges created by basal oxygen atoms [60]. 20

3.7 Circular shape of DNA immobilised on a mica substrate with a cruciform extrusion indicated with an arrow [62]. 20

3.8 Deflection noise density depending on the laser output power. Above a threshold, the noise level increases significantly above the theoretical photo diode (PD) shot noise, which is caused by the mode hopping of the laser [23]. 22

3.9 PG-TIA with integrated multiplexer for two different gain settings [66]. 23

3.10 Drain current I_D in relation to the drain to source voltage V_{DS} of a n-channel JFET for different gate to source voltages V_G [68]. 24

3.11 Integrated VCR with (a) a light source; (b) a photoresistor and (c) a photo-FET [71]. 26

4.1 Closed loop laser driver circuitry with current and power control; (a) shows a current-controlled op-amp implementation with a laser diode LD and a gain resistor R; (b) is a power-controlled circuit with an integrated photo diode PD providing feedback FB from the LD amplified with the gain resistor R. 28

4.2 Laser path simulation with second focusing lens added to decrease the spot size of the QPD illumination in order to be able to increase the sensitivity. Beginning from the left, the first lens is collimating the highly divergent diode laser beam, while the second is focusing it onto the cantilever. On the bottom half a visual representation of the beam with the AFM components is shown for reference [75][45]. 29
4.3 Adding a VCR to the TIA feedback path enables the TIA gain to be dynamically adjustable. 30
4.4 (a) State-of-the-art AFM setup with the QPD output current amplified and converted to a voltage by a TIA and demodulated and filtered by a lock-in amplifier; (b) Implementation of a novel laser signal demodulation with a VG-TIA and low-pass filter instead of the fixed gain TIA and lock-in amplifier. 31
4.5 Proposed AFM system design. The Z axis piezoelectric actuator induces a forced oscillation into the cantilever at or near its own resonance frequency, which is then picked up as a lateral movement on the QPD. The resulting current can be demodulated via the VG-TIA and low-pass filter. 33

5.1 Laser path with diode laser output on the left being collimated and focused to have the focal point on the backside of the cantilever before being reflected onto the QPD. 35
5.2 Combined closed loop laser driver with power or current control. . . . 36
5.3 Laser path setup with the three main points for mechanical path adjustments. 36
5.4 Microscope image of a triangular cantilever with the ideal laser position for a not perfectly focussed beam indicated in red and the length and width dimensioned. 37
5.5 Schematical representation of the setup with a VG-TIA and measured signals for reference after each block of the system. 38
5.6 Prototype PCB implementing the five different VG-TIA as well as the laser driver, QPD reference and power management. 39
5.7 VG-TIA implemented with an integrated multiplexing circuit as programmable gain transimpedance amplifier. 39
5.8 n-channel JFET with supporting subtractor op-amp circuit forming a VG-TIA. 40
5.9 Modulation of one of the two gain resistors with a galvanically isolated LDR to implement a VG-TIA. 41
5.10 MOSFET based VG-TIA with the characteristic T-shaped feedback network shunting parts of the input current to ground. 42
5.11 42
5.12 Low-pass filter in a Sallen-Key topology with switchable resistors to vary its cutoff frequency. 43
5.13 Prototype for the two subtracting TIA implementations; (A) shows a dedicated op-amp based subtractor VG-TIA; (B) is a current mirror with an attached VG-TIA. 44

5.14 Subtracting TIA implemented with two VG-TIAs and a dedicated op-amp based subtractor circuit with additional voltage amplification. 45
5.15 Subtractor TIA with current mirror based on the TLA design. 45

6.1 Picture of a *Bruker MultiMode V* AFM setup including attached microscope for visual cantilever adjustion. 47
6.2 Connections between the unmodified *NanoScope 6* AFM controller and the newly implemented VG-TIA and associated parts. The connection between the waveform generator and laser driver is for testing and not used during normal scanning operation. 48
6.3 Bandwidth evaluation setup for VG-TIA and laser driver measurements. 49
6.4 VG-TIA gain plotted as a function of the permittable input voltage range. 50
6.5 Setup for measuring the VG-TIA bandwidths; (a) shows the fixed gain bandwidth; (b) evaluates the variable gain bandwidth. 51
6.6 With the variable resistor set to constant gain, the bandwidth of the VG-TIA is plotted in relation to a frequency-modulated laser current. . 51
6.7 Bode plot for the variable gain bandwidth measured with a constant laser output. 52
6.8 Evaluation of the proportionality between the laser amplitude, which is proportional to the cantilever oscillation amplitude, and the filtered output voltage for both MOSFET based subtractor VG-TIA. 53
6.9 Camera view of the laser beam focused on the back of a cantilever. . . 54
6.10 Platinum coated calibration grating, measured with the novel VG-TIA laser signal demodulation. The topography is shown on the left and the deflection measurement error on the right. 54
6.11 Zoomed-in measurement on one of the calibration grating pits, topography is shown on the left and the deflection measurement error on the right 55
6.12 Collagen fibre with different strands measured with topography on the left and the deflection measurement error on the right with the enlarged section from Fig.6.13 marked in red. 56
6.13 Enlarged image of a collagen fibre with D-band periodicity clearly showing on the left, deflection measurement error on the right. 56
6.14 DNA image with some of the helical strands marked with white arrows and the deflection measurement error on the right. 57

CHAPTER 1

Introduction

Atomic Force Microscopy (AFM) was invented in the 1980s by Binning *et al.* based on a scanning tunnel microscope (STM) [1]. It enables investigating sample surfaces in the scale of nanometers [2] and is a widely used tool for inspection and analysis for research as well as industry purposes [3], in metrology [4], for thermal treatment [5], imaging [6] as well as for molecular sample manipulation [7]. Advantages over other measurement methods such as transmission electron microscopy and scanning electron microscopy (SEM) like the missing necessity of vacuum and measurements with ambient temperatures and non conductive samples make it the preferred measurement method for many applications [8]. This is all done while making in situ imaging of nano indentations possible without the need of tip switching, movement of samples or area relocation [9]. With AFM-based methods a broad area of applications are known including surface morphology, electrical properties, adhesion, mechanical stimulation and others [5]. This is done by using the interaction forces between the sharp tip of a probe on the front of a cantilever and the sample surface which result in a measurable bending of such [10].

Shown in Fig. 1.1 is a typically used model of an AFM setup, implementing the cantilever with its tip moving along the surface of a sample, picking up the reflected laser signal with a four quadrant photo detector (QPD) before feeding it to the TIA which outputs a voltage to the feedback controller & amplifier [1]. A piezo actuator, which is in turn controlled by said feedback controller & amplifier, sets the distance from the tip to the sample operating the system in a closed loop [11].

Different measurement modes can be applied, most commonly used is the so called tapping mode [12], in which the cantilever is excited in its own resonance frequency and only tapping the surface of the sample in order to minimise impact and therefore

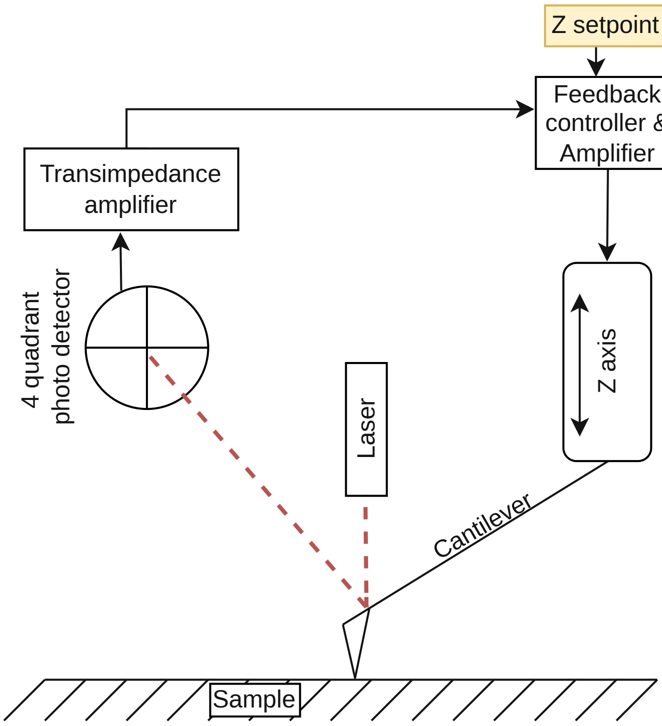

Figure 1.1: AFM typical block diagram for a 1D movement in the Z axis (adapted from [9]).

damage to the surface of the sample [13]. The oscillation amplitude is kept at a constant level by a feedback loop which keeps the tip at a defined distance to the sample [10].

Having the cantilever oscillating, the change in amplitude correlates to surface interactions, which explains the need for demodulation of the measured output [14]. This is often times done with the help of a dedicated lock-in amplifier [15] or after digitisation [16]. In this configuration the Analog to Digital Conversion (ADC) speed plays a critical and constraining role in the overall accuracy [17]. Tapping mode is often times used in conjunction with a laser-based optical readout, which measures the reflection of a laser beam pointed at the back of the cantilever [10]. Multi-segmented photo diode sensors are widely used for picking up the signal, before before current-to-voltage conversion and amplification with a Transimpedance Amplifier (TIA) [9].

High bandwidth AFM is needed for time variant sample surfaces e.g. in cells in liquid samples in order to be able to record dynamic processes [18]. Biological samples can be measured with sub-nanometer resolutions, while being in liquids such as propanol or water [19]. Measurements on those samples are often done in the tapping mode, in order to avoid damaging the surface of the sample [13]. This makes high-speed AFM, which are capable of measurements in wet and electrically conductive environments [13], an interesting topic for research e.g. [20], [21], [18] and opens the possibility for a novel analog demodulation approach for laser-based tapping mode AFM setups.

1.1 Goal of This Thesis

With the capabilities and constraints of state of the art AFM explained above, the goal of this thesis is the design, implementation and measurement of a novel direct demodulation approach for laser-based tapping mode AFM setups.

This is implemented by directly demodulating a tapping mode laser signal picked up by a QPD with a variable gain amplifier, in a unit directly added to an existing AFM setup. The aim is to achieve a high scanning bandwidth while keeping measurement noise low, without the need of external lock-in amplifiers or additional circuitry. It can also be used in liquids and only needs standard AFM with low, medium or high self-resonance frequency cantilevers, as well as being capable of being used in a constant gain mode for contact mode measurements. By the end of this thesis, an AFM head should be assembled with newly designed and evaluated analog tapping mode laser signal demodulation circuitry. It should additionally incorporate a custom laser driver circuitry for testing and specifying the implemented design. The best option, in terms of bandwidth and noise, to demodulate the signal, therefore modulating the TIA resistor has to be analysed. The final design should then be measured and compared against previous and similar works in the field. This can be summarised by

- Design and implementation of different analog demodulation designs directly in the TIA
- Analysis of the existing measurement path and addition of necessary supplementary circuitry
- Creation of a measurement setup with compatible AFM components
- Measurements and comparison to similar implementations

1.2 Outline

This work discusses the complete design and implementation of an AFM head with tapping mode laser signal demodulation. It is achieved by implementation of a Variable Gain Transimpedance Amplifier (VG-TIA) in conjunction with a low-pass filter which directly demodulates the laser signal into an output voltage proportional to the cantilever oscillation amplitude. To start, Chapter 2 lays out the state of the art of AFM, readout modes, measurements modes and tapping mode demodulation. Chapter 3 describes the theoretical backgrounds and goes into detail about sample preparation, noise sources and possible voltage controller resistor designs. The proposed system is detailed in Chapter 4, including explanations of the chosen parts for the electronics as well as the laser path. In Chapter 5, the design and implementation of the real world hardware is explained and shown, before the results are presented and discussed in the evaluation in Chapter 6. This thesis concludes with Chapter 7 in which a summary and and outlook for future works is given.

CHAPTER 2

State of the Art

This chapter explains the important aspects of AFM, the relevant readout and measurement modes as well as demodulation options. It is used in order to be able to design and implement an AFM head as shown in fig 2.1 with the proposed tapping mode laser signal demodulation and be able to compare it to other works. An in-depth analysis of the relevant physical theories and practical constraints inferring from those are given for each addressable section.

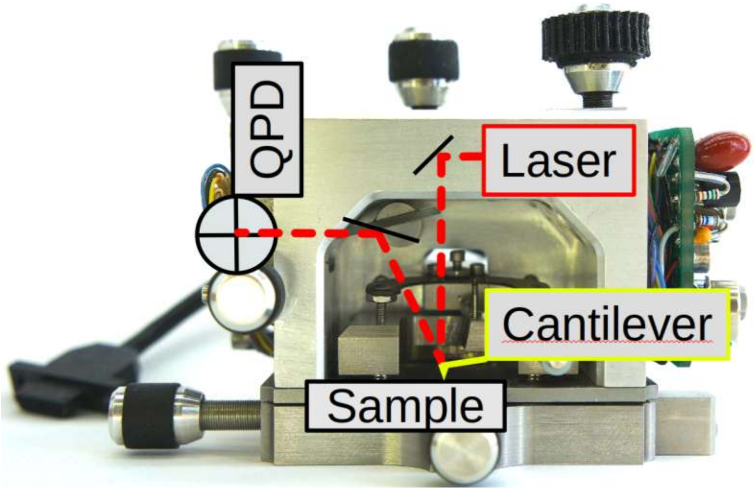

Figure 2.1: Picture of an AFM head from a *Bruker MultiMode V* with the laser path for an optical beam deflection readout.

2.1 Cantilever Deflection Readout

The fundamental task in AFM is to control the distance of the scanning probe to the sample, thus measuring its topography while scanning along its surface [1]. In STM this is done via measurement of the tunneling current [22]. In AFM this is done by keeping the interaction forces on the cantilever (=deflection) constant [1]. There are many approaches on how to measure the cantilever deflection, the most common one for commercial systems is Optical Beam Deflection (OBD) [23]. While many other cantilever deflection readouts [24] have also been successfully implemented, the ones based on the piezoelectric [25] or piezoresistive [24] effect, optical interferometry [26] as well as capacitive [27] have been taken into comparison.

2.1.1 Capacitive

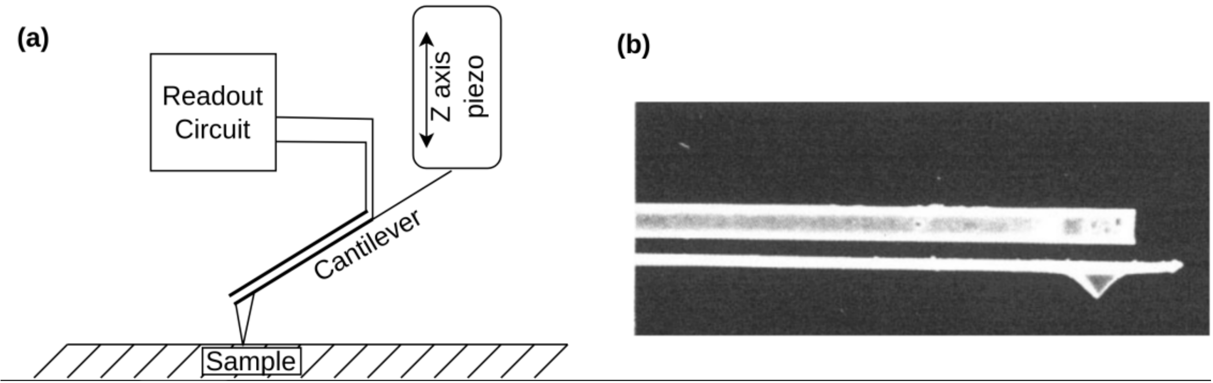

Figure 2.2: Cantilever deflection readout based on a micromachined cantilever with integrated capacitive readout detection; (a) shows the readout principle while (b) is a micromachined cantilever with such a capacitive plate shown (adapted from [28]).

By adding an electrically conductive layer on the cantilever and a second static one on top, as shown in Fig. 2.2, the changing capacitance can be used to measure physical displacement. The used cantilevers are specifically micromachined for the task and offer a low-cost option for many applications [28]. It is easy to use due to the possibility of actuating the cantilever with an applied feedback signal [27]. With different setups and constellations, thermal amplitude spectra with $400 fm/\sqrt{Hz}$ at a cantilever oscillation frequency of $243 kHz$ were measured [29].

2.1.2 Interferometric

With the addition of a sensor based on a Fabry-Pérot interferometer, the cantilever deflection readout can be done via fiber optic cables and an optic circulator [30]. This method uses the multiple beam interference between the end of the fiber cable with a dielectric reflector and the back side of a cantilever as shown in Fig. 2.3 (a) to achieve deflection noise densities of $2fm/\sqrt{Hz}$ while using regular commercially available cantilevers [26].

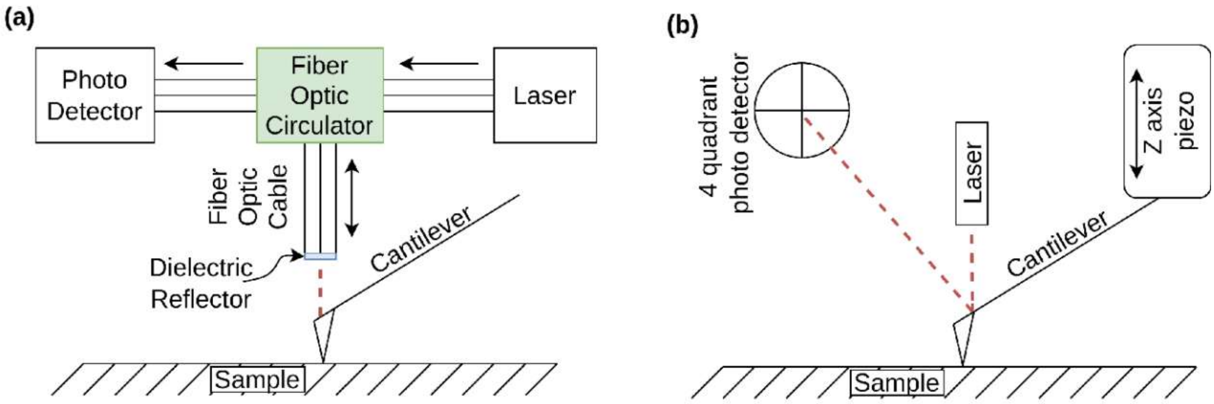

Figure 2.3: Optical readout approaches for cantilever deflection; (a) shows an Fabry-Pérot interferometric sensor (adapted from [26]); (b) shows the most common OBD with a four quadrant photo detector readout (adapted from [23]).

2.1.3 Optical Beam Deflection (OBD)

Since its first publication in 1988 by Meyer *et al.* [31], OBD has proven to be advantageous in many cases while being relatively simple to integrate. The measurement principle shown in Fig. 2.3 (b) consists of a laser beam directed at the reflective back side of a cantilever and picking up the cantilever deflection as a change in the position of the reflection on a Position Sensitive Detector (PSD) [23]. This PSD consists of two vertically stacked photo diodes and the resulting currents are often times subtracted and normalised to be independent of the total illumination of the sensor [32]. If this position sensor is implemented as a QPD, not only the force normal to the cantilever can be measured, but also the lateral force, by subtracting the left and right QPD currents, which is then considered a friction force microscope [33]. Utilising this method, a noise level for deflection below $4.5fm/\sqrt{Hz}$ at a bandwidth of $20MHz$ was achieved [34].

2.1.4 Piezo Based

Piezoresistive

A cantilever with an added strain-sensing sensors as shown in Fig. 2.4 (a) can be used as a readout technique, while being compact in size and not needing optical transparency of the measurement liquid. This strain gauge implemented in a bridge configuration can achieve a noise level of $30pm$ with a measurement bandwidth of $20kHz$ [24].

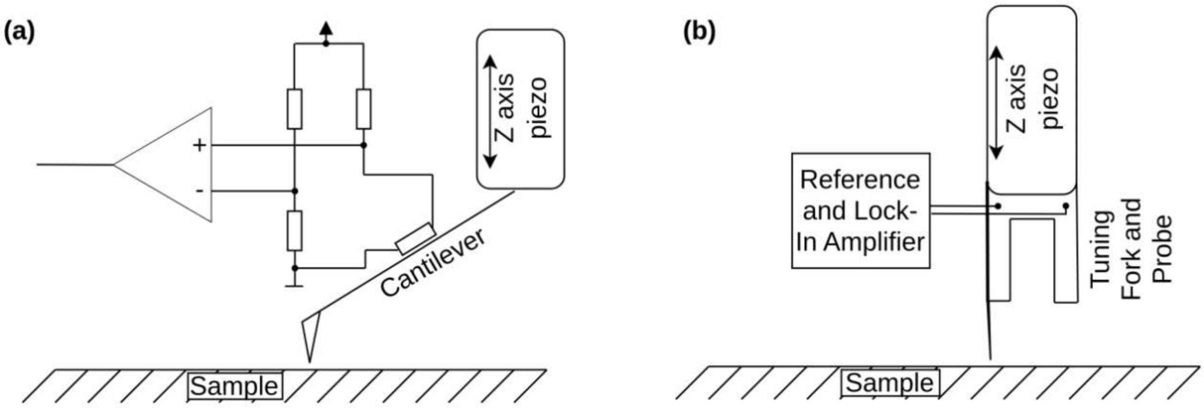

Figure 2.4: (a) shows a strain gauge sensor added to the cantilever in a bridge configuration (adapted from [24]); (b) shows a piezoelectric tuning fork with attached probe (adapted from [25]).

Piezoelectric

Using the piezoelectric effect which is present in quartz crystals and resulting in a mechanical force being indicated by a proportional electrical signal, tuning forks, like shown in Fig. 2.4 (b), have been used for reading cantilever positions. Implementations of these quartz tuning forks have shown to have noise levels of $35 fm/\sqrt{Hz}$ at a cantilever oscillation frequency of $33kHz$ [25].

Summary

With the achievable noise and measurement bandwidths in mind, the different methods for extracting the deflection of a cantilever, which in turn indicates the surface topology of the sample, are evalueated. Due to the simplicity of the setup and ease in beam alignment, OBD is the most commonly used technique in modern commercially available AFM setups [23]. For this reasons, this work focuses on the OBD cantilever deflection readout.

2.2 Topography Measurement Modes

While there are many measurement modes for AFM, which define under which conditions the cantilever tip to sample interaction happens, for measurements of surface topography three major modes have emerged [35]. In contact mode, the tip is dragging along the sample surface, while non-contact avoids this by oscillating it near the sample and just relying on Van-der-Waals forces. The combination of the former, the so-called tapping mode, has the oscillating cantilever tip is barely touching the sample during each oscillation cycle [36].

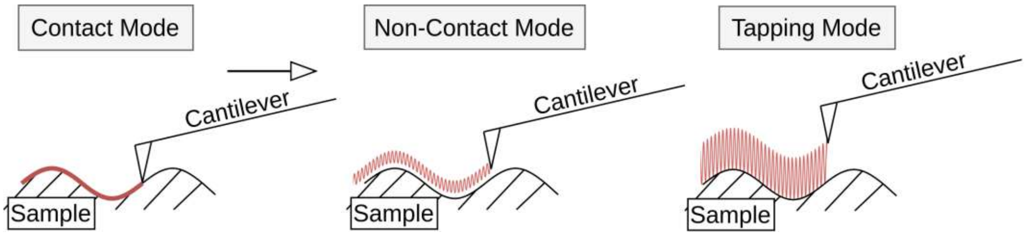

Figure 2.5: The three most widely used measurement modes for surface morphology measurements with AFM with the cantilever movement direction and its tip path indicated (adapted from [37]).

2.2.1 Contact

The AFM measurement mode shown in Fig. 2.5 works by having a cantilever with an attached tip in direct contact with the sample surface. It was the first measurement mode developed with the invention of the AFM. A feedback loop is implemented which keeps the deflection of the cantilever constant while scanning along the sample surface. This makes measurements simple to realise, but has the downside of gradual degradation of sample and tip due to frictional forces [1].

2.2.2 Non-Contact

By having the cantilever oscillate near the sample surface without touching it, the attractive Val-der-Waals forces pull the tip to the sample surface, therefore making the structure measurable, this mode is called Amplitude Modulated Dynamic AFM (AM-AFM) [8]. Due to these forces being smaller than those in contact mode, the oscillation amplitude needs to be kept small to be able to measure changes in phase, frequency or the amplitude of the cantilever, which is indicated in Fig. 2.5. However, this requires a low-noise instrumentation setup and highly controlled environment. While this method can be used non-destructively, it is in many cases not suited for samples with a liquid layer on top making it only applicable for certain applications [9].

2.2.3 Tapping

Due to both contact and non contact modes having different downsides, the third option as shown in Fig. 2.5 is called tapping mode. In this measurement mode, a feedback system ensures that the tip of the cantilever is only lightly tapping the sample surface for each cycle [10]. The resulting changes in amplitude or phase are used to determine surface characteristics [38].

While the cantilever itself behaves like a damped forced harmonic oscillator from Eq. 2.1 with F_0 and ω being the amplitude and angular frequency, finding an expression for the interacting forces from the tip to the surface F_{TS} proves to be difficult. The other equation parameters are in order m, z, k, ω_0 and Q representing mass, position in z axis, force constant, angular resonance frequency and quality factor, respectively [38].

$$m\ddot{z} + kz + \left(\frac{m\omega_0}{Q}\right)\dot{z} = F_{TS} + F_0 cos(\omega t) \tag{2.1}$$

The tip to sample interaction forces contained in F_{TS} in Eq. 2.1 have been thoroughly investigated and can generally be split into six groups, Van-der-Waals forces, capillary forces, electrostatic forces, magnetic forces, ionic and Pauli repulsion forces as well as frictional forces [33]. These forces are generally split into two regimes, attractive and repulsive, the attractive ones predominate if the tip to sample separation is high and vice versa below [39]. Combining all forces into the equation makes a solution difficult to find, therefore different approximations were brought up, either ignoring certain forces or combining them into simplified models, one such model is explained in 3.1.1 [33].

2.3 Tapping Mode Demodulation

Having the cantilever oscillate near its own resonance frequency and only lightly tapping the surface proves to be beneficial for many measurements, specifically ones with soft surfaces such as polymers or DNA-protein structures as it drastically reduces the damage to the sample surface [39]. This results in many setups being built around this, with the most commonly used readout method being OBD [40], Eq. 2.1 produces an output current proportional to this with an added offset current and noise sources [41].

The resulting signal mainly consists of a high frequency oscillation with a changing signal amplitude which is proportional to the tip to surface interactions, effectively amplitude modulating (AM) it [10]. This makes the usage of a lock-in amplifier intuitive, as it multiplies the resulting signal with the reference input of constant amplitude and applies a low-pass filter in order to be able to extract the AM signal as explained in Chapter 2.3.3 [42].

2.3.1 OBD Transimpedance Amplifier (TIA) Bandwidth and Noise

Converting the output current of each QPD section from an OBD-based AFM into a voltage via a TIA and calculating the necessary signals from there is the most common technique [41]. The TIA as shown in an example configuration in Fig. 2.6 (a), uses the gain resistor R to get an output voltage V_{out} linearly proportional to the input current I, resulting in the simple Eq. 2.2 [43].

$$V_{out} = RI \tag{2.2}$$

With the stability of the TIA being imperative, a compensation capacitor C_f has to be added for stability. The four parasitic capacitances that are detrimental to the stability are the photo diode capacitance C_{PD}, the summed up wire capacitance C_{wire} and the two op-amp capacitances for common mode C_M and differential C_{diff} inputs as shown in Fig. 2.6 (b) [40]. TIA stability is explained in depth in Chapter 3.1.5.

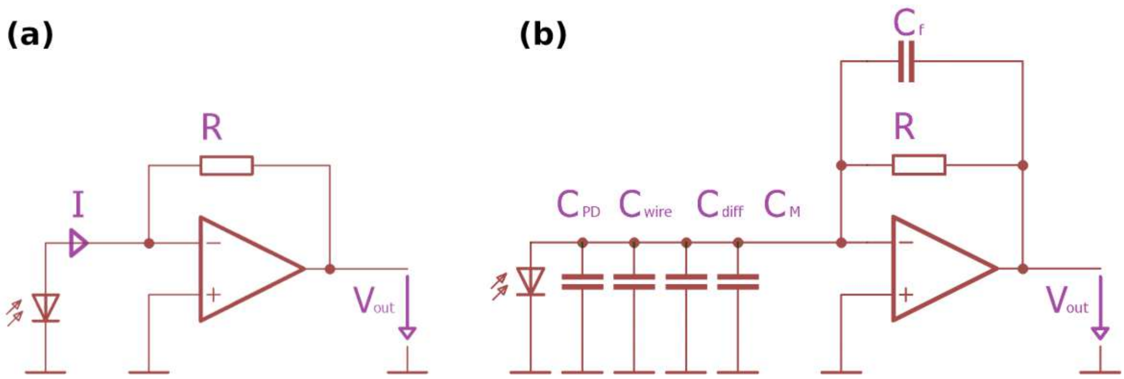

Figure 2.6: (a) TIA built around an operational amplifier with an attached photo diode and the current I resulting from the incoming irradiation converted via the gain resistor R to an output voltage V_{out}. (b) is the same circuit including parasitic capacitances C_{PD}, C_{diff}, C_{wire} and C_M as well as the feedback capacitance C_f. (adapted from [43]).

Utilising this method, low noise cantilever deflection sensors with high bandwidths have been researched and the typical deflection noise is largely dependent on bandwidth and the measurement environment, e.g. in air vs. liquid or piezo vs. photo-thermal excitation yielding a total sensor deflection noise density of $100 - 1000 fm/\sqrt{Hz}$ [44] [40].

By realising a high-bandwidth low-noise AFM, measurements of dynamic processes with high resolutions are made possible. This is important due to the lack of alternatives for certain measurements like biological samples in liquid [43]. Results from [43] produce a beam deflection sensitivity of $10 fm/\sqrt{Hz}$ at a bandwidth of $8.6 MHz$ in liquid utilising a laser-based photo-thermal excitation system for the cantilever for the study of ion organisation and hydration layers. The work of Rode *et al.* [44] implements a $1 MHz$ TIA to modify a commercial piezoelectrically driven AFM system to achieve $10 fm/\sqrt{Hz}$ in liquid. With a bandwidth of $64.5 MHz$ in air, Steininger *et al.* [45] managed to get $62 fm/\sqrt{Hz}$ in a laser path measurement setup developed for AFM usage by optimising laser power and choosing the right QPD and op-amp. By evaluating noise sources and splitting noise performance into each contributing part, Mahmoodi *et al.* [46] measured $107 fm/\sqrt{Hz}$ with an op-amp TIA bandwidth of $22.6 MHz$.

2.3.2 Translinear Amplifier (TLA)

With the implementation of circuits that use the linear correlation of transconductance and collector current of bipolar transistors, current mirrors were implemented for OBD readout [47]. The TLA circuit uses the fact that the oscillating cantilever is alternately reflecting more light on the top and bottom two photo diodes of the QPD as shown in Fig. 2.7 (a) and subtracting two output currents from each other as shown in Fig. 2.7 (c) before transimpedance amplifying the difference [41]. The TLA can be built around a MOSFET based current mirror as shown in Fig. 2.7 (b) and features very few parts which benefits its overall noise contribution [34].

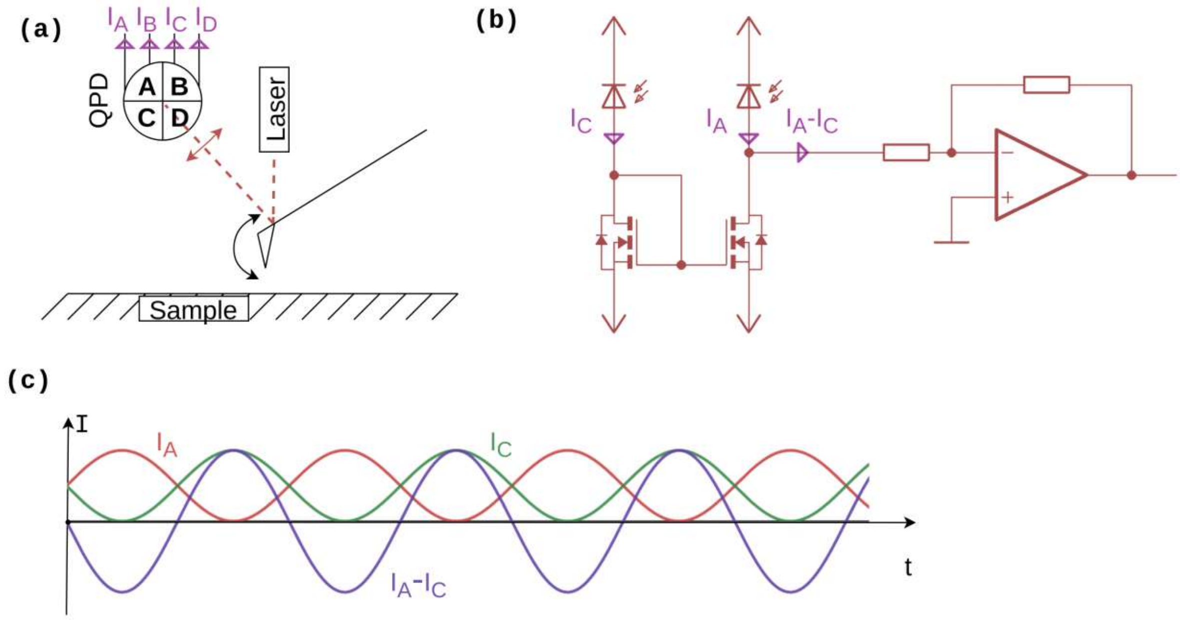

Figure 2.7: (a) The oscillating cantilever reflects more light to either the top two QPD cells A&B or the bottom two C&D; (b) TLA readout circuit with a MOSFET based current mirror and an ideal op-amp based TIA; (c) Is a plot of the two sinusoidal currents with an offset and their 180° phase shift shown in addition with their difference fed into the TIA. (adapted from [34]).

With a TLA implementation as presented above, images of muscovite mica in liquid with atomic resolution were achieved. Enning *et al.* managed to get to $4.5fm/\sqrt{Hz}$ spectral noise density at a bandwidth of $20MHz$ [34]. An experimental verification of an almost identical circuit by Alunda *et al.* managed to get a bandwidth of $10MHz$ which proves this method to be well suited for AFM applications [41].

2.3.3 Lock-In Amplifier

A lock-in amplifier is an open loop synchronous demodulator which mixes two input signals, to get a signal directly proportional to the measured oscillation amplitude [48]

[49]. Most commonly, off-the-shelf lock-in amplifiers are used to demodulate the output signal of a TIA or TLA, with the known cantilever excitation frequency as a second input, for easy extraction of the cantilever oscillation amplitude and phase [14].

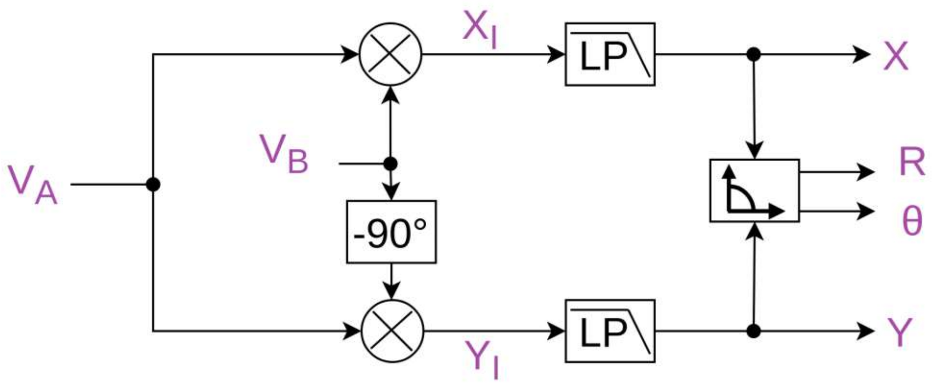

Figure 2.8: Lock-in amplifier functional diagram incl. phase and amplitude calculation (adapted from [50]).

The inner workings of a lock-in amplifier are shown in Fig. 2.8 and can be mathematically described. By applying the sinusoidal input signals V_A from Eq. 2.3 and V_B from Eq. 2.4 which represent the TIA or TLA output and cantilever excitation input, an output signal X_I as shown in Eq. 2.5 is produced. This is then low-pass filtered with a cut-off frequency lower than $2w_o$ in order for X to be directly proportional to the cantilever oscillation amplitude which changes the amplitude $A(t)$ and phase θ as shown in Eq. 2.6.

$$V_A = A(t)sin(\omega_0 t + \theta) \tag{2.3}$$

$$V_B = sin(\omega_0 t) \tag{2.4}$$

$$X_I = V_A V_B = \frac{1}{2}A(t)(cos(\theta) + sin(2\omega_0 t + \theta)) \tag{2.5}$$

$$X = \frac{1}{2}A(t)cos(\theta) \tag{2.6}$$

$$Y_I = V_A \widetilde{V_B} = \frac{1}{2}A(t)(cos(\theta - \frac{\pi}{2}) + sin(2\omega_0 t + \theta) - \frac{\pi}{2}) \tag{2.7}$$

$$Y = \frac{1}{2}A(t)sin(\theta) \tag{2.8}$$

By demodulating the same signal V_A with $\widetilde{V_B}$ which is phase shifted by $-\frac{\pi}{2}$, as indicated in Eq. 2.7, the resulting signal Y now includes a term $sin(\theta)$ instead of $cos(\theta)$. This enables extraction of both amplitude R and phase θ with equations Eq. 2.9 and Eq. 2.10 respectively [14].

$$R = \sqrt{X^2 + Y^2} \tag{2.9}$$

$$\theta = tan^{-1}(\frac{Y}{X}) \tag{2.10}$$

Lock-in amplifiers can also be implemented digitally which have the possibility to facilitate many data processing steps in the digital realm. This includes tuning of the ADC sampling frequency, predecimation filters for noise optimisation and multichannel direct digital synthesis for interleaved data to increase the overall signal-to-noise ratio [16]. This technique is demanding for the ADC sampling rate as well as its needed resolution and accuracy [50].

Although lock-in amplifiers are the most widely used demodulation system for AFM OBD readout circuits, the limited bandwidth combined with the need for external hardware is limiting their usability spectrum. Other methods have been suggested and implemented to circumvent this, but this is an actively researched field [14]. The possibility for a new technique which directly implements the demodulation into the TIA is proposed in this work.

CHAPTER 3

Theoretical Background

This chapter explains the theoretical background for the proposed analog demodulation with a Variable Gain TIA (VG-TIA). Also, the benefits of subtracting two or more QPD signals to be able to implement a TLA as subtractor TIA are described as well as the background and how those interact. This chapter should give an overview on each proposed system block as well as the details on how it is supposed to work and its relevant characteristics. Each block is backed by its necessary functional theory, which embeds it in the larger framework. Applicational use cases are explained for the system as a whole so that the theory can be easily put into practise.

3.1 Dynamic AFM

For many kinds of laboratories researching surface science, the AFM is a highly relevant tool, mainly due to the ability to measure with accuracies of up to $10^{-10}m$ [36]. Using a dynamic method, such as the tapping mode, offers major advantages over the static contact mode. While the latter needs to be in constant contact, therefore damaging the sample surface, tapping mode can lessen this, while simultaneously having multiple possible readout channels. This is due to the oscillation amplitude, phase and frequency being measurable, compared to deflection and torsion for contact mode. Additionally there is the benefit of being able to not only measure the resulting force on the cantilever, but also the force gradient while moving to and from the sample surface [39].

3.1.1 Tip to Sample Interaction

While the tip to sample interaction forces can be split into six groups, magnetic forces, capillary forces, electrostatic forces, ionic and Pauli repulsion forces, frictional forces and Van-der-Waals forces, not all of them are equal in their order of magnitude and finding a mathematical solution including all of them has been proven difficult to find [33]. Due to the complexity, a number of simplifications have been have been introduced and modelled to describe different applications. One of those is the Derjaguin, Muller, Toporov (DMT) model [51], which neglects the tip to sample contact energy dissipation and describes low adhesion materials with hard surfaces and small tip radii to get the short range repulsive forces. A different model incorporating the interaction forces between molecules, shown in Fig. 3.3, is the Lennard-Jones potential [52]. Forces are considered long range as soon as the tip to sample distance exceeds the intermolecular distance a_0.

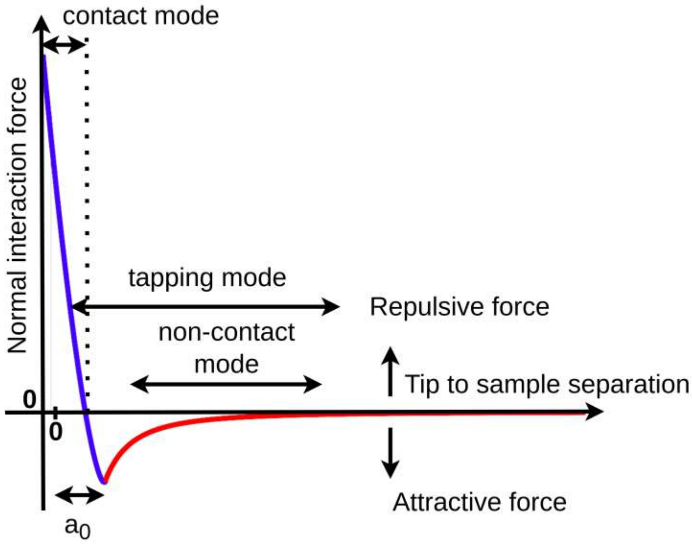

Figure 3.1: Total tip to sample interaction forces modelled using Lennard-Jones potential for molecular interaction forces (adapted from [9]).

Having the cantilever stick to the sample due to an overall attractive force can lead to an instability in the oscillation. This can be avoided by a large enough cantilever oscillation amplitude while supplying enough power to compensate for the losses in each oscillation cycle. Operating the cantilever in a stable dynamic mode is important for facilitating its advantages and choosing a fitting cantilever with the right quality factor Q and force constant k is crucial [8].

3.1.2 Cantilever

The actual interaction between the AFM and its sample is based on the forces between the cantilever tip and its surrounding structures. These forces explained in 3.1.1 are the defining factors for the design of a cantilever and its tip. Besides the rectangular design, triangular cantilevers with cutouts in the middle, as shown in Fig. 3.2 are commonly used as they offer different mechanical characteristics. The resonance frequency of the cantilever is largely influenced by its length L, width a and height b as well as its material. Silicon is commonly used which also benefits the OBD readout due to its reflective surface [53]. Some manufacturers add a layer of aluminium to the back side as coating to increase the reflectivity which accomplishes greater sensitivity in turn [54].

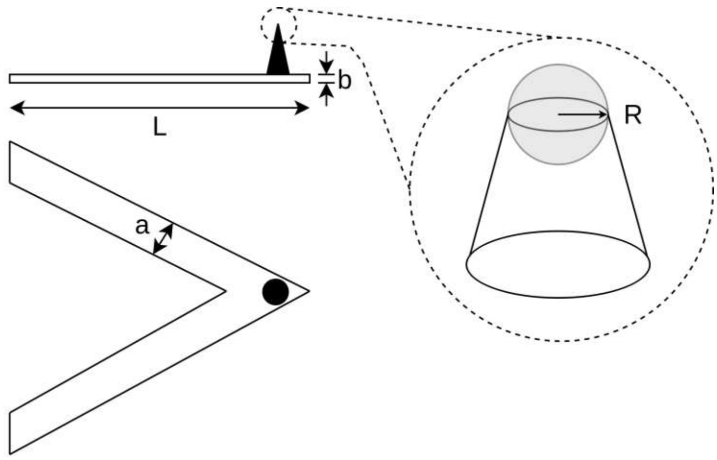

Figure 3.2: Triangular cantilever top and side view with its mechanical dimensions and tip radius (adapted from [53] [55]).

With the tip radius R being the defining factor for minimum observable topographical features, it is indispensable to adhere to good measurement practises which avoid its degradation. For sharp tips, it can be in the order of $4 - 10nm$ and degrades while being used in the tapping mode due to friction forces and plastic deformation [55].

3.1.3 Oscillation Amplitude and Phase

Using the tapping AFM measurement mode results in a practically sinusoidal output waveform with the same frequency as the exitation source, while having a phase shift between those two, and an amplitude depending on the mechanical parameters of the setup and the gain of the transimpedance amplifier. Fig. 3.3 shows a dynamic AFM with the relevant exitation input to the z-axis piezoelectric actuator and the transimpedance amplified QPD output signal [38].

By looking only at the amplitude change of the output signal, a significant part of the sample surface information can be lost. Forces acting on the tip that are not proportional to topographical features like adhesion, plastic surface deformation, electrostatic interactions and others result in measurement errors which can be reduced by a phase measurement [56].

Implementing a phase and amplitude measurement is usually done after a lock-in amplifier or similar implementation as indicated in Eq. 2.9. Lock-in amplifiers often

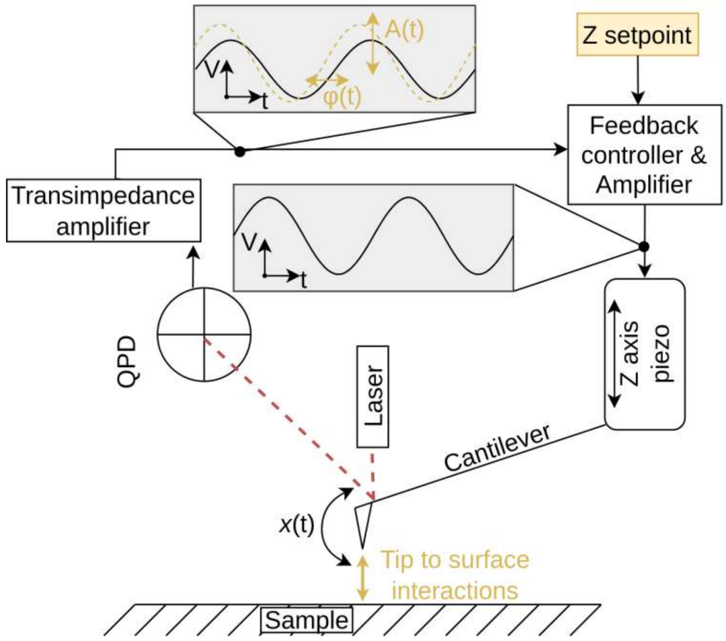

Figure 3.3: Dynamic AFM with exitation and output waveforms pictured. The amplitude and phase change of the cantilever oscillation due to different types of surface to sample interactions is shown in yellow [38].

times have this mathematical operation for extraction already included and are therefore the most widely used tool [11].

3.1.4 Four Quadrant Photo Detector (QPD)

To be able to choose the right PSD for an application, there are a certain parameters to choose from. The most commonly used detectors, shown in Fig. 3.4 (a), are QPDs consisting of four segmented silicon-based photo diodes separated by a small gap [45]. Each of those diodes can be split into its small signal equivalent circuit, as shown in Fig. 3.4 (b) and consists of an ideal current I_Q being generated by the pn-junction of the photodiode, the dark current I_D and parallel capacitance C_P as well as the shunt and series resistances R_P and R_S [57].

$$I_X = I_Q - I_{sat}(e^{\frac{qV_{bias}}{K_B T}} - 1) \tag{3.1}$$

The total output current I_X for each photo diode is defined in Eq. 3.1, resulting in the characteristic exponential output current curve. It can be obtained from the ideal current I_Q by using the saturation current I_{sat} and bias voltage V_{bias} additionally to the constant values for the electron charge q, Boltzmann constant K_B and absolute temperature T [57].

As the parallel capacitance is detrimental to the stability of the TIA, it needs to be

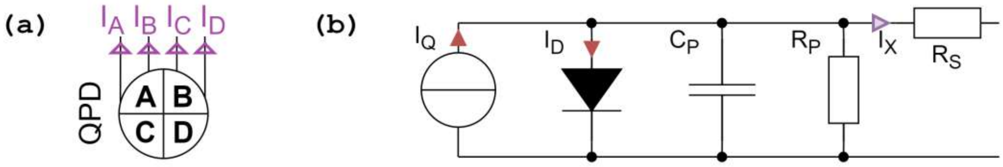

Figure 3.4: (a) QPD with each quadrant and output current to show in (b) the small signal equivalent circuit for a QPD and the corresponding currents (adapted from [57]).

kept as small as possible. Modern QPDs are similar in their capacitances and, with a bias voltage applied, result in values around $3 - 20pF$ depending on the size of each segment. While smaller segments result in lower capacitances, choosing a QPD of sufficient size is important for setting up the measurement and aligning the incoming laser light.

3.1.5 Transimpedance Amplifier (TIA)

The output of the QPD being a current proportional to the incoming irradiation, usually in the order of $10 - 100\mu A$, it needs to be amplified and converted into a voltage as shown in Fig. 3.5. The parasitic input capacitance C_S is detrimental to the stability of the TIA, as it adds a pole to the transfer function of the system [40].

$$A_N(f) = R \cdot \frac{1 + j2\pi f R(C_S + C_f)}{1 + j2\pi f R C_f} \tag{3.2}$$

Therefore the feedback capacitance C_f is added, to compensate for that and add a phase margin. The noise gain Eq. 3.2 shows that the additional capacitance added is making the noninverting closed loop voltage gain stable. Simplifying this to Eq. 3.3 defines the corner frequencies for the pole f_p and the zero f_z shown in Fig. 3.5. If the corner frequency of this added pole is set higher than the open loop gain of the op-amp, which defines the gain bandwidth product GBW, the TIA is not stable and will oscillate. The resulting overall bandwidth of the TIA is defined in Eq. 3.4 [44].

$$A_N(f) = R \cdot \frac{1 + j\frac{f}{f_z}}{1 + \frac{f}{f_p}} \tag{3.3}$$

$$B_{TIA} = \sqrt{\frac{GBW}{2\pi R C_S}} \tag{3.4}$$

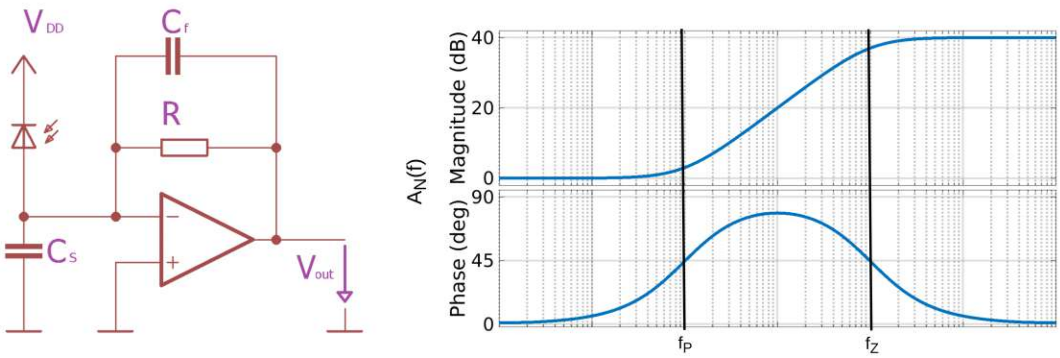

Figure 3.5: Non-inverting closed-loop gain for a TIA with parasitic capacitance C_S and the feedback capacitance C_f with the corresponding noise gain bode plot (adapted from [58]).

3.2 Sample Preparation

In order to be able to measure sample surfaces with high accuracies, samples have to be prepared and appropriate substrates have to be chosen. This proves to be especially important for biological samples such as protein crystals, Deoxyribonucleic Acid (DNA), biomolecules, cells and others [59].

3.2.1 Substrates

A substrate is chosen by analysing the sample properties and needed parameters. Its surface needs to be smooth enough in order not to influence the measurement and still be able to have the sample attached well enough for it not to move around due to the forces applied by the cantilever tip.

While tapping mode AFM applies less lateral force to the sample as contact mode AFM does, there have still emerged only a few different substrates which are widely used in conjunction [59]. For a lot of samples, mica has been used, as well as glass and silicon oxide [61]. DNA and nucleoprotein samples can use mica with ionic treatment or metal cations to increase the sample to substrate connection strength, as the negatively charged backbone of DNA does not effectively bind to the negatively charged mica surface otherwise [62]. Muscovite mica can be produced in layers of $1nm$ thickness and results in a negatively charged atomically flat surface [59]. An example of muscovite shown in Fig. 3.6 clearly shows the size proportions of the hexagonally shaped $AlO3^+$ and $SiO4^+$ rings including the basal oxygen atom bridges between them [60]. Hydrophobic substrates made out of highly orientated pyrolytic graphite (HOPG) can also be atomically flat and are commonly used for particles that come in dry powders [61].

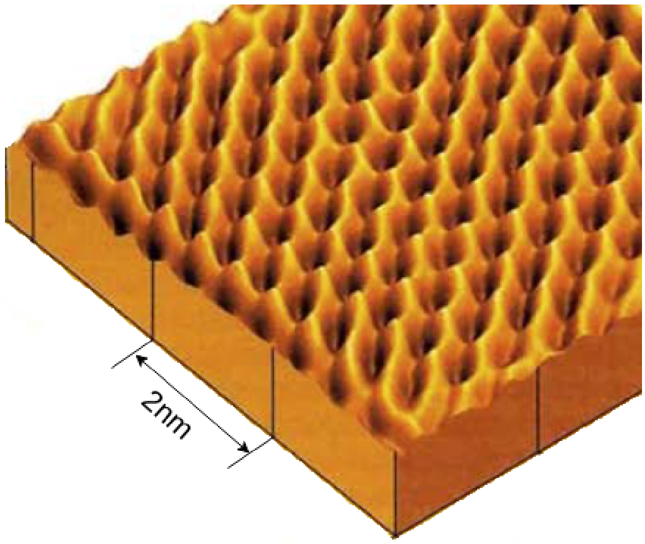

Figure 3.6: Muscovite surface AFM image showing the $AlO3^{+}$ and $SiO4^{+}$ hexagonal rings with bridges created by basal oxygen atoms [60].

3.2.2 Immobilisation

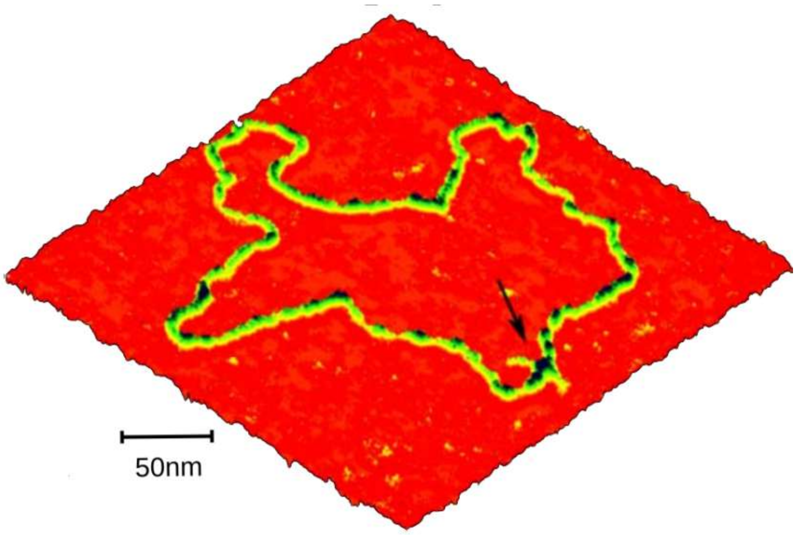

Figure 3.7: Circular shape of DNA immobilised on a mica substrate with a cruciform extrusion indicated with an arrow [62].

Immobilising the sample on the substrate can be done with different methods. Especially for biological samples, applying them mixed in a liquid solution which evaporates is often done. Measurements in liquid can be done by physically adsorbing the sample onto a substrate like mica and for larger molecules, covalent binding can be used with proteins like collagen being adhered using a cross-linker [59].

This process can deform the sample structure and for small feature sizes like DNA molecules, tests have been implemented in order for these deformations to be accounted for. Imaging DNA with its circular shape can be achieved with this and even the protruding cruciform structure marked with an arrow in Fig. 3.7 can be clearly measured. With drastically offset DNA double helix pitches, post immobilisation treatments like heated incubation have been shown to mitigate those effects [62].

3.3 Noise Sources

As the total noise of the setup is a limiting factor for the measurement sensitivity and therefore the topographical resolution limit, knowing the components and their noise sources is self-evident. They can be split into the following parts and should give an overview of their importance [40].

3.3.1 Mechanical Noise

Mechanical vibrations and oscillations are inherent to all environments AFM setups are situated in. They are usually filtered via multiple dampening and isolation elements. Firstly, vibration isolated tables, which use heavy elements resting on pneumatically actuated isolators, form the workbench for the setup to rest on. Additional isolation elements made out of soft materials are used in conjunction with additional pneumatic hoods for acoustic and vibration mitigation [43].

In the end, a compact and well designed mechanical head with the active mechanical measurement loop fully enclosed inside is important to avoid the noise permeating the outer layers and minimise their influence as much as possible [43].

3.3.2 Laser Source Noise

With a closed loop constant power semiconductor laser driver as proposed in 4.1.1, the highest influence on its noise level is its output power in relation to the maximum output power. Limiting the output power of a laser diode to a value below half of its maximum, yields a drastically reduced output noise [23].

The reason for this is the mode hopping of the laser at higher output power resulting in output intensity fluctuations as shown in Fig. 3.8 [23]. An alternative to that would be to modulate the laser current at frequencies above $200MHz$ to operate it in a multimode regime and suppress mode hopping wile also having a lower coherence which helps with noise generated by optical interference on the QPD surface [43].

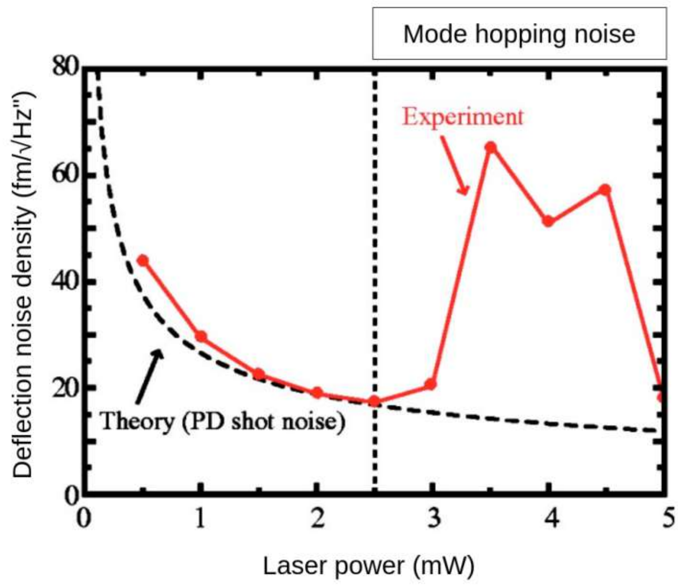

Figure 3.8: Deflection noise density depending on the laser output power. Above a threshold, the noise level increases significantly above the theoretical photo diode (PD) shot noise, which is caused by the mode hopping of the laser [23].

3.3.3 OBD Noise

The two biggest factors in the measurement noise of an OBD setup are the shot noise from the photo diodes in the QPD and the Johnson noise created in the TIA gain resistor. The former is created by the discrete nature of the incoming light particles and electric charges, the latter by the thermally agitated electrons inside the resistor at temperatures above 0K [23].

The shot voltage noise v_{shot} can be modelled with Eq. 3.5, incorporating a gain reduction factor ξ_{PD} which is frequency dependent and caused by the photo diode junction capacitance as well as the TIA gain resistor R, electron charge e, light to current conversion efficiency η, an attenuation factor for the laser power α as well as its output power P and finally the total bandwidth of the setup B [23].

$$v_{shot} = \xi_{PD} R \sqrt{2e\eta\alpha PB} \tag{3.5}$$

Voltage noise generated by the resistor is defined in Eq. 3.6 for each photo diode in the QPD. The input variables different to the ones brought up in Eq. 3.5 are K_B and T, being Boltzmann constant and absolute temperature [23].

$$v_j = \sqrt{4K_BTRB} \tag{3.6}$$

3.4 Voltage Controlled Resistor (VCR)

In order to be able to integrate the functionality of a lock-in amplifier into a TIA to be able to directly demodulate the cantilever oscillation amplitude and phase, the gain resistor of the TIA must be changeable via an externally applied voltage signal. A VCR is the missing element for this and different approaches for implementation are considered in this section.

While there are many different approaches for resistors that can be controlled via an external signal, only a few of them are viable for usage in a VG-TIA due to their integrated Complementary Metal–Oxide–Semiconductor (CMOS) composition or compulsory grounded implementation [63]. Some VCR implementations are based on integrated circuits, like a multiplier and only need little external circuitry [64], but the most common VCR is based on a junction field effect transistor (JFET) [65].

3.4.1 Integrated Circuit (IC) VCR

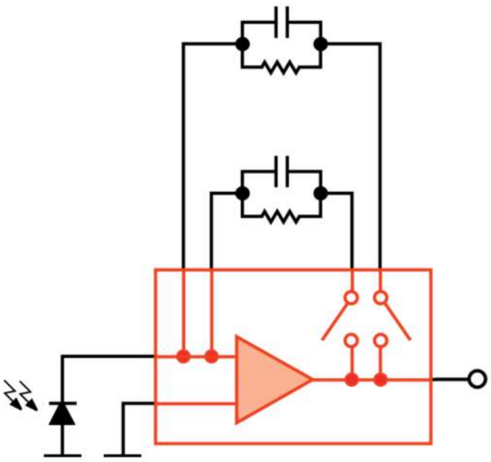

Figure 3.9: PG-TIA with integrated multiplexer for two different gain settings [66].

Programmable-Gain Transimpedance Amplifiers (PG-TIA) are integrated circuits (IC) which have one or more inputs for gain selection. They switch different resistors and feedback capacitors into and out of the amplification path via in internal multiplexer, as shown in Fig. 3.9 to achieve different overall transimpedance gains [66]. To be able to implement a VCR, there is the option to use an off-the-shelf PG-TIA and use the gain selector inputs with external circuitry to choose a gain synchronous with the demodulation input.

A similar implementation with an integrated circuit, which is able to dynamically set the gain, uses the analog input of a multiplier chip. This offers a high linearity, but has the downside of limited bandwidth [64].

3.4.2 Field Effect Transistor (FET) VCR

FET are used both in their linear as well as their saturation region to implement VCR. FET can use the dynamic resistance of FET, which is proportional to the gate to source voltage to implement this [67].

Junction FET (JFET)

The dynamic resistance r_{DS} of a JFET in ohmic region is shown in Eq. 3.7. This depends on the one hand on the physical dimension of the JFET, $2H$, W, σ being height, width and specific conductance of the channel and on the other hand on the pinch-off V_p and gate to drain V_{GD} voltages, of which the first is device dependent and the second applied during operation [67].

$$r_{DS} = \frac{1}{\sigma 2HW} \frac{1}{1 - \sqrt{\frac{V_{GD}}{V_P}}} \tag{3.7}$$

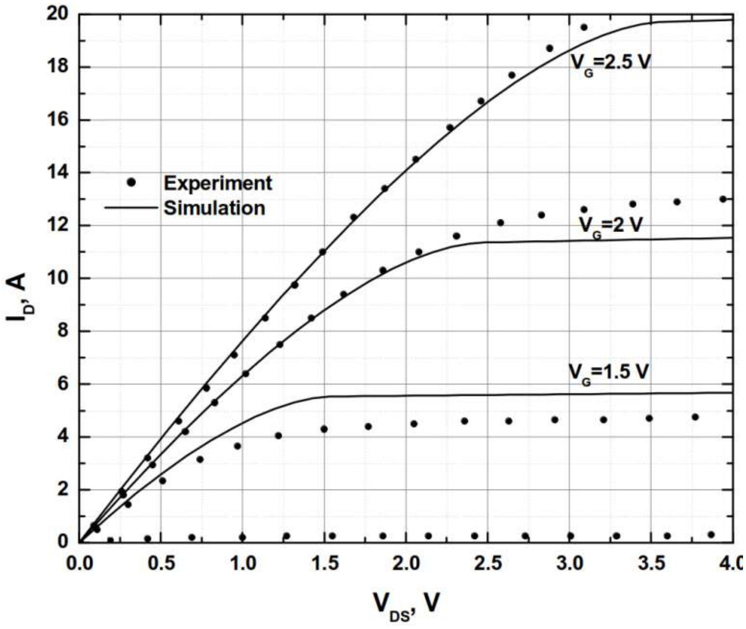

Figure 3.10: Drain current I_D in relation to the drain to source voltage V_{DS} of a n-channel JFET for different gate to source voltages V_G [68].

The resulting relation between the drain current I_D and drain to source voltage V_{DS} is shown in Fig. 3.10 in dependence of the applied gate to source voltage V_G. The linear region for different V_G can be clearly seen, which proves the wide adaption of the JFET in its ohmic region for VCR applications [67].

Metal–Oxide–Semiconductor FET (MOSFET)

Similarly to JFET, MOSFET can be used for VCR applications in their linear and saturation region [69]. With the most commonly available n-channel enhancement MOSFET, applying a positive voltage to the gate with respect to its source opens the conducting channel, which is vice versa to the closing channel of the most commonly used n-channel JFET with a negative V_G being applied.

$$r_{DS} = \frac{1}{\beta(V_G - V_t)} \tag{3.8}$$

With the MOSFET in its linear region, the output equation 3.8 for its dynamic resistance r_{DS}, is defined by physical parameters in the form of the gain factor β and the threshold voltage V_t [67].

3.4.3 Photoresistor VCR

A photoresistor is an optoelectronic element which has a transfer function between its resistance and a light intensity applied to its active area due to the internal photoelectric effect [70]. Alternatively there is the photo-FET, which is a MOSFET with a gate voltage applied by an incoming illumination. By implementing a device which shines a defined amount of light produced by a light emitting diode onto a photoresistor or photo-FET through the help of a light conductor, a galvanically isolated VCR can be created [71].

Fig. 3.11 shows an integrated VCR with both photoresistor (b) and photo-FET (c) outputs. Both of them are driven by the same light source Fig. 3.11 (a) [71].

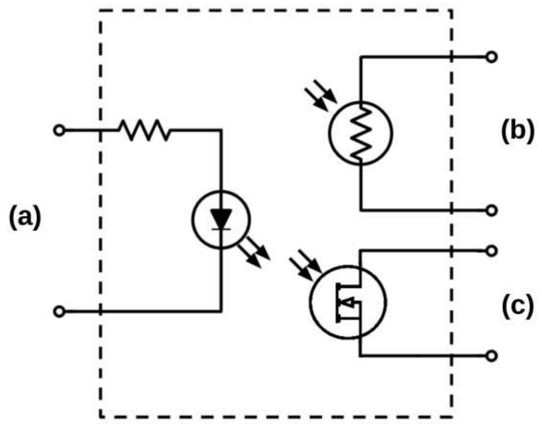

Figure 3.11: Integrated VCR with (a) a light source; (b) a photoresistor and (c) a photo-FET [71].

3.4.4 Summary

Many of the proposed VCR techniques largely focus on ohmic linearity and possible compensation methods for long term drifts and other inaccuracies [71], which is not the main focus on the implementation for this works VCR. As the theory presented in Chapter 2.3.3 for the lock-in amplifier suggests, a high difference in the maximum and minimum gain and a bandwidth higher than the cantilever oscillation frequency is far more important than the typical benchmarks. For this reason, the implementations presented in Chapter 5.4 focus largely on the latter.

CHAPTER 4

Proposed System

Equipped with the necessary theoretical background from Chapter 3 as well as the available research that has been done and is considered state of the art from Chapter 2, a new and improved system can be proposed. This is done through analyzation of the optical path including all components involved in the measurement and signal acqusition. From this point forward, the electrical subsystem is explored and the existing TIA as well as the proposed VG-TIA explained and mathematically verified.

4.1 Optical Path

The laser setup including the laser source, driver, light path, QPD and TIA are a large part of the total cantilever deflection noise density. Implementation of an OBD readout circuit for the cantilever deflection offers various advantages such as the simple and easy beam alignment and the straight forward setup design, which also results in it being the most commonly used cantilever deflection readout. This includes the laser source being a semiconductor laser, due to the additional complexity and cost of other laser sources as well as choosing the right cantilever for a desired measurement application. The state of the art TIA then converts and amplifies the QPD output currents into proportional voltages [23]. This work utilises said method while implementing custom circuitry to ensure high accuracy and fulfil the size constraints of the setup.

Alternative implementations with modulated laser currents have shown to result in reduced interferences and measurement artefacts [72]. While this method could be used, the additional circuitry and increased complexity of the system are a limiting factor. The major part of the interference is due to light being reflected off of the sample surface, which can be compensated for and therefore a different approach for noise minimisation can be chosen [23].

4.1.1 Driver

Designing a closed-loop low-noise laser driver is proposed to be the ideal solution for the implementation and testing phase of this work. Two options were taken into account, the first being a closed loop current control and the second a closed loop power control, both shown in Fig. 4.1. While the first option would result in a simpler circuit with a less expensive and readily available laser diode, small changes in temperature and other environmental factors can significantly influence the output power of semiconductor laser diodes, contributing to the noise [73].

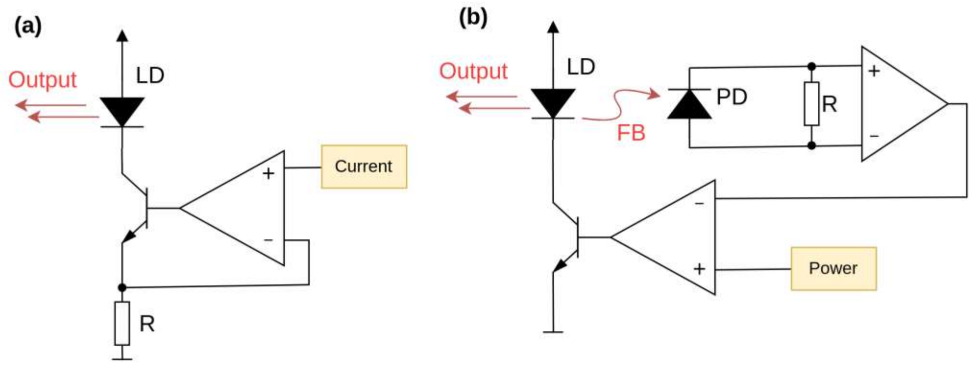

Figure 4.1: Closed loop laser driver circuitry with current and power control; (a) shows a current-controlled op-amp implementation with a laser diode LD and a gain resistor R; (b) is a power-controlled circuit with an integrated photo diode PD providing feedback FB from the LD amplified with the gain resistor R.

In order to measure not only the laser current, but also the real output power, a semiconductor laser diode with an integrated photo diode was evaluated and the closed-loop power control circuit shown in Fig. 4.1 was chosen. This enables a higher output power stability compared to the current controlled approach, while only using a slightly higher amount of components in total. In order to keep the circuit from oscillating, it's closed-loop response must be stable. For this, a low-pass filter can be added to the op-amp output depending on it's Gain Bandwidth Product (GBW).

4.1.2 Light Path

Design of the light path from the laser diode, reflecting off the cantilever and back onto the QPD plays an important part in the overall noise and resolution performance of the AFM setup. The chosen semiconductor laser source has an output divergence and is collimated by a collimation lense which is placed directly after the source and before the focusing lens. This enables a very well focused beam with minimal optical losses due to unwanted reflections off the sample surface and dispersion [74].

In order to be able to know the maximum distance between the cantilever and the QPD as well as the acceptable divergence to a certain cantilever deflection Eq. 4.1 defines their relation. The intensity difference ΔI is defined as the difference between the upper two intensities I_A and I_B and the lower two I_C and I_D as defined in Fig. 2.7. From this the cantilever deflection Δz can be deduced with the reflected beam divergence δ and the cantilever length l [33].

$$\frac{\Delta I}{I} = \frac{(I_A + I_B) - (I_C + I_D)}{I_A + I_B + I_C + I_D} = \frac{6\Delta z}{l\delta} \tag{4.1}$$

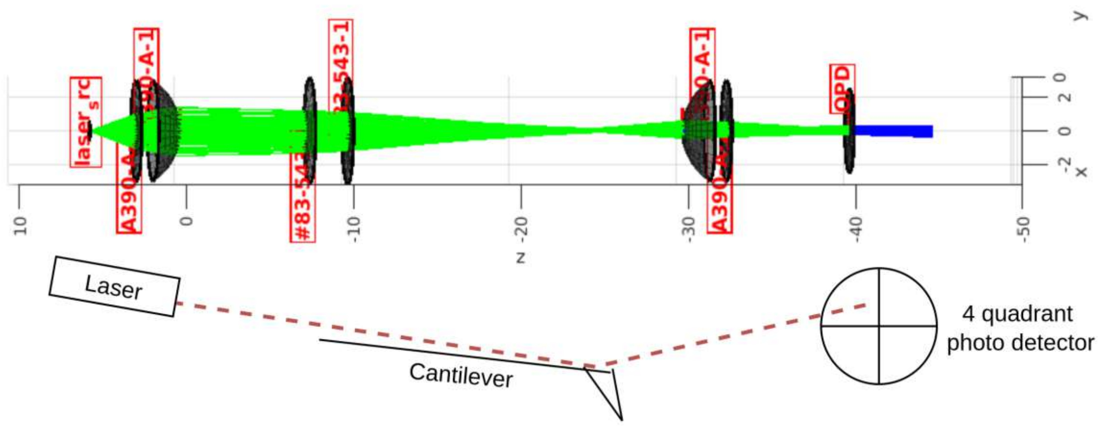

Figure 4.2: Laser path simulation with second focusing lens added to decrease the spot size of the QPD illumination in order to be able to increase the sensitivity. Beginning from the left, the first lens is collimating the highly divergent diode laser beam, while the second is focusing it onto the cantilever. On the bottom half a visual representation of the beam with the AFM components is shown for reference [75][45].

An alternative to the boundaries defined by Eq. 4.1 is implementing a second focusing lens after the laser has been reflected off the cantilever. This method shown in Fig. 4.2 has several advantages, as the spot size of the light illuminating the QPD is decreased. Therefore it is possible to make use of a smaller QPD, which in turn results in a smaller parasitic capacitance for the TIA and increases the mechanical deflection sensitivity of the setup [45].

In practice the laser beam shape produced by a diode laser is going to be oval in its shape due to the semiconductor waveguide being rectangular in shape. This so called astigmatism is dependent on the type of laser diode and can be corrected by two cylindrical lenses placed orthogonal to each other. On the other hand, the output intensity profile across the beam generally is Gaussian shaped and well suited for focussed applications like OBD [75].

4.2 Demodulation

Most dynamic AFM measurements use a lock-in amplifier explained in 2.3.3 as a basis for the amplitude and phase measurement. Although this is a simple solution, it comes with several major challenges especially for cantilevers with higher oscillation frequencies. This has spurred the search for alternative demodulation techniques to achieve lower noise, higher bandwidth or more easily implementable tapping mode AFM setups [76].

In order to be able to know what the necessary demodulation bandwidth should be, it is important to know the desired cantilever and its parameters. Eq. 4.2 describes how the maximum measurement bandwidth f_{BW}, which correlates with the maximum measurement speed and topographical sizes of a sample, is linked to the resonance frequency ω_0 and quality factor Q of the cantilever itself [77].

$$f_{BW} = \frac{\omega_0}{4\pi Q} \tag{4.2}$$

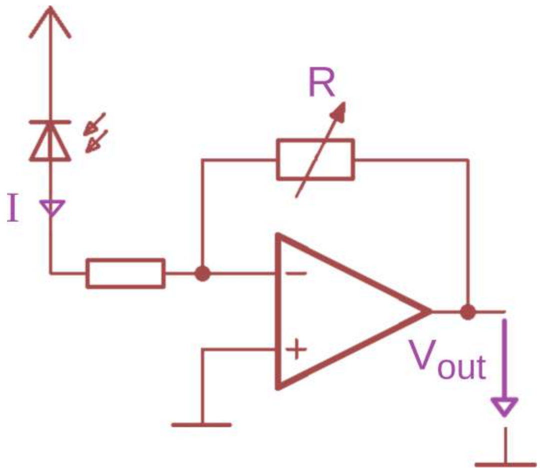

Figure 4.3: Adding a VCR to the TIA feedback path enables the TIA gain to be dynamically adjustable.

Identical to regular lock-in amplifiers, the desired demodulation technique as shown in Fig. 4.3 should therefore be able to have a bandwidth higher than the cantilever resonance frequency as well as a low-pass filter cut-off frequency higher than the measurement bandwidth. Additionally the resistance R should be able to be changed dynamically with the resonance frequency of the cantilever to enable demodulation of the current I produced by the photo diode.

4.2.1 VG-TIA

Fig. 4.4 (b) shows the novel approach for a VG-TIA, which makes the expensive and bulky lock-in amplifier (a) obsolete enabling a direct demodulation of the QPD output current in the TIA. This major simplification enables an implementation with fewer components which then in turn can reduce the challenges faced in tapping and other dynamic AFM measurement modes which use high resonance frequency cantilevers for high imaging bandwidths. The low-pass filter removes the additional 2ω component from the signal, identical to the internal low-pass of the lock-in amplifier explained in 2.3.3 [76].

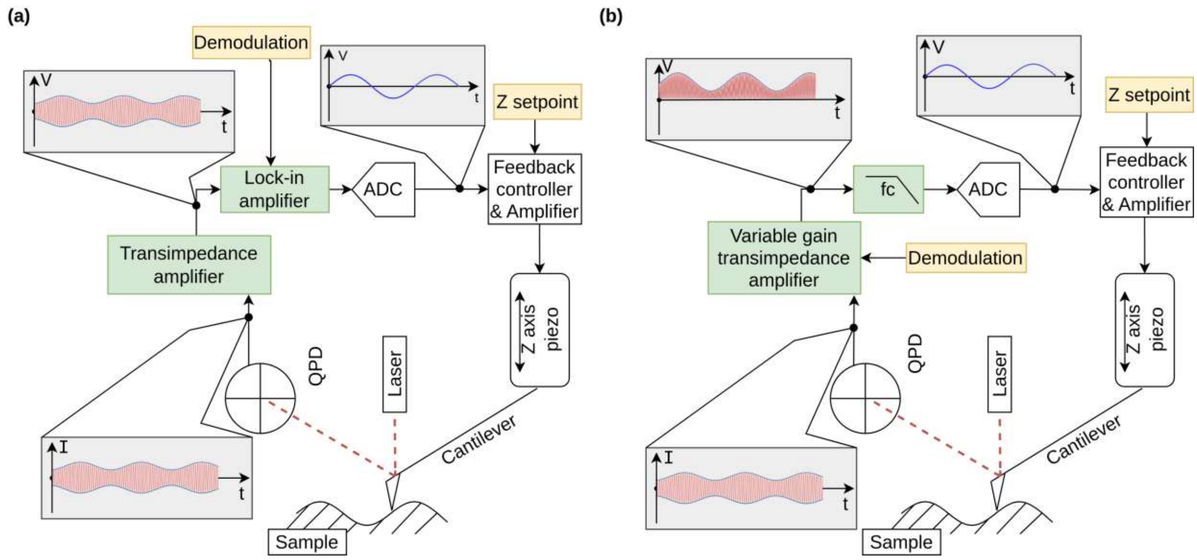

Figure 4.4: (a) State-of-the-art AFM setup with the QPD output current amplified and converted to a voltage by a TIA and demodulated and filtered by a lock-in amplifier; (b) Implementation of a novel laser signal demodulation with a VG-TIA and low-pass filter instead of the fixed gain TIA and lock-in amplifier.

The equation 2.6 for Fig. 4.4 (a) shows that the output of the lock-in amplifier shown is proportional to the cantilever oscillation and both amplitude and phase can be extracted via two demodulation phases as presented in Eq. 2.9 and Eq. 2.10 respectively. This behaviour can be implemented with a VG-TIA, by using the equations below. Eq. 4.3 shows one output current I from the QPD, which consists of an oscillating part with the oscillation frequency ω of the cantilever and a phase φ_Q as well as a dynamic part I_Q, which is proportional to the oscillation amplitude, incorporating the tip to surface interactions. By the devise of a time depended resistor R with an amplitude R_D and frequency ω identical to the cantilever oscillation, as defined in Eq. 4.4, the output equation of a regular TIA is modified to include this as shown in Eq. 4.5.

With the addition of this variable resistor and by modulating it with the same frequency as the cantilever, the output voltage U_{Xi} from Eq. 4.5 again has a term $I_Q R_D$ proportional to the cantilever oscillation amplitude and phase identical to the lock-in amplifier. The additional term with two times the oscillation frequency of the cantilever can be removed with the simple low-pass filter shown in Fig. 4.4 (b) to have get to Eq. 4.6.

Equations 4.7 and 4.8 use the same principal method, but apply a phase-shifted demodulation signal to the VG-TIA in order to get a phase-shifted output. Practically this can be realised by using the left and right halves of a QPD as shown in Fig. 2.7 (a) as separated inputs and demodulating them with two different VG-TIA and modulation inputs. This enables the full usage of all four QPD cells while simultaneously avoiding additional circuitry.

$$I = I_Q sin(\omega t + \varphi_Q)) \tag{4.3}$$

$$R = R_D sin(\omega t) \tag{4.4}$$

$$U_{Xi} = IR = \frac{1}{2} I_Q R_D (cos(\varphi_Q) + sin(2\omega t + \varphi_Q)) \tag{4.5}$$

$$U_X = \frac{1}{2} I_Q R_D cos((\varphi_Q) \tag{4.6}$$

$$U_{Yi} = I\widetilde{R} = \frac{1}{2} I_Q R_D (cos(\varphi_Q - \frac{\pi}{2}) + sin(2 + \varphi_Q) - \frac{\pi}{2}) \tag{4.7}$$

$$U_Y = \frac{1}{2} I_Q R_D sin(\varphi_Q) \tag{4.8}$$

To be able to extract the cantilever oscillation phase φ_Q and amplitude I_Q independently, Eq. 4.9 and Eq. 4.10 are used with the input signals U_X and U_Y which have a phase shift of $-\frac{\pi}{2}$ in relation to each other. With this final calculation, the output equations of a modulated VG-TIA are structurally identical to the lock-in demodulation theory presented in Chapter 2.3.3.

$$I_Q = \frac{\sqrt{U_X + U_Y}}{R_D} \tag{4.9}$$

$$\varphi_Q = tan^{-1}(\frac{U_Y}{U_X}) \tag{4.10}$$

The resulting wave forms shown in Fig. 4.4 (b) visualise the equations above and demonstrate the simplicity of this approach. Offsets and other non-ideal characteristics have not been discussed and included in the equations above and can either be compensated mechanically or in the circuitry. While the implementation of such a VG-TIA is not a trivial task, as shown in the following chapter, the end resulting setup can be used for many different AFM measurement modes and applications broadening the spectrum of available methods.

4.3 Proposed system Overview and Requirements

The novel AFM design proposed as shown in Fig. 4.5 combines and integrates the aforementioned methods and design principles. It is a tapping mode measurement AFM with an OBD cantilever deflection readout consisting of a constant power laser driver for closed-loop diode laser control, which is collimated and focused with the light path, terminating on a QPD. The attached VG-TIA demodulates and amplifies the signal before a low-pass filter outputting a voltage proportional to the desired cantilever oscillation amplitude acts as the final element.

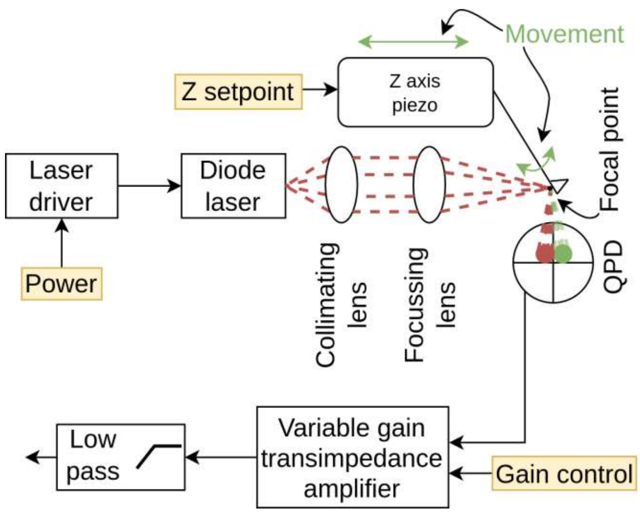

Figure 4.5: Proposed AFM system design. The Z axis piezoelectric actuator induces a forced oscillation into the cantilever at or near its own resonance frequency, which is then picked up as a lateral movement on the QPD. The resulting current can be demodulated via the VG-TIA and low-pass filter.

The advantages of the VG-TIA can be evaluated by the simpler setup, while the OBD readout ensures an easy configuration of the mechanical parts and sample. By being able to control laser power, cantilever position and movement as well as the VG-TIA gain separately, each component can be tested and verified independently. Implementation of this system and its chosen components is explained in detail in Chapter 5 and results are shown in Chapter 6 highlighting the real world use-cases on some example topographies.

CHAPTER 5

System Design and Integration

With the necessary theoretical knowledge, a practical system can be designed and integrated into an existing AFM setup. This application of the state of the art combined with the proposed approach for a demodulation directly in the TIA via the VG-TIA was done in several steps. Firstly two prototypes were built for testing and evaluation of different VG-TIA, subtractor TIA and laser driver as well as the necessary low-pass filter and power management circuitry. Each design was measured and compared to the other available implementations before choosing the best combination of them.

5.1 Concept

In the end the design has to be able to fit into the existing head of a *MultiMode V* AFM and interact with the available software and all features. For this, the newly created hardware should be able to connect to the *NanoScope 6* controller via the *Signal Access Module* supplied by the manufacturer *Bruker*.

The proposed implementations were realised on two custom Printed Circuit Boards (PCB) which were manually assembled and tested for functionality before use. Integration of the custom hardware into the existing software could achieved via a custom measurement mode where the gain from the VG-TIA was set to be at a constant level and deviations from that governed to be kept constant while measuring. The resulting images and control errors are included in the evaluation in Chapter 6.

5.2 Laser and Optical Path Implementation

The laser path and lens positions were constrained by the existing AFM head and were measured and simulated to check their positions and possible mounting points for additional lenses. The laser path shown in Fig. 5.1 shows the light beams being almost perfectly collimated before being focused on the cantilever itself. Due to mechanical constraints, the implementation of a second focusing lens was not implemented. A filter to avoid stray illumination of the QPD is placed in front of it to only pass light near the 640nm wavelength from to the red diode laser.

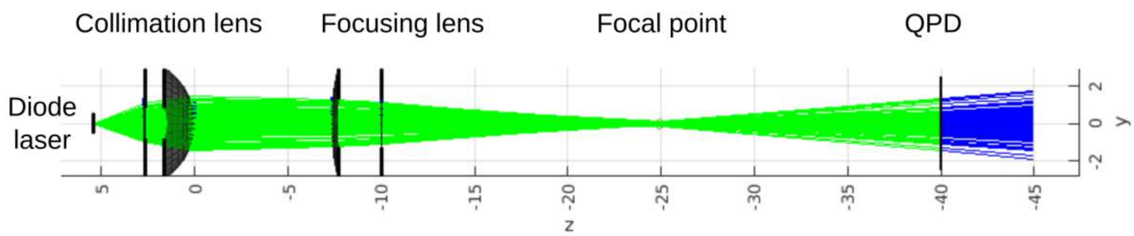

Figure 5.1: Laser path with diode laser output on the left being collimated and focused to have the focal point on the backside of the cantilever before being reflected onto the QPD.

5.2.1 Laser Driver

As the laser driver had to be used both in a constant output mode for measurements and a modulated output mode for setting up and aligning the laser path, both laser drivers shown in Fig. 4.1.1 were implemented. This offered the benefit combining the better long term output stability of the closed loop power control with the fast modulation speeds of the closed loop current control. This switchable controller is shown in Fig. 5.2 and was implemented on the prototype PCB shown in Fig. 5.6.

It is also important to control the power dissipation of the laser diode as output wavelength drift and semiconductor degradation heavily influence the measurement [75]. For this a aluminium fixture with heatsinking capabilities was created to facilitate measurements running for a longer time or with higher output power .

5.2.2 Laser Setup

Setting up the mechanical path of the laser signal required the setup to have different points for path adjustments. The three main ones marked in yellow in Fig. 5.3 are required to be able to do the following steps. Firstly the cantilever is brought into position so that the laser beam directly reflects off the end and is centred. Secondly the laser is focused directly on the back of the cantilever as well as possible to avoid light

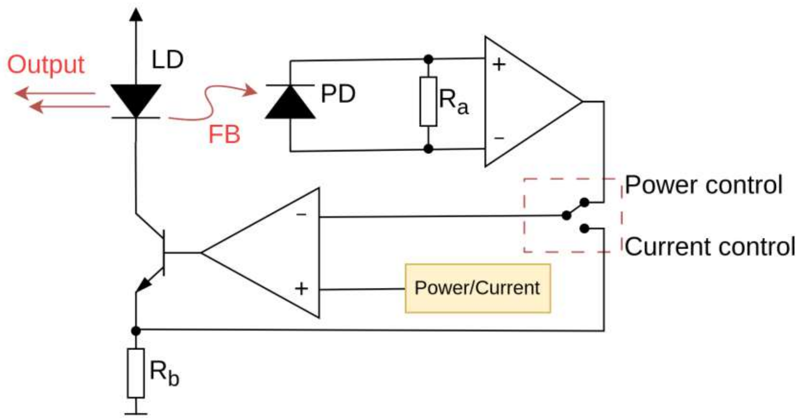

Figure 5.2: Combined closed loop laser driver with power or current control.

being being lost on either side of the cantilever and reflected off the sample surface. The third and last part is done by looking at the output currents of the QPD while changing its position relative to the incoming beam. This then enables an identical amount of light to shine on all four of its photodiodes removing static offsets in the transimpedance stage.

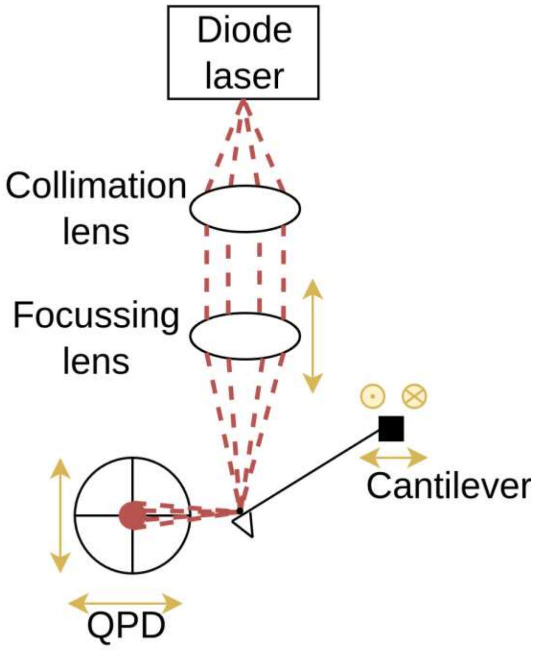

Figure 5.3: Laser path setup with the three main points for mechanical path adjustments.

If the laser path is set up correctly, the laser should be aligned as indicated in Fig. 5.4. In practice, the laser focus is constrained by the astigmatism of the output beam, limiting the size and shape of the focal point and allowing some light to pass the back of the cantilever. This unwanted behaviour can lead to changes in the sample and result in distorted measurements due to this light spillage [78].

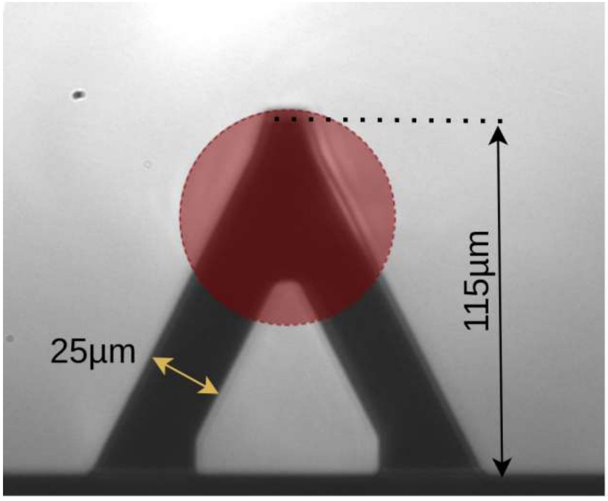

Figure 5.4: Microscope image of a triangular cantilever with the ideal laser position for a not perfectly focussed beam indicated in red and the length and width dimensioned.

5.3 QPD Circuitry

The QPD as shown in Fig. 1.1 normally consists of four photodiodes with a common anode or cathode. Each photodiode is a silicon semiconductor with an internal p-n junction which has an inherent capacitance and a spectral response for different wavelengths [79]. Choosing a QPD with a spectral response peak matching the laser diode wavelength can be done by careful consideration of different parts. The inherent capacitance on the other hand can not be changed and is proportional to the size of the active area of the photodiode itself. There therefore is a trade-off between the size of the QPD and the achieveable bandwidths for the TIA as explained in section 3.1.5.

A trick to lower the capacitance of the QPD is to decrease the size of the junction capacitance inside the photodiodes. This is done by pulling the cathode of the QPD to a potential higher than ground, effectively applying a reverse bias voltage to the photodiode and reducing the junction capacitance [79]. This is done with the use of a reference voltage as any fluctuations and noise is capacitively coupled through the QPD to the input of the TIA and detrimental to the output stability of the circuit.

5.4 TIA with Variable Gain

The novel approach of implementing the demodulation of a OBD cantilever deflection readout into the TIA is done by the means of a VG-TIA as explained in 4.2.1. The most important part was finding a circuit that can effectively change the gain of a TIA with enough speed and high enough difference between the highest and lowest gain setting while still being able to maintain a linear proportionality between the input current amplitude change and filtered output voltage over a wide enough bandwidth.

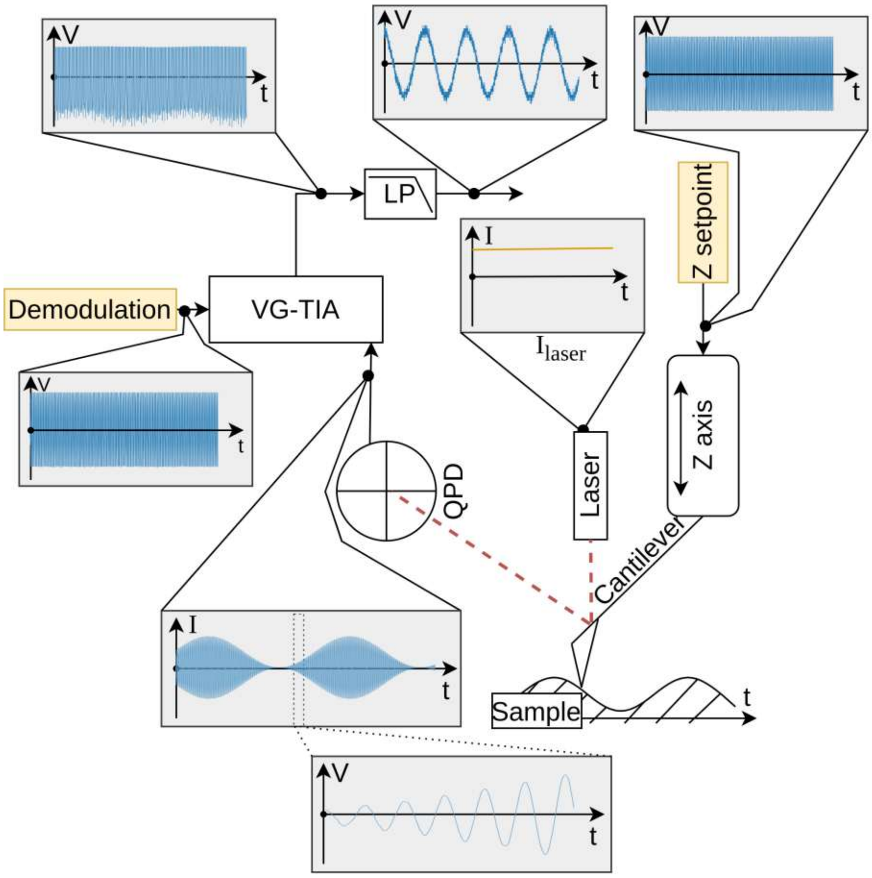

Figure 5.5: Schematical representation of the setup with a VG-TIA and measured signals for reference after each block of the system.

With equation 4.9 defining the how the theoretical behaviour of the VG-TIA should look like, Fig. 5.5 shows a practical example of those. The topographical information and movement along the surface can be effectively simulated via an amplitude modulation of the laser current while exciting the z-axis piezo and VG-TIA near the resonance frequency of the cantilever. The resulting output of the VG-TIA consisting of a signal component with double the frequency and a component directly proportional to the cantilever oscillation amplitude. The low-pass filtered output of this is then what the equation above prompts and therefore the system is working as intended.

5.4.1 VG-TIA Implementations

A first prototype as shown in Fig. 5.6 was devised to facilitate five different VG-TIA options as well as the aforementioned circuitry around. The power management circuitry generates the needed bipolar power rails for the op-amps with linear regulators to add as little noise as possible. The supporting components around the QPD output a reference voltage for biasing it and a connector to be able to ground it for testing. The laser driver is implemented as detailed in 5.2.1 with an additional header for a capacitively coupled input for biased AC operation. All five VG-TIA implementations are explained below and their test and measurement results are summarised in Chapter 6.

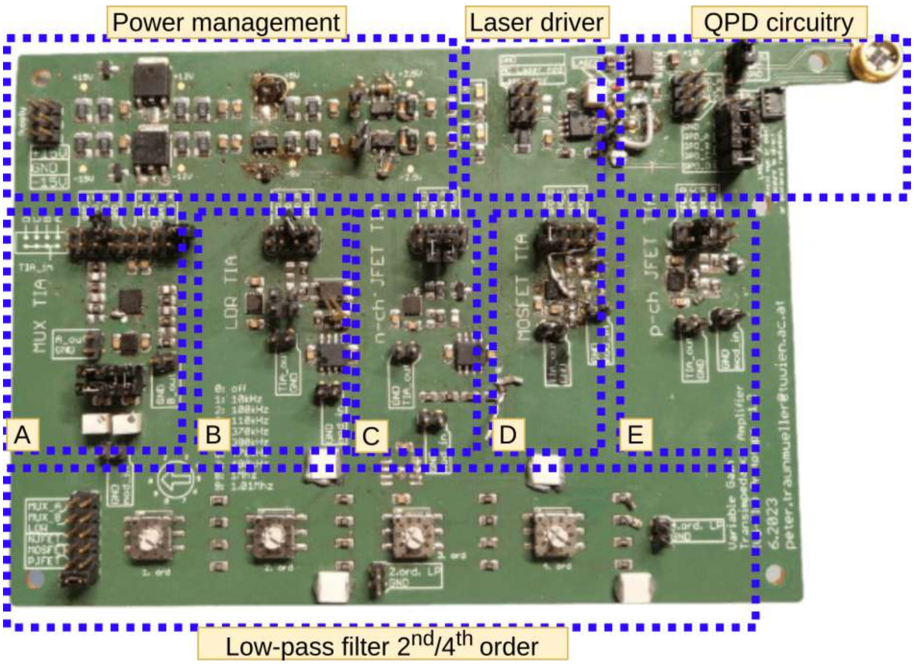

Figure 5.6: Prototype PCB implementing the five different VG-TIA as well as the laser driver, QPD reference and power management.

Resistor Multiplexing (MUX) VG-TIA

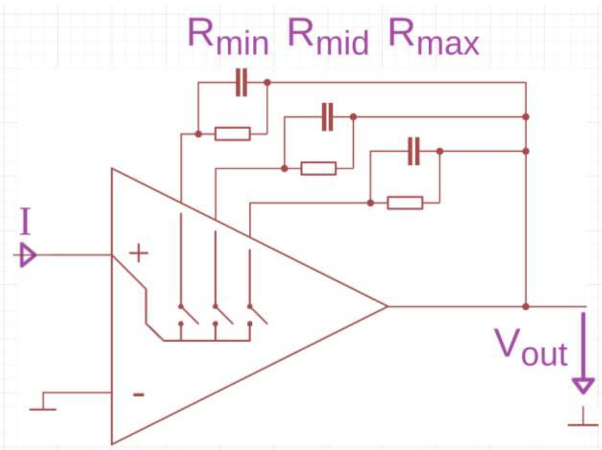

Figure 5.7: VG-TIA implemented with an integrated multiplexing circuit as programmable gain transimpedance amplifier.

Using the $OPA3S2859$ as dedicated programmable gain transimpedance amplifier, this implementation would be the most integrated for any of the VG-TIA options presented [80]. Its functional principle is shown in Fig. 5.7 and implementation in

Fig. 5.6 (A) where three gain resistors R_{min}, R_{mid} and R_{max} with one feedback capacitor each can be dynamically switched into the amplification path via two external inputs to act as the gain resistor R_g. The resulting amplification range is split into three discrete values defined by the resistors and shown in Eq. 5.1.

$$V_{out} = -I \cdot R_g \tag{5.1}$$

N-channel JFET Based VG-TIA

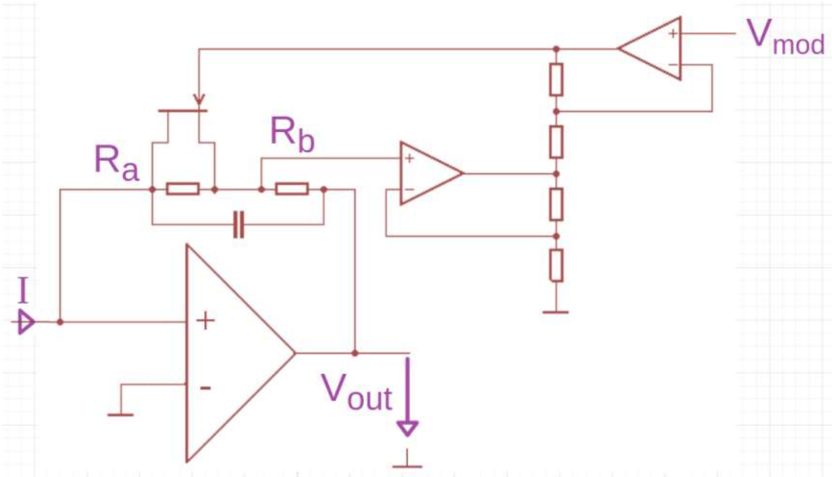

Figure 5.8: n-channel JFET with supporting subtractor op-amp circuit forming a VG-TIA.

Fig. 5.8 shows a VG-TIA with two gain resistors, one of which can be dynamically adjusted by a parallel n-channel JFET with its physical counterpart being Fig. 5.6 (C). To be able to apply a gate-to-source voltage externally via V_{mod} which is referenced to ground, a subtraction amplifier is built into the circuit. The JFET can be used both in its ohmic as well as the saturation region to be able to define its resulting resistance R_{JFET} both as an analog range and two digital steps. The output equation 5.2 shows how the the two gain resistors R_a and R_b and the JFET resistance R_{JFET} influence the total current to voltage amplification gain.

$$V_{out} = -I \cdot (\frac{R_a * R_{JFET}}{R_a + R_{JFET}} + R_b) \tag{5.2}$$

Lights Dependant Resistor (LDR) Based VG-TIA

By using a galvanically isolated LDR pictured in Fig. 5.6 (B), the VG-TIA gain can be changed as shown in Fig. 5.9. The LDR resistance can only be switched digitally, but has the advantage of not coupling additional noise from the modulation voltage

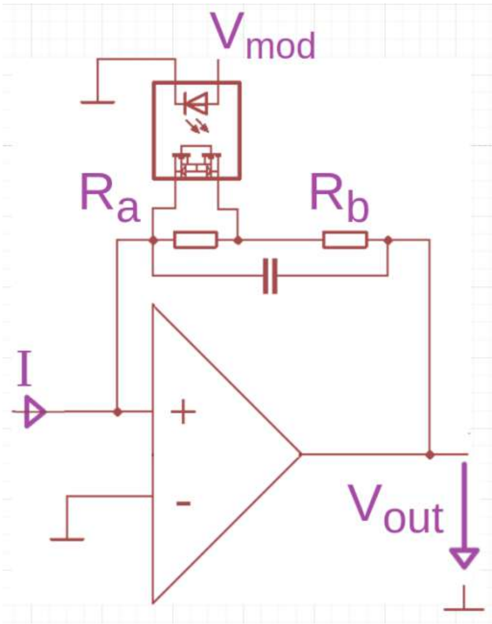

Figure 5.9: Modulation of one of the two gain resistors with a galvanically isolated LDR to implement a VG-TIA.

V_{mod} into the output. This implementation uses two resistors R_a and R_b for the high an low gain settings as shown in Eq. 5.3 to get an output voltage V_{out} proportional to the input current I.

$$V_{out} = -I \cdot (\frac{R_a * R_{LDR}}{R_a + R_{LDR}} + R_b) \tag{5.3}$$

MOSFET Based VG-TIA

By shunting parts of the incoming current I to ground, the MOSFET based VG-TIA can linearly change the amplification of the transimpedance amplifier. The feedback capacitance is connected over the complete gain resistor network to ensure output stability during switching and avoid possibly damaging current spikes through the MOSFET. This implmementation schematically shown in Fig. 5.10 is easily distinguishable from the others by its characteristic T-shaped feedback path.

$$V_{out} = -I \cdot (\frac{R_a R_b}{R_c + R_{MOSFET}} + R_a + R_b) \tag{5.4}$$

The output equation 5.4 includes all three gain resistors R_a, R_b and R_c, and while the former two define the maximum gain, the latter is responsible for the minimum due to the small resistance of the MOSFET R_{MOSFET} it its fully turned on state. Fig. 5.6 (D) depicts this in its physical implementation.

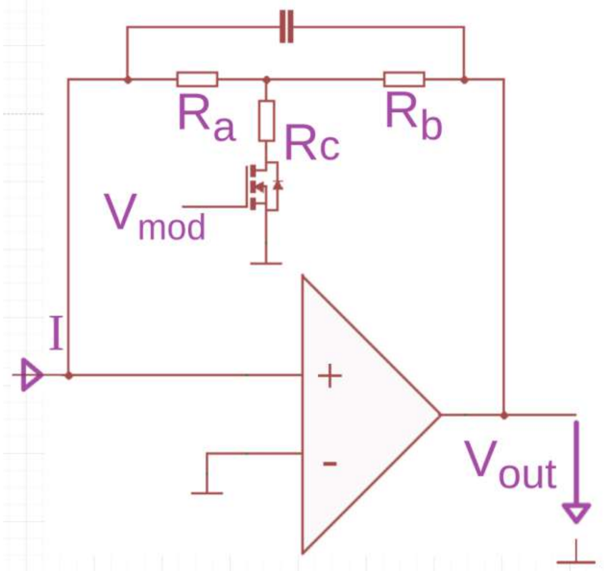

Figure 5.10: MOSFET based VG-TIA with the characteristic T-shaped feedback network shunting parts of the input current to ground.

P-channel JFET Based VG-TIA

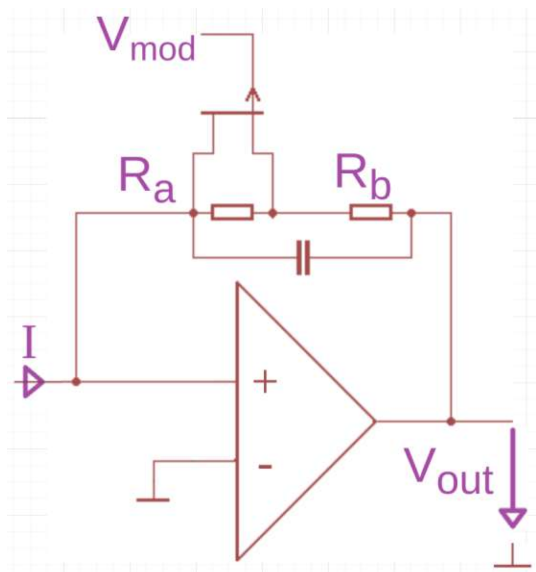

Figure 5.11:

Replacing the n-channel JFET from the implementation shown in Fig. 5.8 by its p-channel counterpart results in the simpler and overall easier circuit shown in Fig. 5.11 and real world implementation Fig. 5.6 (E). This is warranted by the fact that an op-amp based TIA keeps its non-inverting input close to $0V$ which enables the gate-to-source voltage V_{mod} not needing the subtractor circuit. This does not come without a downside though, as p-channel JFETs have lower availability and higher voltage noise for otherwise similar specifications [81] [82]. The mathematical correlation between the input current I and output voltage V_{out} is defined identically with Eq. 5.2 featuring R_a and R_b as gain resistors.

5.5 $2^{nd}/4^{nd}$ Order Low-Pass

The needed low-pass filter to remove the higher frequency components from the VG-TIA output was realized in two stacked unity gain Sallen-Key topologies as shown in Fig. 5.12. Each stage had two selection inputs to be able to switch four different resistors or resistor combinations for cut-off frequencies between $10kHz$ and $1MHz$ with a total of nine steps.

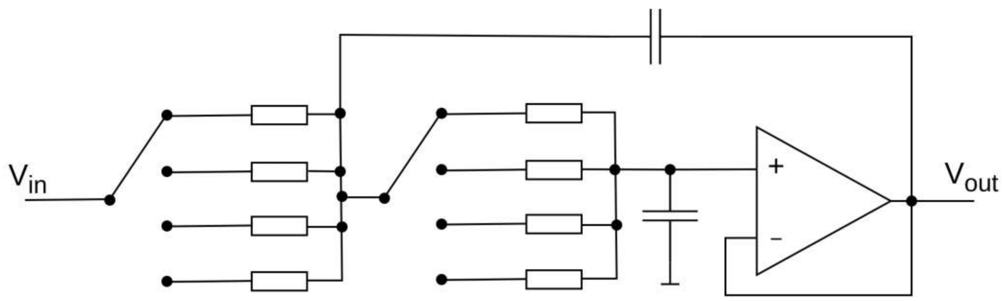

Figure 5.12: Low-pass filter in a Sallen-Key topology with switchable resistors to vary its cutoff frequency.

The input voltage V_{in} of the low-pass filter could be selected to be the output of each VG-TIA as well as an external signal for testing and verification of its frequency response.

5.6 Subtracting TIA

With the implementation of a TLA in the form of a subtracting TIA as explained in 2.3.2, the sensitivity for cantilever oscillation amplitude changes can be increased. This is due to the fact that a dynamic AFM measurement mode such as the tapping mode results in an illumination pattern which is vertically oscillating around the centre of the QPD. The subtraction of the resulting top and bottom signal from each photodiode effectively increases the available signal amplitude while decreasing the signal to noise ratio [34]. Two circuits that integrate this behaviour into the proposed VG-TIA have been implemented as shown in Fig. 5.13 including a laser driver with power/current modulation capabilities, QPD reference circuit, power management and the necessary low-pass filter.

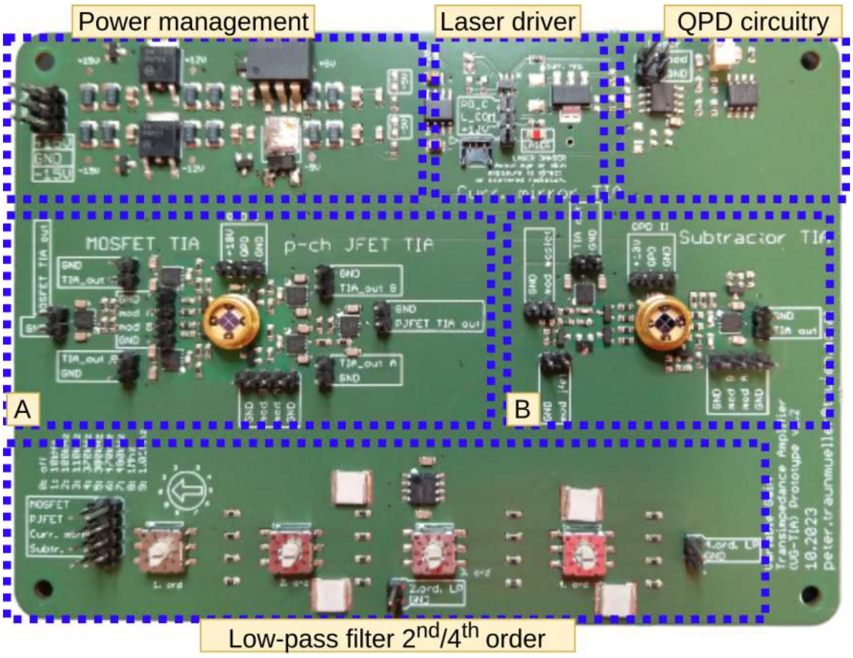

Figure 5.13: Prototype for the two subtracting TIA implementations; (A) shows a dedicated op-amp based subtractor VG-TIA; (B) is a current mirror with an attached VG-TIA.

5.6.1 Dedicated Op-Amp

Combining two VG-TIAs into a circuit with a subtractor is shown in Fig. 5.14. This dedicated op-amp based option enables the subtraction of the output voltages of each VG-TIA has an additional signal amplification integrated in the second stage in parallel with the subtraction. The physical implementation for this as pictured in Fig. 5.13 (A) focuses on short traces for low capacitive coupling between the QPD and each VT-TIA input.

The output voltage V_{out} as defined in Eq. 5.5 is dependent on both VG-TIA output voltages V_a and V_b amplified with by gain factor α defined by the resistor network around the right op-amp shown in Fig. 5.14. Each VG-TIA voltage is dependent on the photodiode currents I_A or I_C as well as the variable resistances R_a or R_b.

$$V_{out} = \alpha(V_b - V_a) = \alpha(-I_C \cdot R_b + I_A \cdot R_a) \tag{5.5}$$

5.6.2 Current Mirror

By subtracting the currents before amplification, the circuit shown in Fig. 5.15 implements a TLA similar to a solution proposed in ref. [34]. This solution has the downside of missing the additional amplification factor as compared to the implementation shown

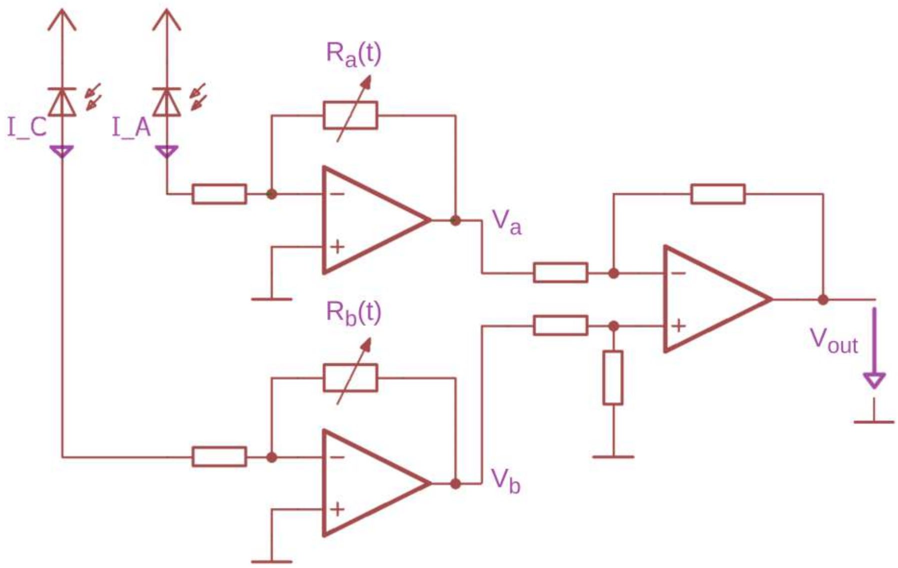

Figure 5.14: Subtracting TIA implemented with two VG-TIAs and a dedicated op-amp based subtractor circuit with additional voltage amplification.

in Chapter 5.6.1, but some outstanding advantages. Due to the limited output voltage of the op-amp defined by its supply voltage rails which also directly influence its output noise, amplifying only the current difference can be done with a much higher gain factor. Fig. 5.13 (B) puts this idea into practise while also offering the same short low capacitance traces for the QPD output as (A).

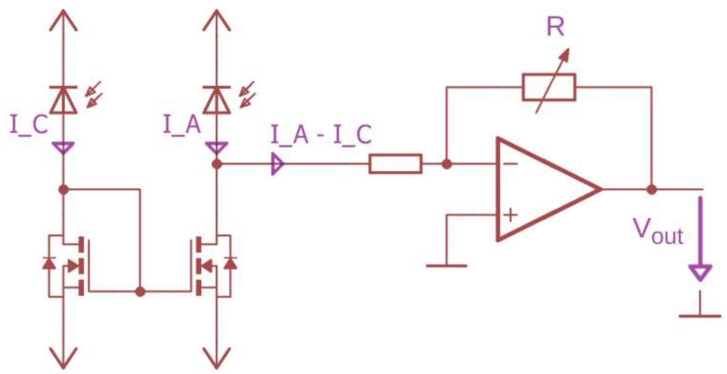

Figure 5.15: Subtractor TIA with current mirror based on the TLA design.

$$V_{out} = -(I_A - I_C) \cdot R \tag{5.6}$$

This TLA uses two MOSFETs in a current mirror configuration which subtracts the two currents I_A and I_C from each other before transimpedance amplification by R via Eq. 5.6 to get V_{out}. The current mirror works by connecting both gates of the MOSFETs to one of its drains, effectively coupling the drain currents to each other via its gate-source voltage depencency.

CHAPTER 6

Evaluation & Results

The implemented VG-TIA options, laser driver and subtracting TIA are tested and their capabilities for real world application are evaluated. This is done on a *Bruker MultiMode V* AFM as pictured in Fig. 6.1 with a *NanoScope 6* controller and *Signal Access Module* to connect the custom setup to the existing system. An *Agilent 33500B Series* waveform generator is used in the setup to be able to control the VG-TIA gain, the z-axis piezo and therefore cantilever position and the laser driver modulation input.

Both of the presented subtractor TIAs are tested and their results compared to each other. They both feature implementations for MOSFET and p-channel JFET based variable gain stages and are tested accordingly. For comparability, the results shown are only depicting one configuration.

The implemented laser driver is used in the current controlled setting for bandwidth measurements and a power controlled laser is used for the surface topography measurements with samples.

6.1 System Characterisation

Fig. 6.2 shows the relevant connections from and to the *MultiMode V* AFM. The AFM is set to contact mode and uses the filtered output from the VG-TIA as an input to evaluate the distance from tip to sample and control the applied force in each tapping mode cycle to stay constant. Both the VG-TIA and the piezoelectric actuator for the z-axis are externally supplied by a sinusoidal waveform with the same frequency and a

Figure 6.1: Picture of a *Bruker MultiMode V* AFM setup including attached microscope for visual cantilever adjustion.

phase set to maximise the output sensitivity.

The additional connection from the waveform generator to the laser driver is only used for testing and verification during the setup and specification. This is done in order for a full bandwidth specification of the VG-TIA to be achievable without the need of a cantilever with different resonance frequency for each data point and is schematically shown in Fig. 6.3. It is not used during a regular measurement operation and the laser power is set to a constant value chosen in the aforementioned process.

Initially all five presented VG-TIA implementations are measured, of which two show the most promising results and are taken into closer consideration. The evaluated VG-TIA behaved as described below.

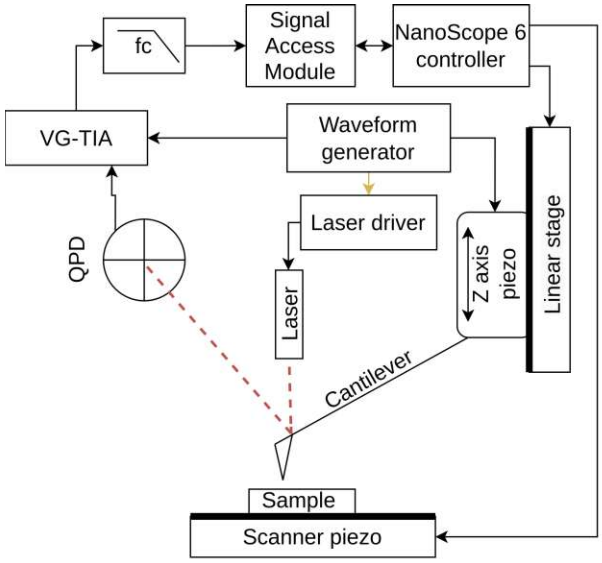

Figure 6.2: Connections between the unmodified *NanoScope 6* AFM controller and the newly implemented VG-TIA and associated parts. The connection between the waveform generator and laser driver is for testing and not used during normal scanning operation.

MUX VG-TIA

The resistor multiplexing implementation using the $OPA3S2859$ is not able to switch resistors with high gain differences dynamically. The intended use case of this IC is static gain switching to maximise the utilisation of ADC input ranges, therefore the transimpedance bandwidth specified in the datasheet is without internal switches being operated. For this application fast and periodical switching between selected gains via the internal switches is necessary. Switch transition times specified in the dynamic switching characteristics of up to $230ns$ are not reproducible in a cyclical switching operation of the $OPA3S2859$. This is presumptively caused by the internal switching logic limiting switching between gains to a sequential order, therefore making the IC unsuitable to be used as VG-TIA.

N-channel JFET VG-TIA

While the n-channel JFET theoretically would have yielded a lower noise level and easier sourcing, the additional circuitry is prone to oscillations due to the complicated gate to source voltage subtraction. This subtraction inside the feedback path of the VG-TIA as shown in Fig. 5.8 only allows stable operation with the addition of large feedback capacitors which considerably limit the switching speed. Only static gain settings are achievable with the circuit presented.

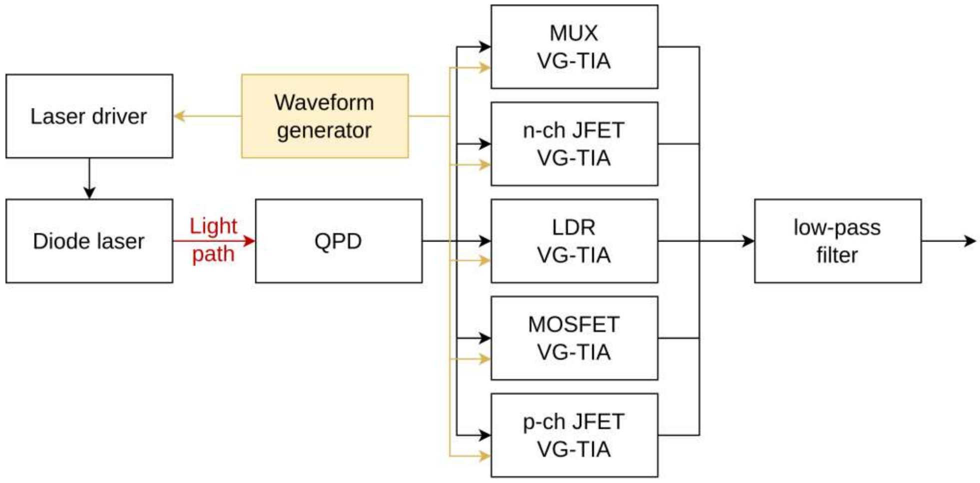

Figure 6.3: Bandwidth evaluation setup for VG-TIA and laser driver measurements.

LDR VG-TIA

An LDR implemenation features the galvanically isolated $TLX9175J$ with an LED and photo-MOSFET optically coupled inside a package. This results in an independently grounded demodulation input which avoids noise picked up by externally connected cables to be coupled into the VG-TIA. Due to the large gate capacitance and slow charge discharge speed on the detector side, this implementation is bandwidth limited to approx. $2.5kHz$. An additional external connection to this gate to be able to discharge it more quickly would be necessary for higher switching speeds.

MOSFET VG-TIA

The T-shaped feedback path configuration inside the VG-TIA enables parts of the incoming current being shunted to ground. With this configuration, the feedback capacitance is across the complete feedback path and stable operation is possible up to the expected frequency of approx $430kHz$.

P-channel JFET VG-TIA

Due to the TIA configuration, the source voltage of the p-channel JFET already is kept near ground. This enables a direct modulation input without additional circuity and operation of the JFET in both its resistive as well as saturation region. With the gate to source capacitance acting in parallel to the input capacitance, bandwidth of the VG-TIA has to be limited by the feedback capacitance as defined by Eq. 3.2.

6.1.1 Controlling the Transimpedance Gain

In order for the VG-TIA to work, the TIA gain needs to be chooseable by an external signal. This can either be a digital input or an analog voltage and should result ideally in resistances between 0Ω and $\infty\Omega$. Practically, at least one order of magnitude should be achievable for the demodulation to work. The values shown in Fig. 6.4 show that for both the p-channel JFET as well as the MOSFET based implementation, this is possible. The latter has a more gradual increase and can be sinusoidally modulated within the linear region of operation. This proves the theoretical idea proposed in 4.2.1 to be practically implementable.

$$\Delta A = \frac{A_{max}}{A_{min}} \tag{6.1}$$

Minimum gain for the p-channel JFET based VG-TIA is 0.023 for a modulation voltage of $0V$ and maximum 3.84 for $10V$. The MOSFET variant gains can be set from 0.014 to 1.9. This means that ΔA, the ratio between the lowest and highest gain defined in Eq. 6.1 is 166.96Ω for the former and 135.71Ω for the latter.

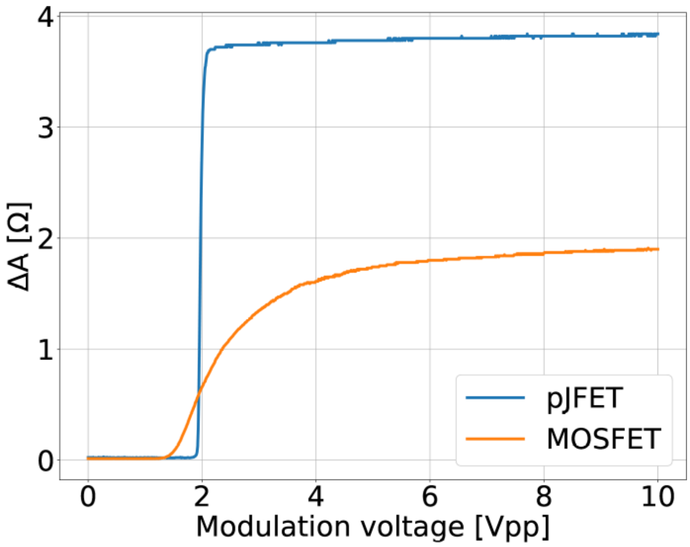

Figure 6.4: VG-TIA gain plotted as a function of the permittable input voltage range.

6.1.2 Fixed Gain Bandwidth

By keeping the VG-TIA set to a constant gain as shown in Fig. 6.5 (a) and frequency modulating the laser current, the bandwidth of the current to voltage amplification is measured. Both magnitude and phase are measured from $10kHz$ up to $4MHz$ with the reference signal for the phase being the measured laser current.

The resulting bode plot in Fig. 6.6 has a clear cutoff frequency around $300kHz$ for

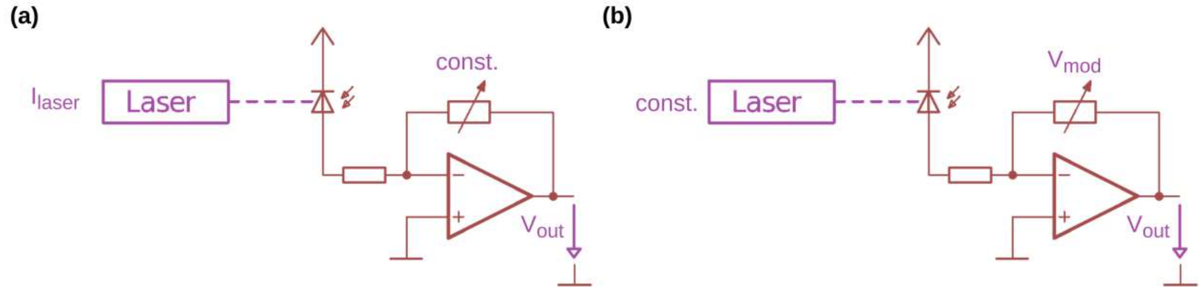

Figure 6.5: Setup for measuring the VG-TIA bandwidths; (a) shows the fixed gain bandwidth; (b) evaluates the variable gain bandwidth.

both VG-TIA with a rising magnitude up to this for the MOSFET and declining for the p-channel JFET VG-TIA. The phase is as expected up to this point, whereas it is not reliably measurable and has spikes due to the small signal amplitude and resulting phase measurement uncertainty.

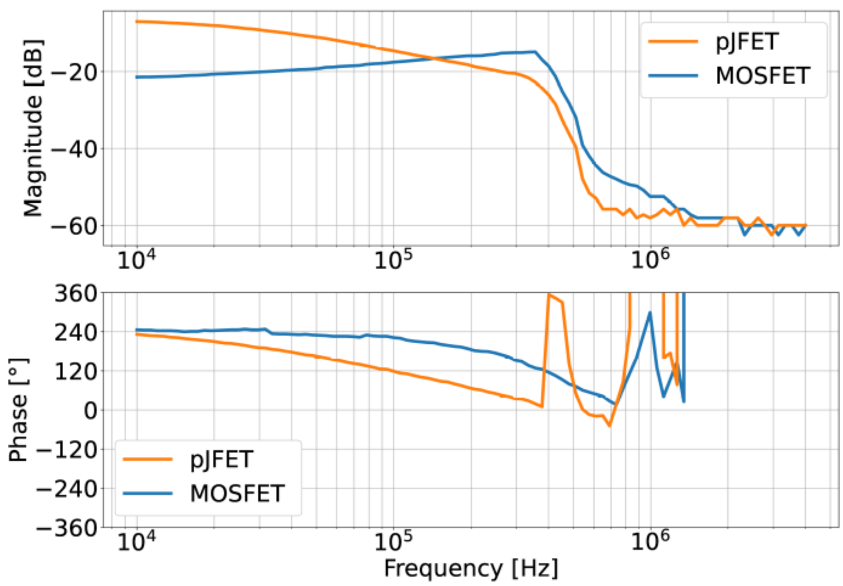

Figure 6.6: With the variable resistor set to constant gain, the bandwidth of the VG-TIA is plotted in relation to a frequency-modulated laser current.

6.1.3 Variable Gain Bandwidth

Only modulating the VG-TIA gain while keeping the laser current constant is shown in Fig. 6.7. This Bode plot is acquired by keeping the laser current constant while sinusoidally modulating the variable gain of the VG-TIA as shown in Fig. 6.5 (b). Both implementations show a similar phase and magnitude curve shape, with the JFET showing a lower frequency cutoff while maintaining a higher overall amplification. This can be explained by the additional input capacitance in parallel with C_S shown in Fig. 3.5 introduced by the gate-source capacitance of the p-channel JFET.

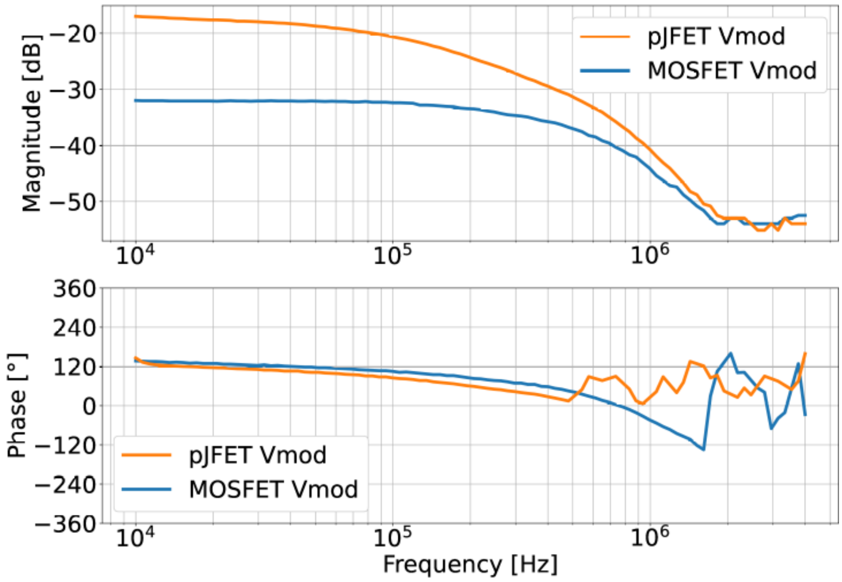

Figure 6.7: Bode plot for the variable gain bandwidth measured with a constant laser output.

6.1.4 Subtractor VG-TIA Output Linearity

With the VG-TIA results in mind, the full setup is to be tested and evaluated if the linear proportionality factor between the cantilever amplitude, which indicates tip to sample interaction forces, and the filtered output voltage predicted by Eq. 4.9 is true. For this, the subtractor VG-TIA is fed with a current generated by the QPD from an amplitude modulated laser. As this has to be done within the setup, the cantilever is exited at its resonance frequency without tip to surface interaction while the VG-TIA is modulated with the same frequency. This measurement was done with the low-pass filter set to a cutoff frequency of $10kHz$ and the amplitude of the demodulation input of the MOSFET-based VG-TIA set to $8V_{pp}$.

This is considered a critical step to prove the feasibility of the proposed tapping mode laser signal demodulation. While the results shown in Fig. 6.8 are simple to grasp, they prove this theory to be correct. The low-pass filtered output voltage V_{out} is linearly proportional over a wide range of laser amplitudes, which in turn is proportional to the cantilever deflection and therefore indicate the interaction forces from cantilever tip to sample surface.

By using a linear regression model to fit a first order polynomial into the transfer function, the maximum deviation from a fully linear proportionality can be calculated. The maximum measured deviation from this model is 4.63% of the full scale output for the current-mirror-based subtractor VG-TIA and 3.24% for the dedicated op-amp based subtractor VG-TIA. However, for the AFM to operate in tapping mode this curve does not need to be linear, as it is operated in a single operation point during feedback. What is interesting is the sensitivity (i.e. slope) of the curve, which puts the current-mirror-based subtractor VG-TIA ahead.

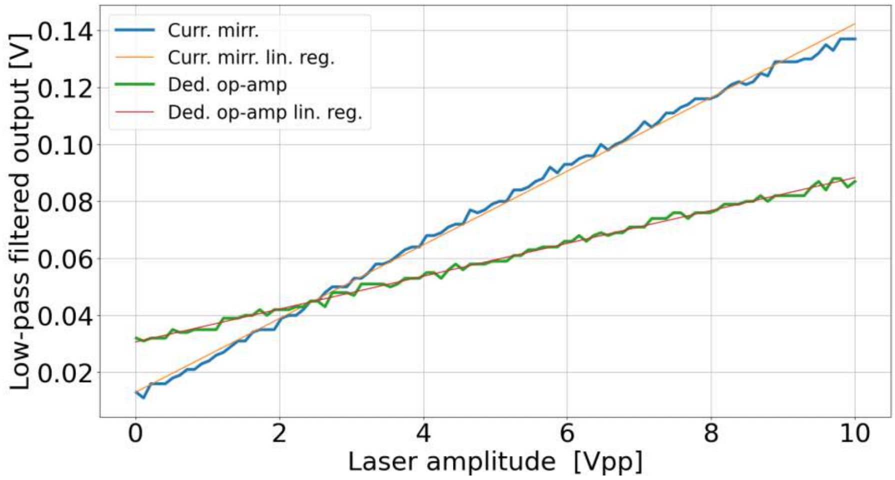

Figure 6.8: Evaluation of the proportionality between the laser amplitude, which is proportional to the cantilever oscillation amplitude, and the filtered output voltage for both MOSFET based subtractor VG-TIA.

6.1.5 Summary

Evaluating the theory put up in Chapter 3 and explained in chapters 4 and 5, the MOSFET-based subtractor VG-TIA proves this to be true and can be used for real world AFM measurement applications. Both the variable gain bandwidth as well as the fixed gain bandwidth are high enough to be used with high frequency cantilevers up to $300kHz$, the high gain differential of over 130Ω enables useful demodulation without a significant loss in measurement sensitivity and the highly linear overall laser amplitude to output proportionality with $< 5\%$ maximum linearity error.

6.2 System Evaluation

With a fully characterized implementation, actual topographies of test-samples are measured and shown in this section. For this, the triangular $scanasyst - air$ cantilever made by $Bruker$ is used in the setup, which has a nominal resonance frequency of $70kHz$ and a Q factor between 100 and 500 and an overall length of $115\mu m$ [54]. The cantilever is made out of silicon nitride and has a reflective aluminium coating of the back side.

The available samples are first prepared by carefully cleaning the surface with compressed air and preventing any other contamination from attaching to it before inserting them into the AFM head and aligning them under the microscope. After this the laser is focused and brought into position to reflect off the back of the cantilever as shown in Fig. 6.9. The light reflected onto the QPD is then measured and the QPD is moved so that the output current from each photo diode is identical.

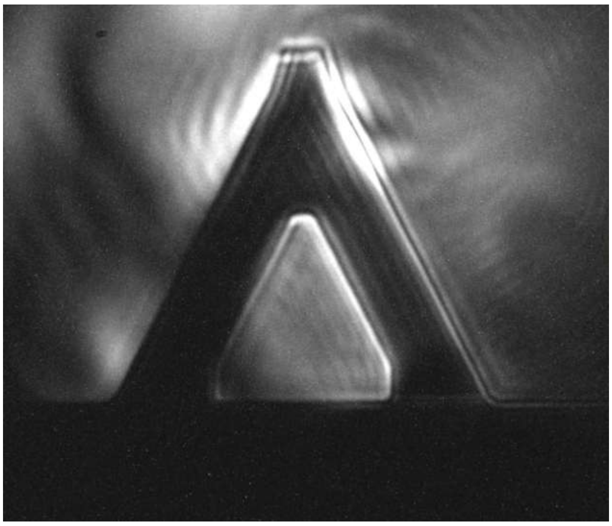

Figure 6.9: Camera view of the laser beam focused on the back of a cantilever.

6.2.1 Surface Topography Reference Measurement

To be able to evaluate the minimal feature sizes and reference resolution, a calibration grating is measured. This $VGRP-15M$ artifact made by $Bruker$ is platinum coated silicon, has a pitch of $10\mu m$ and each pit is $180nm$ deep. The measured surface topography is shown in Fig. 6.10 and has a resolution of $512x512$ pixel. The small bright dots on the image are dust and other contaminant particles, which can not be removed by post-processing.

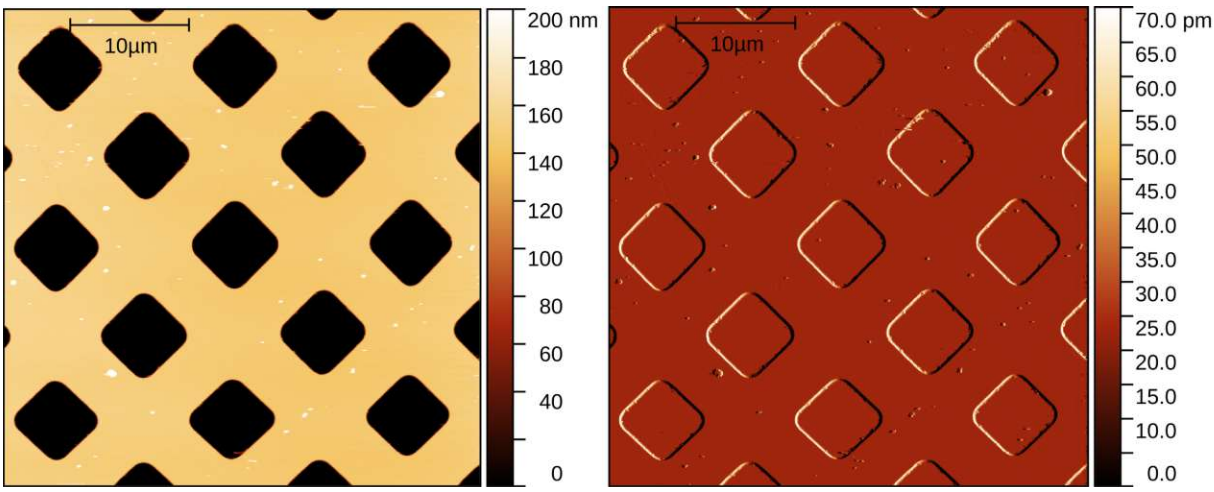

Figure 6.10: Platinum coated calibration grating, measured with the novel VG-TIA laser signal demodulation. The topography is shown on the left and the deflection measurement error on the right.

A zoom-in to one of the pits is shown in Fig. 6.11 where the same $512x512$ pixel resolution shows more details on the local step of the structure between the highest and the lowest point of the sample. The rounded corners of each pit induced by the etching process of the sample manufacturing are also clearly visible.

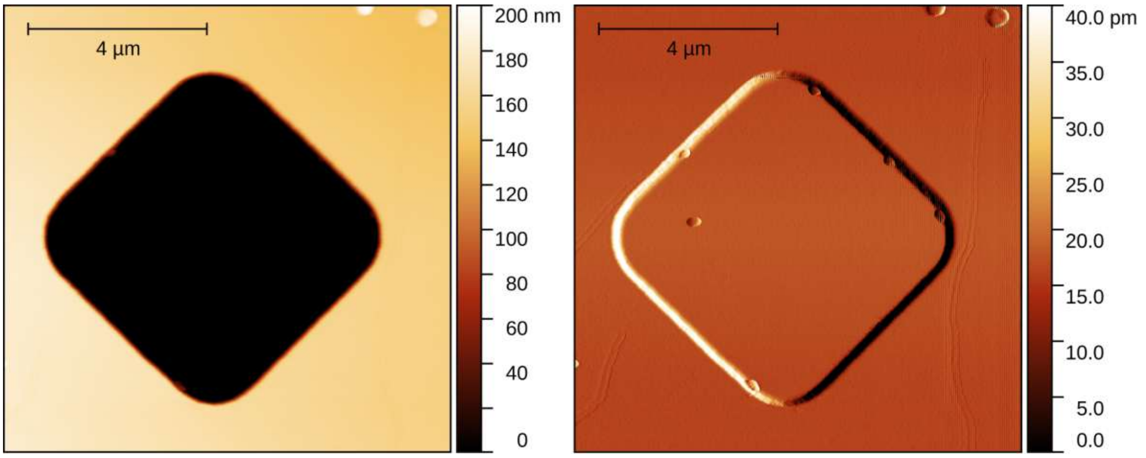

Figure 6.11: Zoomed-in measurement on one of the calibration grating pits, topography is shown on the left and the deflection measurement error on the right

6.2.2 Biological Sample Measurement

Biological samples are a widely used application for AFM measurements [83], two of which are shown in this section. The images have been acquired using the setup steps described above and can be used for comparison with other AFM setups and demodulation techniques.

Collagen Fibre

The measurement of a biological sample is shown in Fig. 6.12, where a collagen fibre is pictured. This fibrous protein is extracted from a rat tail and immobilised to the substrate. Each fibrils has a prominent periodicity pattern of 64 to 67nm called D-band periodicity [83]. The enlarged section in Fig. 6.13 is clearly showing those repeating structures and even the round nature of the element itself can be seen.

Deoxyribonucleic Acid (DNA)

It is often times highly interesting to image DNA with high resolution microscopy methods and due to its stability, DNA is even used as reference for AFM specification [2]. Due to the diameters in the order of single nanometers, other optical microscopes can not resolve it reliably. Measuring and displaying the helical structures of 1 to 2nm can be challenging and even minuscule deviation from the ideal setup, like a not perfectly sharp cantilever tip can result in a failed acquisition.

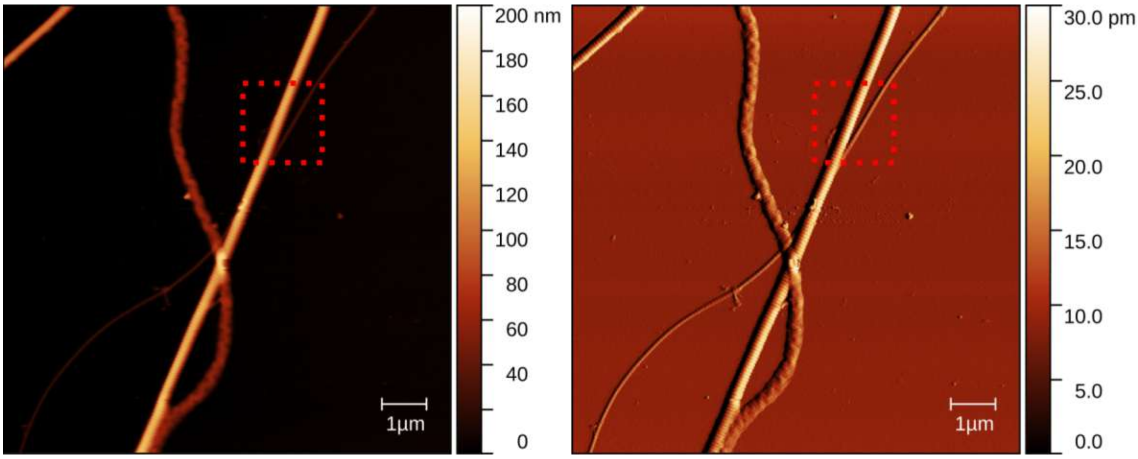

Figure 6.12: Collagen fibre with different strands measured with topography on the left and the deflection measurement error on the right with the enlarged section from Fig.6.13 marked in red.

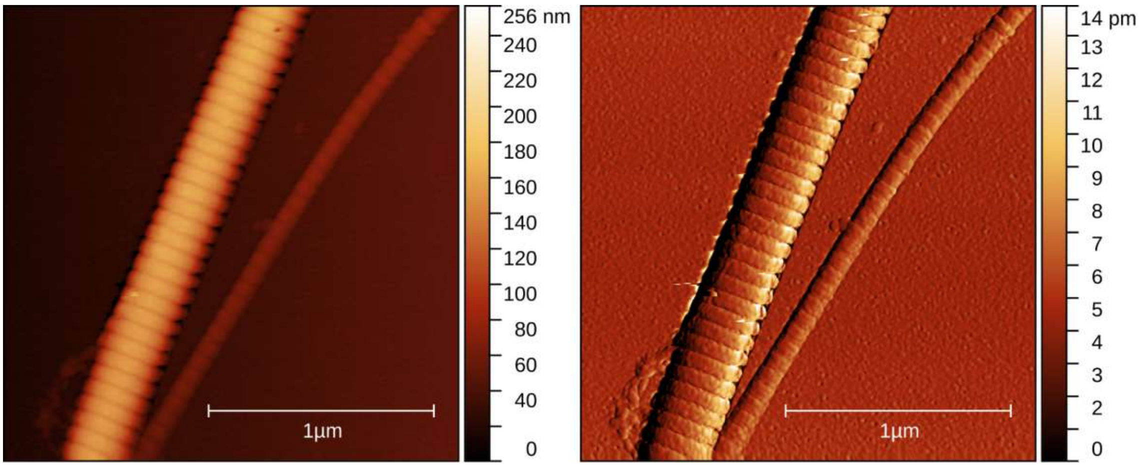

Figure 6.13: Enlarged image of a collagen fibre with D-band periodicity clearly showing on the left, deflection measurement error on the right.

Fig. 6.14 shows the strands of DNA and their structure with some the round and knotted structures marked with white arrows. A single piece of contamination is responsible for the highest point dimensioned at $13.7nm$ which visualises the amount of care and accuracy needed to record such an image. The structires are almost invilible in the deflection measurement error as the noise floor of the system is a limiting factor.

6.2.3 Evaluation Summary

In summary, the presented VG-TIA proves to be a viable alternative to the available lock-in amplifier to demodulate an OBD readout signal with a dynamic AFM measurement mode. The implemented system connects a custom laser driver with the analysed optical path to the QPD. A total of five VG-TIA implementations with two subtracting TIA

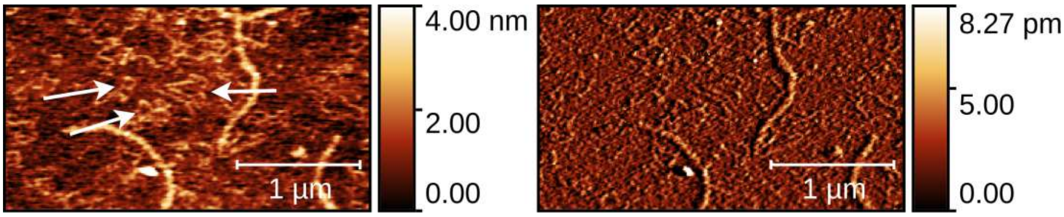

Figure 6.14: DNA image with some of the helical strands marked with white arrows and the deflection measurement error on the right.

circuits have been tested and evaluated against each other to be able to choose the best performing one. The presented sample measurements visualise these achievements with DNA being the most pithy with its regular usage as resolution reference for commercial AFM.

CHAPTER 7

Conclusion

With an increasing availability of high frequency cantilevers, facilitating a growing field of high speed AFM acquisition methods, the external demodulation of OBD readout signals after transimpedance amplification is an highly interesting topic for research. The need of expensive and bulky lock-in amplifiers can be a burden and simplification of the measurement setup yields possibilities for better sample topography recordings with higher resolution and lower noise.

The interaction forces between the cantilever tip and sample do not only result in an amplitude change, but also in phase changes, which can be measured and used to correct measurement errors caused by interfering forces like adhesion, spastic surface deformation or electrostatic interactions. Different cantilever deflection readout methods are explained and compared to each other in Chapter 2 as well as the available measurement modes and the demodulation theory.

The novel approach of integrating the demodulation into the TIA, by the means of a VG-TIA, the lock-in amplifier can be replaced by a simple low-pass filter, while getting the same benefits of it as compared to other demodulation techniques without the need of high sampling rate ADCs or other complicated additional elements. This novel idea including the necessary analysis of the elements interacting with the measurement path is explained in Chapter 3.

In the end a complete dissection and partial redesign of the measurement path was done, including the optical path consisting of laser driver, light path, cantilever reflection and QPD as well as the newly implemented VG-TIA with custom variable gain circuitry and on-board low-pass filter in Chapter 5. Five different VG-TIA are compared and the two with the overall most promising results are brought up for testing for which demodulation is possible up to $300kHz$. The best suited one is integrated into two subtraction VG-TIA circuits which in turn are tested and compared to culminate in the MOSFET based subtracting VG-TIA used for the measurements on real samples with gain differentials of over 130Ω. The remaining noise sources which can not be removed and are kept as small as possible through a combination of multiple known methods and design choices for best results.

A mechanical integration of the designed, manufactured, assembled and tested hardware is done on the existing AFM setup for evaluation and specification of the overall performance. The fully functional system is used for measurements of different biological and non-biological reference samples which is presented in Chapter 6. Measurements of DNA are presented as reference to other implementations with topographical feature sizes smaller than $4nm$.

In short, the idea of implementing a fully functional demodulation circuit directly into the TIA works and proves to be a viable alternative to demodulation via lock-in amplifier. The devised VG-TIA works well in conjunction with the also custom laser driver, low-pass and subtractor circuitries. Permanently adding such a system to existing AFM is possible and would save the need for external devices.

7.1 Outlook

This work proves the feasibility of a direct demodulation within the TIA, for which there still are possibilities for improvement and reevaluation with newly available parts.

Firstly, testing and evaluation of other methods to change the gain of a TIA without compromising the signal integrity as well as optimising the existing solutions for highest possible differential QPD output amplification would be a straight-forward option to broaden the project's possibilities. Secondly, the integration of an additional focusing lens, including a mechanical mount to quickly change the focus of the reflected light on the QPD, could reduce its size and increase the bandwidth. A third possible improvement could be achieved by adding the excitation waveform generator directly into the circuit for easier handling and shorter overall cable lengths reducing the noise coupled into the system from external sources.

Lastly, designing and manufacturing of a fully integrated circuit which includes one subtractor VG-TIA design would be the most complex but best suited implementation for commercialisation as well as improving noise and bandwidth specifications.

Bibliography

[1] G. Binnig, C. Quate, and C. Gerber, "Atomic force microscope," *Physical Review Letters*, vol. 56, no. 9, pp. 930–933, 1986, Cited by: 12926; All Open Access, Bronze Open Access.

[2] P. J. Kolbeck *et al.*, "Dna origami fiducial for accurate 3d atomic force microscopy imaging," *Nano Letters*, vol. 23, no. 4, pp. 1236–1243, 2023.

[3] R. W. Stark, "Dynamic force spectroscopy: Looking at the total harmonic distortion," in *Recent Advances in Multidisciplinary Applied Physics*, A. Mendez-Vilas, Ed., Oxford: Elsevier Science Ltd, 2005, pp. 427–431.

[4] Y. Xu, S. Smith, and P. Atherton, "A metrological scanning force microscope," *Precision engineering*, vol. 19, no. 1, pp. 46–55, 1996.

[5] E. K. Kosareva, A. N. Pivkina, and N. V. Muravyev, "Atomic force microscopy in energetic materials research: A review," *Energetic Materials Frontiers*, Jun. 2022.

[6] B. Drake *et al.*, "Imaging crystals, polymers, and processes in water with the atomic force microscope," *Science*, vol. 243, no. 4898, pp. 1586–1589, 1989.

[7] A. L. Weisenhorn *et al.*, "Imaging and manipulating molecules on a zeolite surface with an atomic force microscope," *Science*, vol. 247, no. 4948, pp. 1330–1333, 1990. eprint: https://www.science.org/doi/pdf/10.1126/science.247.4948.1330.

[8] F. J. Giessibl, "Advances in atomic force microscopy," *Rev. Mod. Phys.*, vol. 75, pp. 949–983, 3 Jul. 2003.

[9] N. Jalili and K. Laxminarayana, "A review of atomic force microscopy imaging systems: Application to molecular metrology and biological sciences," *Mechatronics*, vol. 14, no. 8, pp. 907–945, 2004.

[10] Y. Martin, C. C. Williams, and H. K. Wickramasinghe, "Atomic force microscope-force mapping and profiling on a sub 100-A scale," *Journal of Applied Physics*, vol. 61, no. 10, pp. 4723–4729, May 1987. eprint: https://pubs.aip.org/aip/jap/article-pdf/61/10/4723/7994030/4723_1_online.pdf.

[11] A. P. Nievergelt, S. H. Andany, J. D. Adams, M. T. Hannebelle, and G. E. Fantner, "Components for high-speed atomic force microscopy optimized for low phase-lag," in *2017 IEEE International Conference on Advanced Intelligent Mechatronics (AIM)*, IEEE, 2017, pp. 731–736.

[12] M. Salapaka, D. Chen, and J. Cleveland, "Stability and sensitivity analysis of periodic orbits in tapping mode atomic force microscopy," in *Proceedings of the 37th IEEE Conference on Decision and Control (Cat. No.98CH36171)*, vol. 2, 1998, 2047–2052 vol.2.

[13] C. A. J. Putman, K. O. Van der Werf, B. G. De Grooth, N. F. Van Hulst, and J. Greve, "Tapping mode atomic force microscopy in liquid," *Applied Physics Letters*, vol. 64, no. 18, pp. 2454–2456, May 1994. eprint: https://pubs.aip.org/aip/apl/article-pdf/64/18/2454/10165209/2454_1_online.pdf.

[14] M. G. Ruppert, D. M. Harcombe, M. R. P. Ragazzon, S. O. R. Moheimani, and A. J. Fleming, "A review of demodulation techniques for amplitude-modulation atomic force microscopy," *Beilstein Journal of Nanotechnology*, vol. 8, pp. 1407–1426, 2017.

[15] W. C. Michels and N. L. Curtis, "A Pentode Lock-In Amplifier of High Frequency Selectivity," *Review of Scientific Instruments*, vol. 12, no. 9, pp. 444–447, Dec. 2004. eprint: https://pubs.aip.org/aip/rsi/article-pdf/12/9/444/8331403/444_1_online.pdf.

[16] M. Ayat, M. A. Karami, S. Mirzakuchaki, and A. Beheshti-Shirazi, "Design of multiple modulated frequency lock-in amplifier for tapping-mode atomic force microscopy systems," *IEEE Transactions on Instrumentation and Measurement*, vol. 65, no. 10, pp. 2284–2292, 2016.

[17] J.-J. Vandenbussche, P. Lee, and J. Peuteman, "On the accuracy of digital phase sensitive detectors implemented in fpga technology," *IEEE Transactions on Instrumentation and Measurement*, vol. 63, no. 8, pp. 1926–1936, 2014.

[18] T. Sulchek, R. Hsieh, J. D. Adams, S. C. Minne, C. F. Quate, and D. M. Adderton, "High-speed atomic force microscopy in liquid," *Review of Scientific Instruments*, vol. 71, no. 5, pp. 2097–2099, May 2000. eprint: https://pubs.aip.org/aip/rsi/article-pdf/71/5/2097/11237053/2097_1_online.pdf.

[19] A. A. Baker, W. Helbert, J. Sugiyama, and M. J. Miles, "High-resolution atomic force microscopy of nativevaloniacellulose i microcrystals," *Journal of Structural Biology*, vol. 119, no. 2, pp. 129–138, 1997.

[20] F. Moreno-Herrero, J. Colchero, J. Gómez-Herrero, and A. M. Baró, "Atomic force microscopy contact, tapping, and jumping modes for imaging biological samples in liquids," *Phys. Rev. E*, vol. 69, p. 031 915, 3 Mar. 2004.

[21] Q. Zhong, D. Inniss, K. Kjoller, and V. Elings, “Fractured polymer/silica fiber surface studied by tapping mode atomic force microscopy,” *Surface Science*, vol. 290, no. 1, pp. L688–L692, 1993.

[22] G. Binnig and H. Rohrer, “The scanning tunneling microscope,” *Scientific American*, vol. 253, no. 2, pp. 50–58, 1985.

[23] T. Fukuma, M. Kimura, K. Kobayashi, K. Matsushige, and H. Yamada, “Development of low noise cantilever deflection sensor for multienvironment frequency-modulation atomic force microscopy,” *Review of Scientific Instruments*, vol. 76, no. 5, 2005.

[24] M. Dukic, J. D. Adams, and G. E. Fantner, “Piezoresistive afm cantilevers surpassing standard optical beam deflection in low noise topography imaging,” *Scientific reports*, vol. 5, no. 1, p. 16 393, 2015.

[25] R. D. Grober *et al.*, “Fundamental limits to force detection using quartz tuning forks,” *Review of Scientific Instruments*, vol. 71, no. 7, pp. 2776–2780, Jul. 2000. eprint: https://pubs.aip.org/aip/rsi/article-pdf/71/7/2776/11301233/2776_1_online.pdf.

[26] H. I. Rasool, P. R. Wilkinson, A. Z. Stieg, and J. K. Gimzewski, “A low noise all-fiber interferometer for high resolution frequency modulated atomic force microscopy imaging in liquids,” *Review of Scientific Instruments*, vol. 81, no. 2, 2010.

[27] Y. Shiba, T. Ono, K. Minami, and M. Esashi, “Capacitive afm probe for high speed imaging,” *IEEJ Transactions on Sensors and Micromachines*, vol. 118, no. 12, pp. 647–651, 1998.

[28] J. Brugger, R. Buser, and N. Rooij, “Micromachined atomic force microprobe with integrated capacitive read-out,” *Journal of Micromechanics and Microengineering*, vol. 2, Sep. 1992.

[29] K. A. Brown, B. H. Yang, and R. M. Westervelt, “Self-driving capacitive cantilevers for high-frequency atomic force microscopy,” *Applied Physics Letters*, vol. 100, no. 5, p. 053 110, Jan. 2012. eprint: https://pubs.aip.org/aip/apl/article-pdf/doi/10.1063/1.3679684/14252260/053110_1_online.pdf.

[30] B. Hoogenboom *et al.*, “A fabry–perot interferometer for micrometer-sized cantilevers,” *Applied Physics Letters*, vol. 86, no. 7, 2005.

[31] G. Meyer and N. M. Amer, “Novel optical approach to atomic force microscopy,” *Applied Physics Letters*, vol. 53, no. 12, pp. 1045–1047, Sep. 1988. eprint: https://pubs.aip.org/aip/apl/article-pdf/53/12/1045/7767041/1045_1_online.pdf.

[32] D. Kazantsev and E. Kazantzeva, “A four-segment photodiode cantilever-bending sensor for an atomic-force microscope,” *Instruments and Experimental Techniques*, vol. 57, pp. 631–639, 2014.

[33] E. Meyer, “Atomic force microscopy,” *Progress in Surface Science*, vol. 41, no. 1, pp. 3–49, 1992.

[34] R. Enning, D. Ziegler, A. Nievergelt, R. Friedlos, K. Venkataramani, and A. Stemmer, "A high frequency sensor for optical beam deflection atomic force microscopy," *Review of Scientific Instruments*, vol. 82, no. 4, p. 043 705, Apr. 2011. eprint: https://pubs.aip.org/aip/rsi/article-pdf/doi/10.1063/1.3575322/13460995/043705_1_online.pdf.

[35] P. J. Eaton and P. West, *Atomic Force Microscopy*. Oxford ; New York: Oxford University Press, 2010.

[36] R. Jagtap and A. Ambre, "Overview literature on atomic force microscopy (afm): Basics and its important applications for polymer characterization," 2006.

[37] R. Asmatulu and W. S. Khan, "Chapter 13 - characterization of electrospun nanofibers," in *Synthesis and Applications of Electrospun Nanofibers*, ser. Micro and Nano Technologies, R. Asmatulu and W. S. Khan, Eds., Elsevier, 2019, pp. 257–281.

[38] R. Garcia and R. Perez, "Dynamic atomic force microscopy methods," *Surface Science Reports*, vol. 47, no. 6, pp. 197–301, 2002.

[39] R. Garcıa and A. San Paulo, "Attractive and repulsive tip-sample interaction regimes in tapping-mode atomic force microscopy," *Phys. Rev. B*, vol. 60, pp. 4961–4967, 7 Aug. 1999.

[40] T. Fukuma, "Wideband low-noise optical beam deflection sensor with photothermal excitation for liquid-environment atomic force microscopy," *Review of Scientific Instruments*, vol. 80, no. 2, 2009.

[41] B. O. Alunda, L. O. Otieno, M. Chepkoech, C. C. Byeon, and Y. J. Lee, "Comparative study of trans-linear and trans-impedance readout circuits for optical beam deflection sensors in atomic force microscopy," *Journal of the Korean Physical Society*, vol. 74, pp. 88–93, 2019.

[42] J. H. Scofield, "Frequency-domain description of a lock-in amplifier," *American Journal of Physics*, vol. 62, no. 2, pp. 129–133, Feb. 1994. eprint: https://pubs.aip.org/aapt/ajp/article-pdf/62/2/129/11441741/129_1_online.pdf.

[43] I. Schlesinger, K. Kuchuk, and U. Sivan, "An ultra-low noise optical head for liquid environment atomic force microscopy," *Review of Scientific Instruments*, vol. 86, no. 8, 2015.

[44] S. Rode *et al.*, "Modification of a commercial atomic force microscopy for low-noise, high-resolution frequency-modulation imaging in liquid environment," *Review of Scientific Instruments*, vol. 82, no. 7, 2011.

[45] J. Steininger, M. Bibl, H. W. Yoo, and G. Schitter, "High bandwidth deflection readout for atomic force microscopes," *Review of Scientific Instruments*, vol. 86, no. 10, 2015.

[46] H. Mahmoodi Nasrabadi, M. Mahdavi, M. Soleymaniha, and S. Moheimani, "High resolution atomic force microscopy with an active piezoelectric microcantilever," *Review of Scientific Instruments*, vol. 93, no. 7, 2022.

[47] B. Gilbert, "Translinear circuits: A proposed classification," *Electronics letters*, vol. 1, no. 11, pp. 14–16, 1975.

[48] H.-U. Krotil, T. Stifter, and O. Marti, "Lock-in technique for concurrent measurement of adhesion and friction with the scanning force microscope," *Review of Scientific Instruments*, vol. 72, no. 1, pp. 150–156, Jan. 2001. eprint: https://pubs.aip.org/aip/rsi/article-pdf/72/1/150/11047874/150_1_online.pdf.

[49] A. V. Ermakov and E. L. Garfunkel, "A novel AFM/STM/SEM system," *Review of Scientific Instruments*, vol. 65, no. 9, pp. 2853–2854, Sep. 1994. eprint: https://pubs.aip.org/aip/rsi/article-pdf/65/9/2853/8806610/2853_1_online.pdf.

[50] G. Li, M. Zhou, F. He, and L. Lin, "A novel algorithm combining oversampling and digital lock-in amplifier of high speed and precision," *Review of Scientific Instruments*, vol. 82, no. 9, p. 095 106, Sep. 2011. eprint: https://pubs.aip.org/aip/rsi/article-pdf/doi/10.1063/1.3633943/16093724/095106_1_online.pdf.

[51] B. Derjaguin, V. Muller, and Y. Toporov, "Effect of contact deformations on the adhesion of particles," *Journal of Colloid and Interface Science*, vol. 53, no. 2, pp. 314–326, 1975.

[52] A. Payami Golhin, A. Cavaleiro, and M. Evaristo, "Improvement of the tribological performance of wscf coatings under dry and lubricated conditions," Ph.D. dissertation, Jul. 2019.

[53] N. L. PEDERSEN, "Design of cantilever probes for atomic force microscopy (afm)," *Engineering Optimization*, vol. 32, no. 3, pp. 373–392, 2000. eprint: https://doi.org/10.1080/03052150008941305.

[54] *Triangular silicon nitride cantilever*, SCANASYST-AIR, $70kHz$, Bruker AFM Probes, Mar. 2023.

[55] C. Maragliano, A. Glia, M. Stefancich, and M. Chiesa, "Effective afm cantilever tip size: Methods for in-situ determination," *Measurement Science and Technology*, vol. 26, no. 1, p. 015 002, 2014.

[56] M. Stark, C. Möller, D. J. Müller, and R. Guckenberger, "From images to interactions: High-resolution phase imaging in tapping-mode atomic force microscopy," *Biophysical Journal*, vol. 80, no. 6, pp. 3009–3018, 2001.

[57] D. F. B. C. Monteiro, "Development of a high resolution position sensor for atomic force microscopy," Ph.D. dissertation, 2022.

[58] T. Wang and B. Erhman, "Compensate transimpedance amplifiers intuitively," *Texas Instrument Application Report*, 1993.

[59] K. EL KIRAT, I. BURTON, V. DUPRES, and Y. F. DUFRENE, "Sample preparation procedures for biological atomic force microscopy," *Journal of Microscopy*, vol. 218, no. 3, pp. 199–207, 2005. eprint: https://onlinelibrary.wiley.com/doi/pdf/10.1111/j.1365-2818.2005.01480.x.

[60] J. Leiro, M. Torhola, and K. Laajalehto, "The afm method in studies of muscovite mica and galena surfaces," *Journal of Physics and Chemistry of Solids*, vol. 100, pp. 40–44, 2017.

[61] N. Starostina and P. West, "Part ii: Sample preparation for afm particle characterization," *Probe Microscopy*, pp. 1–9, 2006.

[62] Y. L. Lyubchenko, "Preparation of dna and nucleoprotein samples for afm imaging," *Micron*, vol. 42, no. 2, pp. 196–206, 2011, Biological Specimen Preparation and Preservation for High Resolution Microscopies.

[63] N. Tadic and D. Gobovic, "A voltage-controlled resistor in cmos technology using bisection of the voltage range," *IEEE Transactions on Instrumentation and Measurement*, vol. 50, no. 6, pp. 1704–1710, 2001.

[64] G. Ferri, V. Stornelli, F. Parente, and G. Barile, "Full range analog wheatstone bridge-based automatic circuit for differential capacitance sensor evaluation," *International Journal of Circuit Theory and Applications*, vol. 45, Oct. 2016.

[65] P. Horowitz, W. Hill, and I. Robinson, *The art of electronics*. Cambridge university press Cambridge, 2015, vol. 3.

[66] L. Orozco, "Programmable-gain transimpedance amplifiers maximize dynamic range in spectroscopy systems," *Analog Dialogue*, vol. 47, no. 5, pp. 1–5, 2013.

[67] N. Tadic, "Resistive mirror-based voltage controlled resistor with generalized active devices," *IEEE transactions on instrumentation and measurement*, vol. 47, no. 2, pp. 587–591, 1998.

[68] A. Grekov *et al.*, "Parameter extraction procedure for high power sic jfet," in *2009 IEEE Energy Conversion Congress and Exposition*, IEEE, 2009, pp. 1466–1471.

[69] Z. Wang, "Novel linearisation technique for implementing large-signal mos tunable transconductor," *Electronics Letters*, vol. 2, no. 26, pp. 138–139, 1990.

[70] B. Denisov, "A photoresistor as a multifunctional optoelectronic element," *Journal of Communications Technology and Electronics*, vol. 52, pp. 478–481, 2007.

[71] A. Tadić, A. Reyes Borunda, and M. W. Ray, "Development of a voltage controlled resistor for use in a self-balancing resistance bridge," *Review of Scientific Instruments*, vol. 90, no. 12, p. 124 706, Dec. 2019. eprint: https://pubs.aip.org/aip/rsi/article-pdf/doi/10.1063/1.5119720/15706243/124706_1_online.pdf.

[72] R. Kassies, K. O. van der Werf, M. L. Bennink, and C. Otto, "Removing interference and optical feedback artifacts in atomic force microscopy measurements by application of high frequency laser current modulation," *Review of Scientific Instruments*, vol. 75, no. 3, pp. 689–693, Mar. 2004. eprint: https://pubs.aip.org/aip/rsi/article-pdf/75/3/689/19088225/689_1_online.pdf.

[73] Y. Zhao, Z. Tian, X. Feng, Z. Feng, X. Zhu, and Y. Zhou, "High-precision semiconductor laser current drive and temperature control system design," *Sensors*, vol. 22, no. 24, 2022.

[74] C. A. J. Putman, B. G. De Grooth, N. F. Van Hulst, and J. Greve, "A detailed analysis of the optical beam deflection technique for use in atomic force microscopy," *Journal of Applied Physics*, vol. 72, no. 1, pp. 6–12, Jul. 1992. eprint: https://pubs.aip.org/aip/jap/article-pdf/72/1/6/8025345/6_1_online.pdf.

[75] H. Sun, *Laser diode beam basics, manipulations and characterizations*. Springer Science & Business Media, 2012.

[76] M. Poik, M. Mayr, T. Hackl, and G. Schitter, "Mechatronic Demodulation for Dynamic Atomic Force Microscopy Measurement Modes," in *2022 IEEE International Instrumentation and Measurement Technology Conference (I2MTC)*, Ottawa, ON, Canada: IEEE, May 2022, pp. 1–6.

[77] T. R. Albrecht, P. Grütter, D. Horne, and D. Rugar, "Frequency modulation detection using high-q cantilevers for enhanced force microscope sensitivity," *Journal of applied physics*, vol. 69, no. 2, pp. 668–673, 1991.

[78] G. H. Buh and J. J. Kopanski, "Atomic force microscope laser illumination effects on a sample and its application for transient spectroscopy," *Applied Physics Letters*, vol. 83, no. 12, pp. 2486–2488, Sep. 2003. eprint: https://pubs.aip.org/aip/apl/article-pdf/83/12/2486/18581858/2486_1_online.pdf.

[79] H. Alaibakhsh and M. A. Karami, "A new analytical pinned photodiode capacitance model," *IEEE Electron Device Letters*, vol. 39, no. 3, pp. 379–382, 2018.

[80] *Opa3s2859, dual-channel, 900-mhz, 2.2-nv/sqrt(hz), programmable gain transimpedance amplifier*, OPA3S2859-EP, Rev. B, Texas Instruments Incorporated, Apr. 2021.

[81] *Smpj177tr jfet p-channel 30v low noise*, SMPJ177TR, Rev. A01, InterFET Corporation, Nov. 2023.

[82] *Smpj109tr jfet n-channel -25v low noise*, SMPJ109TR, Rev. 00, InterFET Corporation, Jun. 2019.

[83] A. Stylianou, "Assessing collagen d-band periodicity with atomic force microscopy," *Materials*, vol. 15, no. 4, p. 1608, 2022.

Appendix

1 Prototype schematics A

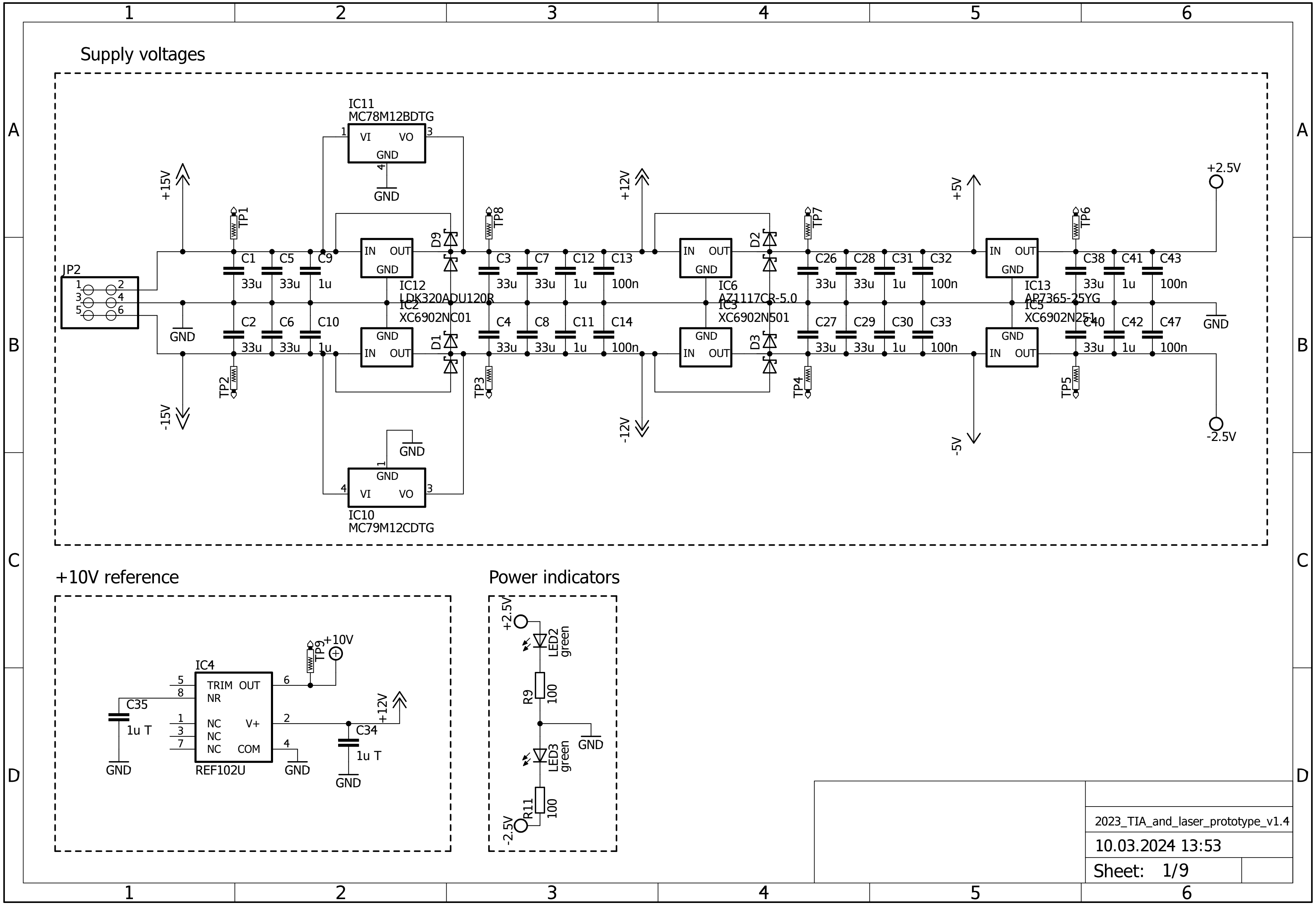
Supply voltages
IC11
MC78M12BDTG
IC10
MC79M12CDTG
IC12
LDK320ADU120R
IC2
XC6902NC01
IC6
AZ1117CR-5.0
IC3
XC6902N501
IC13
AP7365-25YG
IC5
XC6902N251
JP2
+15V
-15V
+12V
-12V
+5V
-5V
+2.5V
-2.5V
GND
+10V reference
IC4
REF102U
TRIM
OUT
NR
NC
V+
COM
C35
1u T
C34
TP9
+10V
Power indicators
LED2
green
LED3
green
R9
100
R11
100
2023_TIA_and_laser_prototype_v1.4
10.03.2024 13:53
Sheet: 1/9

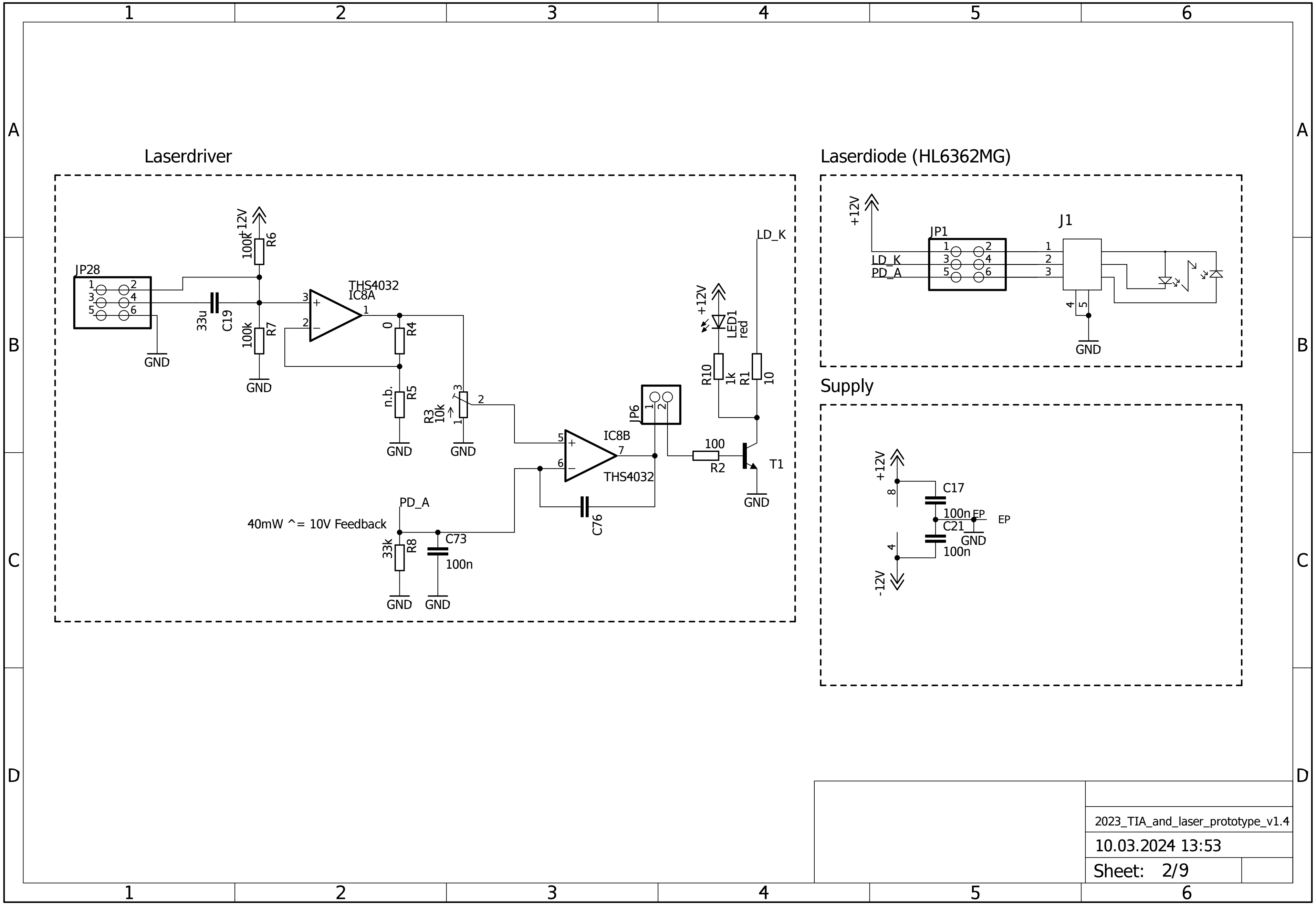
Laserdriver
Laserdiode (HL6362MG)
Supply
JP28
JP1
J1
JP6
THS4032
IC8A
IC8B
THS4032
+12V
-12V
100k R6
100k R7
33u C19
0 R4
n.b. R5
R3 10k
33k R8
C73 100n
C76
100 R2
T1
LED1 red
R10 1k
R1 10
LD_K
PD_A
40mW ^= 10V Feedback
C17 100n
C21 100n
EP
GND
2023_TIA_and_laser_prototype_v1.4
10.03.2024 13:53
Sheet: 2/9

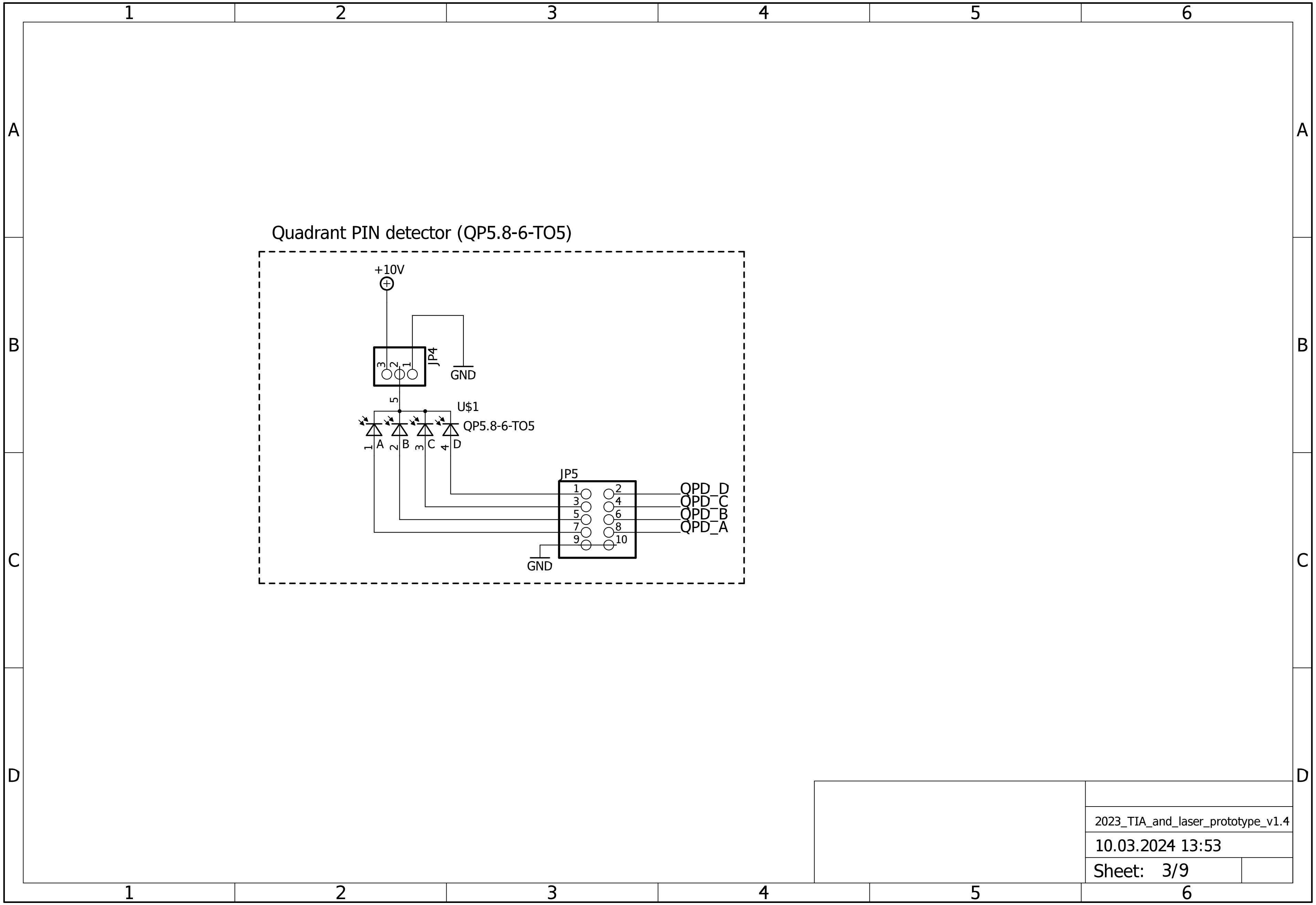
Quadrant PIN detector (QP5.8-6-TO5)
+10V
JP4
GND
U$1
QP5.8-6-TO5
JP5
QPD_D
QPD_C
QPD_B
QPD_A
GND
2023_TIA_and_laser_prototype_v1.4
10.03.2024 13:53
Sheet: 3/9

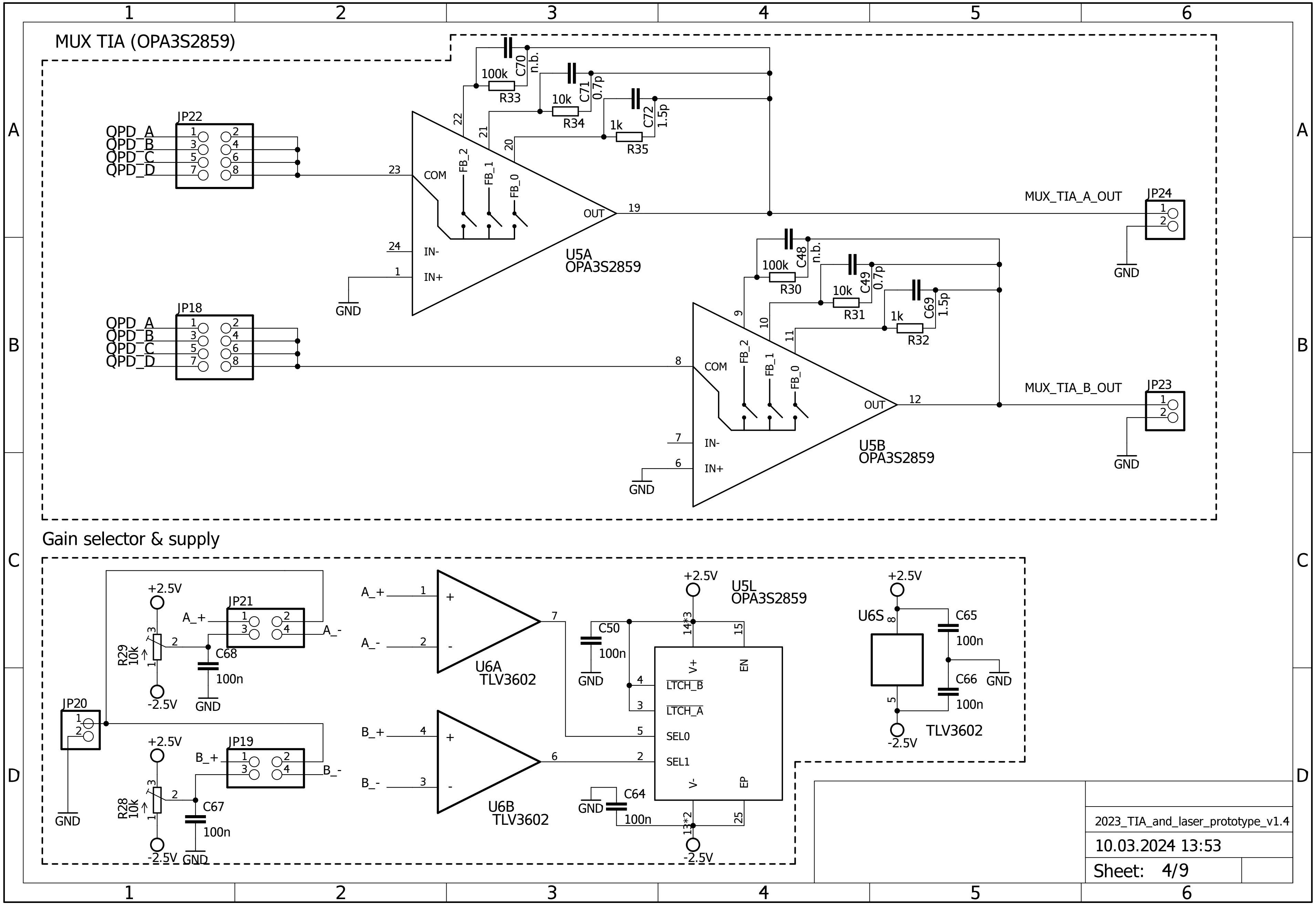

MUX TIA (OPA3S2859)
JP22
QPD_A
QPD_B
QPD_C
QPD_D
JP18
QPD_A
QPD_B
QPD_C
QPD_D
100k R33
C70 n.b.
10k R34
C71 0.7p
1k R35
C72 1.5p
COM
FB_2
FB_1
FB_0
OUT
IN-
IN+
GND
U5A OPA3S2859
MUX_TIA_A_OUT
JP24
100k R30
C48 n.b.
10k R31
C49 0.7p
1k R32
C69 1.5p
U5B OPA3S2859
MUX_TIA_B_OUT
JP23
Gain selector & supply
+2.5V
-2.5V
JP21
A_+
A_-
R29 10k
C68 100n
JP20
JP19
B_+
B_-
R28 10k
C67 100n
U6A TLV3602
U6B TLV3602
C50 100n
C64 100n
U5L OPA3S2859
V+
EN
LTCH_B
LTCH_A
SEL0
SEL1
V-
EP
U6S
C65 100n
C66 100n
TLV3602
2023_TIA_and_laser_prototype_v1.4
10.03.2024 13:53
Sheet: 4/9

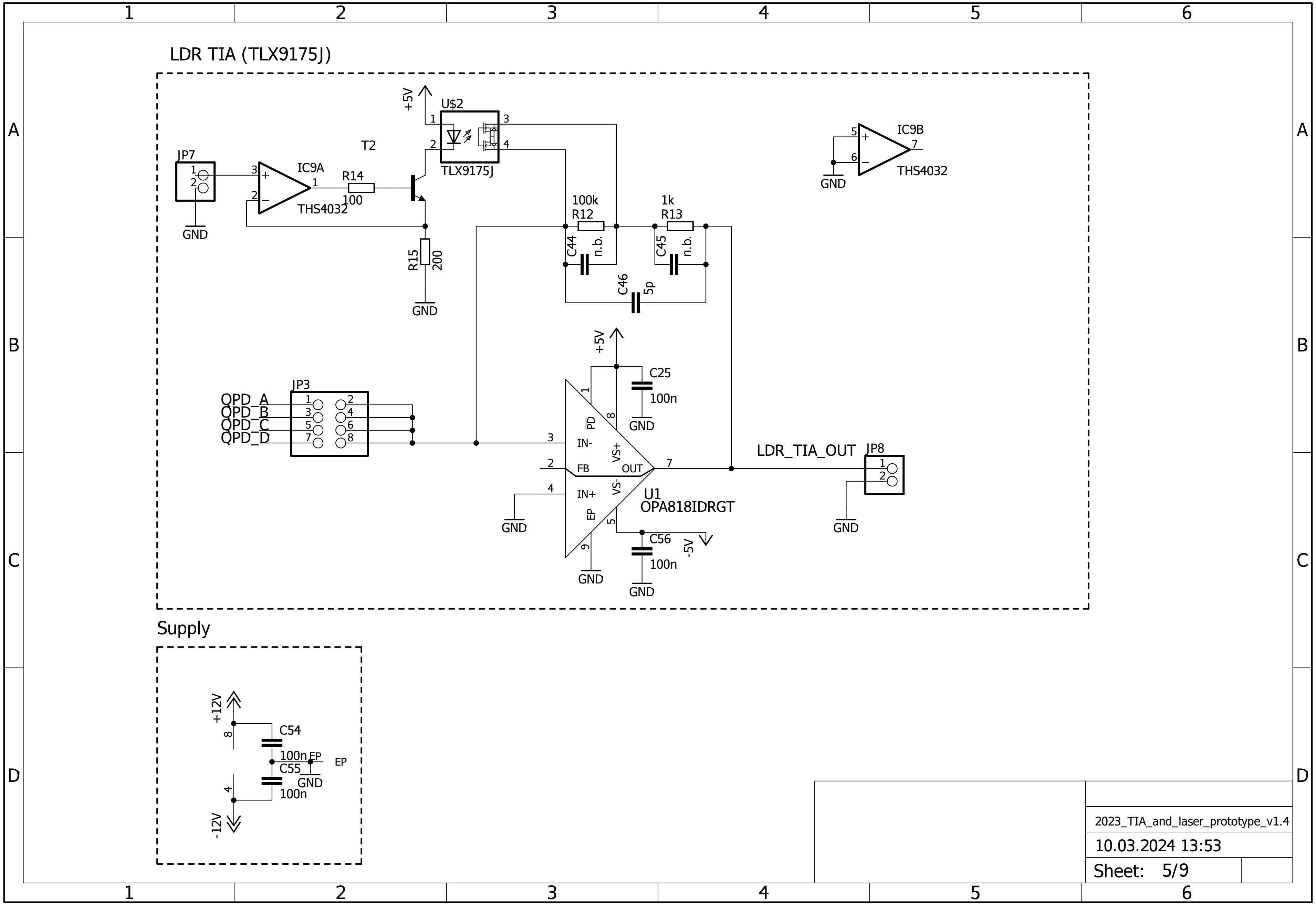

LDR TIA (TLX9175J)
U$2
TLX9175J
+5V
T2
JP7
IC9A
THS4032
R14
100
R15
200
GND
100k
R12
1k
R13
C44
n.b.
C45
n.b.
C46
5p
IC9B
THS4032
JP3
QPD_A
QPD_B
QPD_C
QPD_D
C25
100n
PD
IN-
FB
OUT
IN+
VS+
VS-
EP
U1
OPA818IDRGT
C56
100n
-5V
LDR_TIA_OUT
JP8
Supply
+12V
-12V
C54
100n
C55
100n
EP
2023_TIA_and_laser_prototype_v1.4
10.03.2024 13:53
Sheet: 5/9

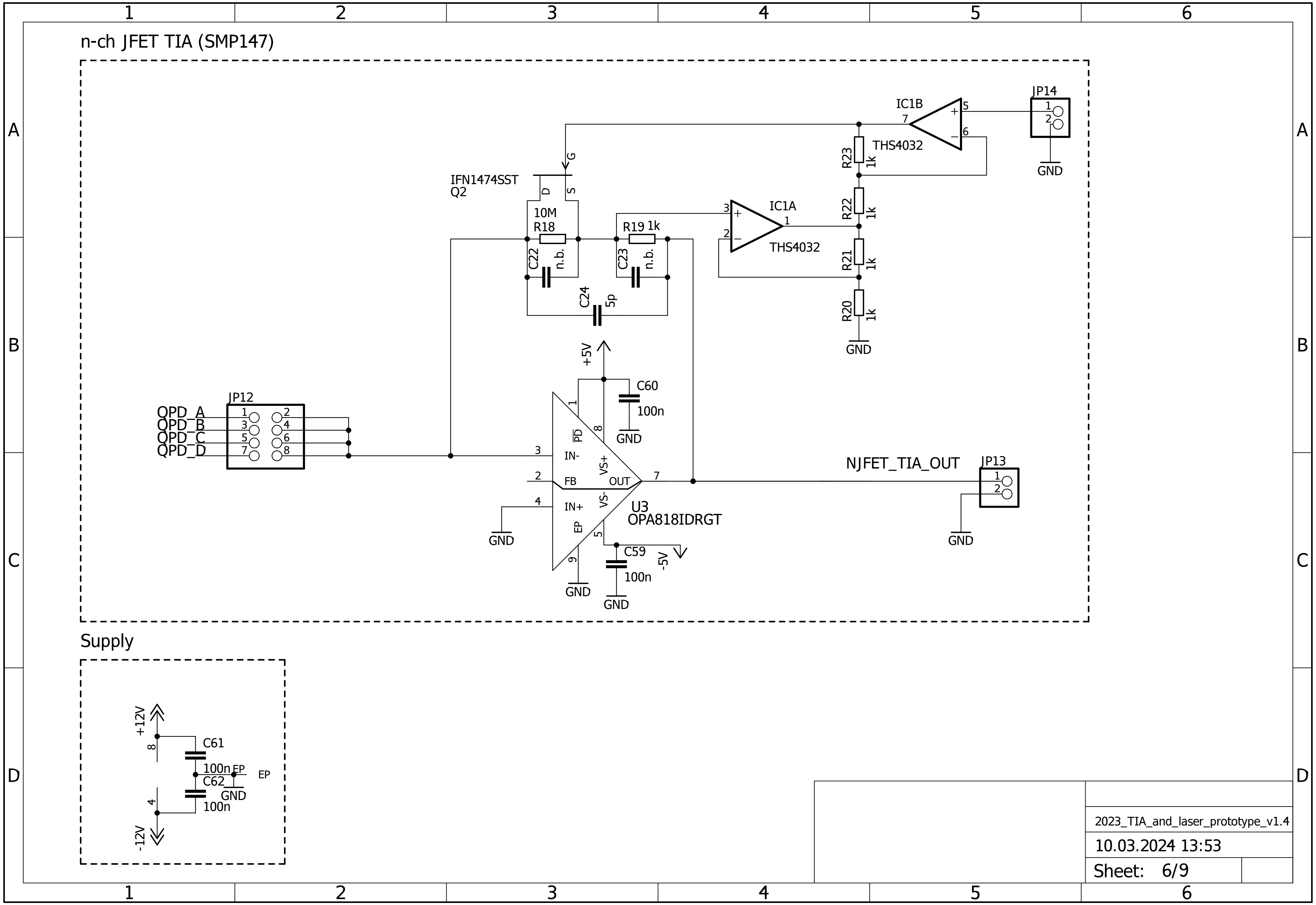

n-ch JFET TIA (SMP147)
IFN1474SST
Q2
G
D
S
10M
R18
R19 1k
C22
n.b.
C23
n.b.
C24
5p
IC1A
THS4032
IC1B
THS4032
R23 1k
R22 1k
R21 1k
R20 1k
GND
JP14
JP12
QPD_A
QPD_B
QPD_C
QPD_D
+5V
C60
100n
U3
OPA818IDRGT
IN-
FB
IN+
OUT
VS+
VS-
PD
EP
C59
100n
-5V
NJFET_TIA_OUT
JP13
Supply
+12V
-12V
C61
100n
C62
100n
EP
2023_TIA_and_laser_prototype_v1.4
10.03.2024 13:53
Sheet: 6/9

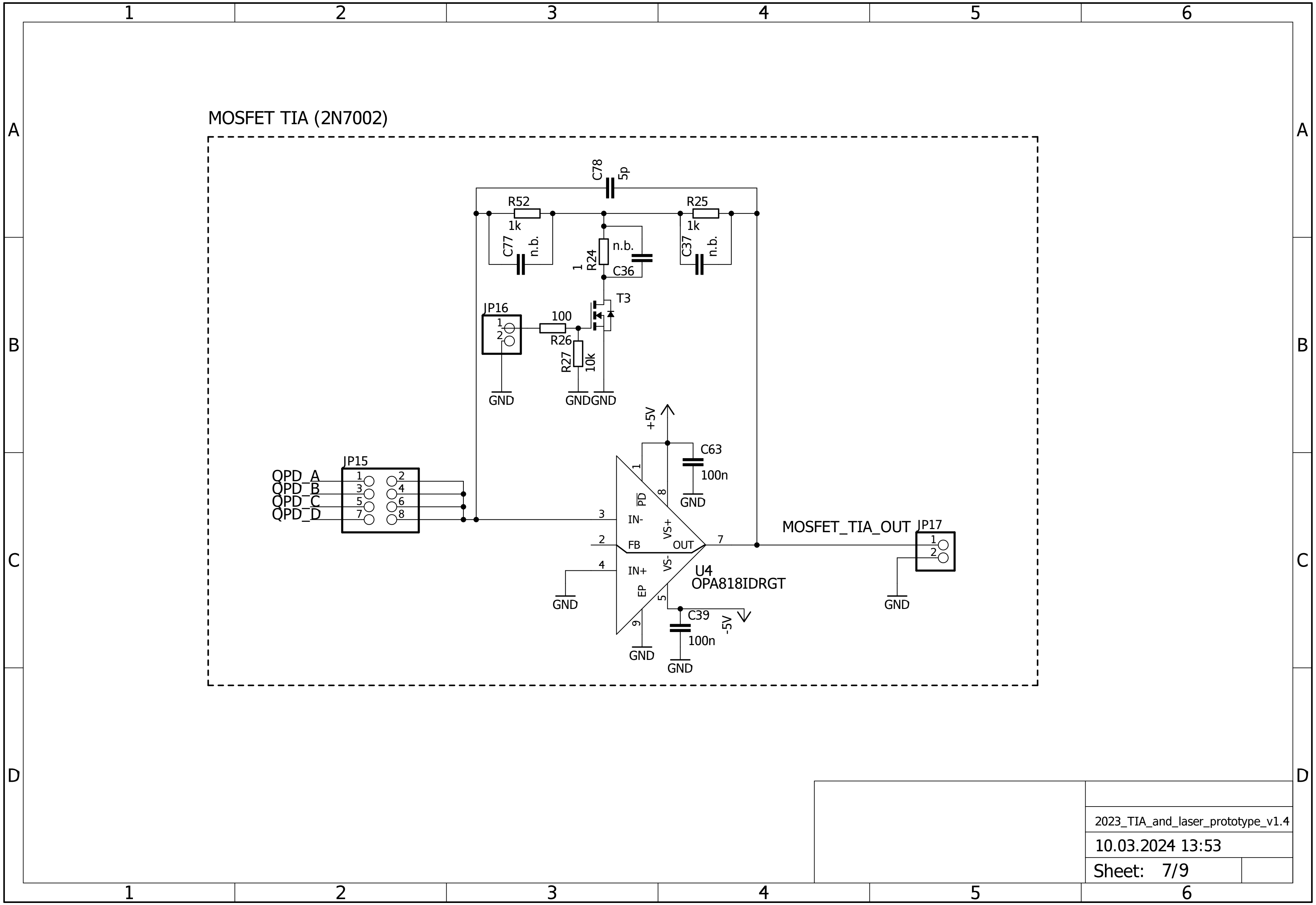
MOSFET TIA (2N7002)
C78
5p
R52
1k
C77
n.b.
R25
1k
C37
n.b.
R24
1
n.b.
C36
T3
JP16
100
R26
R27
10k
GND
GNDGND
+5V
C63
100n
JP15
QPD_A
QPD_B
QPD_C
QPD_D
IN-
FB
IN+
EP
PD
VS+
OUT
VS-
U4
OPA818IDRGT
MOSFET_TIA_OUT
JP17
C39
100n
-5V
2023_TIA_and_laser_prototype_v1.4
10.03.2024 13:53
Sheet: 7/9

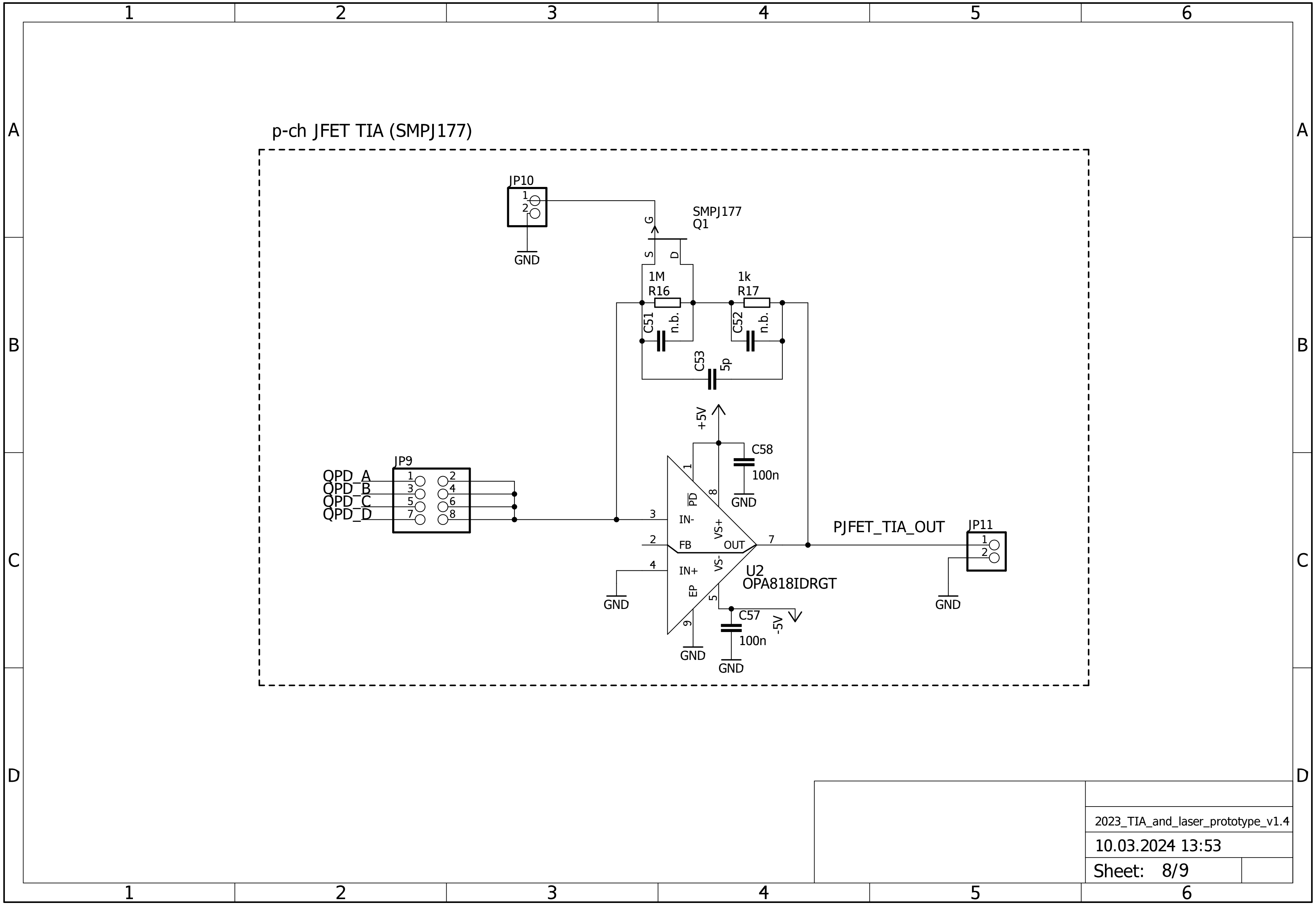

1
2
3
4
5
6
A
B
C
D
p-ch JFET TIA (SMPJ177)
JP10
GND
SMPJ177
Q1
G
S
D
1M
R16
1k
R17
C51
n.b.
C52
n.b.
C53
5p
+5V
C58
100n
GND
JP9
QPD_A
QPD_B
QPD_C
QPD_D
PD
IN-
FB
IN+
EP
VS+
VS-
OUT
U2
OPA818IDRGT
PJFET_TIA_OUT
JP11
GND
C57
100n
-5V
GND
2023_TIA_and_laser_prototype_v1.4
10.03.2024 13:53
Sheet: 8/9

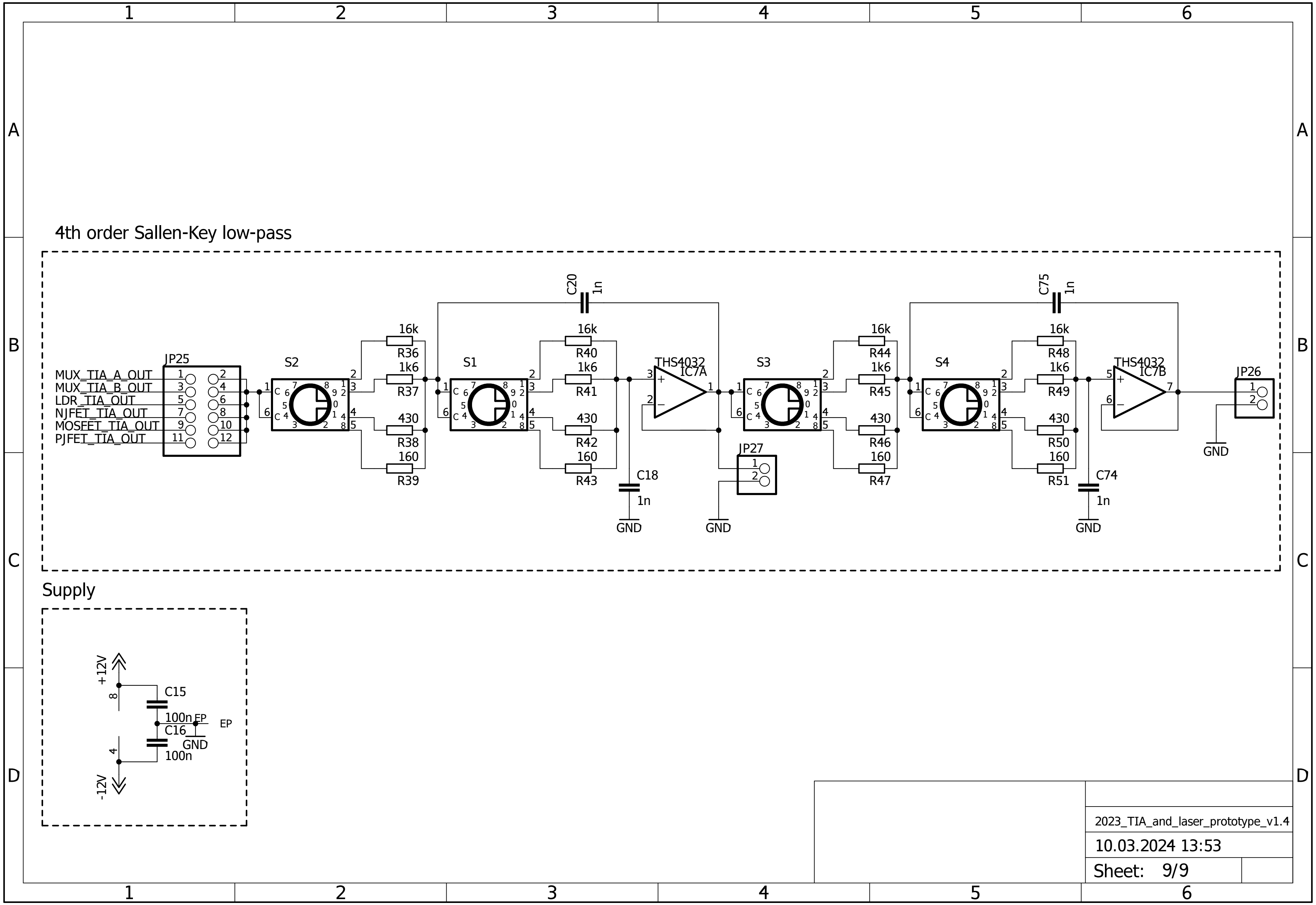
4th order Sallen-Key low-pass
MUX_TIA_A_OUT
MUX_TIA_B_OUT
LDR_TIA_OUT
NJFET_TIA_OUT
MOSFET_TIA_OUT
PJFET_TIA_OUT
JP25
S2
S1
S3
S4
16k
R36
1k6
R37
430
R38
160
R39
R40
R41
R42
R43
C20
1n
C18
C75
C74
THS4032
IC7A
IC7B
R44
R45
R46
R47
R48
R49
R50
R51
JP27
JP26
GND
Supply
+12V
-12V
C15
100n
C16
EP
2023_TIA_and_laser_prototype_v1.4
10.03.2024 13:53
Sheet: 9/9

2 Prototype schematics B

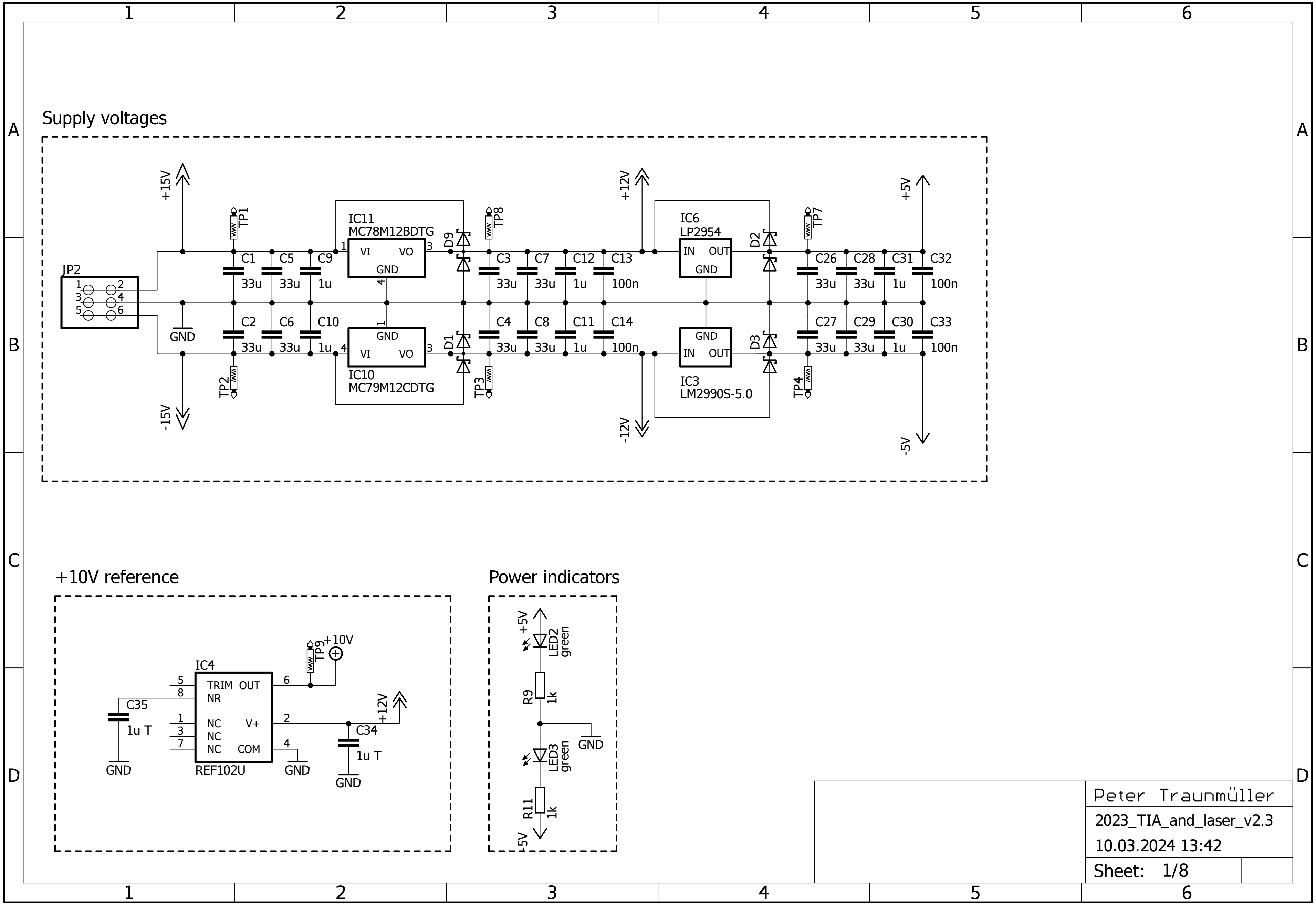
Supply voltages
+10V reference
Power indicators
JP2
IC11
MC78M12BDTG
IC10
MC79M12CDTG
IC6
LP2954
IC3
LM2990S-5.0
IC4
REF102U
TRIM OUT
NR
NC
V+
COM
+15V
-15V
+12V
-12V
+5V
-5V
+10V
GND
C1 33u
C2 33u
C5 33u
C6 33u
C9 1u
C10 1u
C3 33u
C4 33u
C7 33u
C8 33u
C12 1u
C11 1u
C13 100n
C14 100n
C26 33u
C27 33u
C28 33u
C29 33u
C31 1u
C30 1u
C32 100n
C33 100n
C35 1u T
C34 1u T
D9
D1
D2
D3
TP1
TP2
TP3
TP4
TP7
TP8
TP9
LED2 green
LED3 green
R9 1k
R11 1k
Peter Traunmüller
2023_TIA_and_laser_v2.3
10.03.2024 13:42
Sheet: 1/8

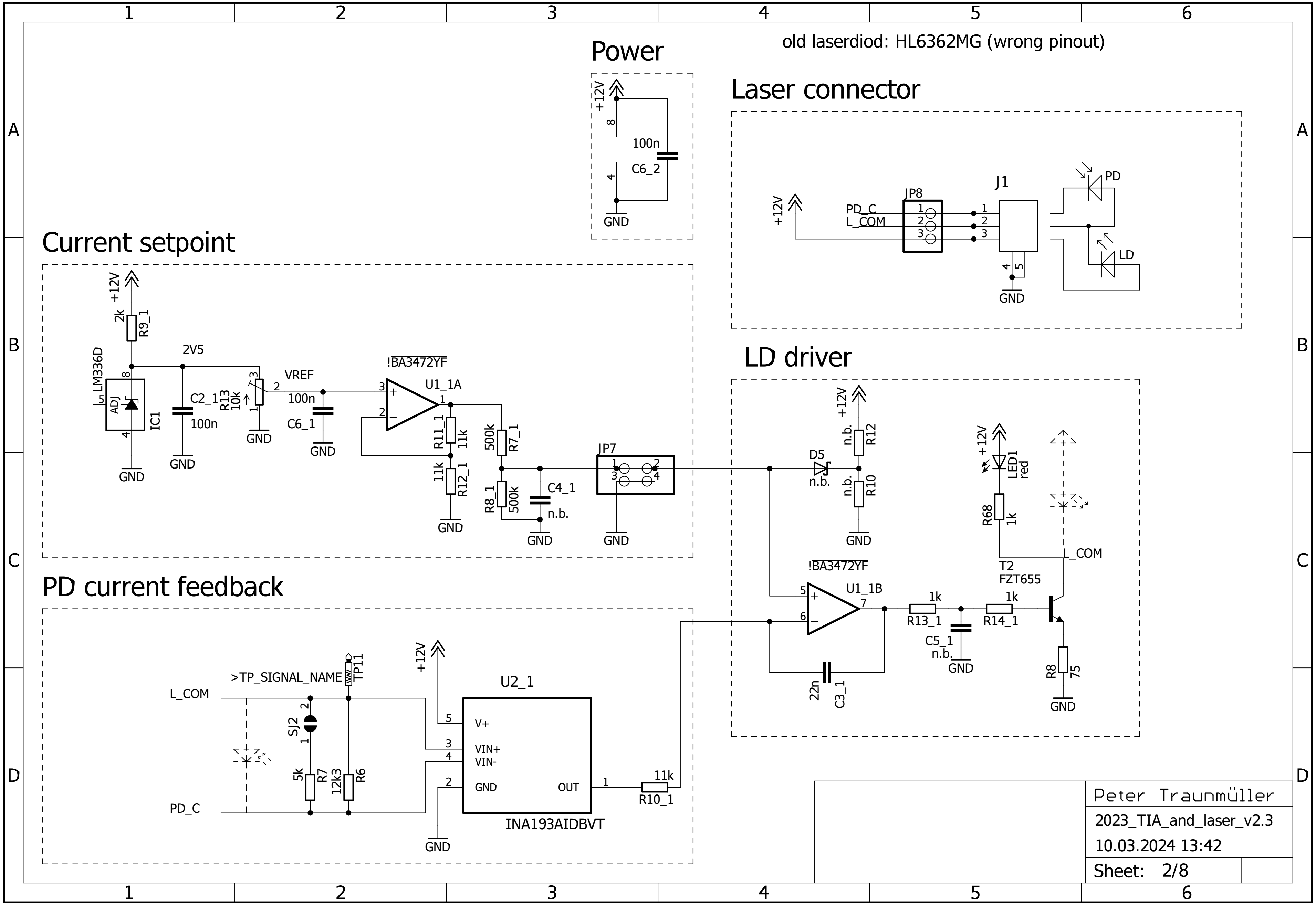

Power
old laserdiod: HL6362MG (wrong pinout)
Laser connector
Current setpoint
LD driver
PD current feedback
+12V
GND
100n
C6_2
PD_C
L_COM
JP8
J1
PD
LD
2V5
VREF
!BA3472YF
U1_1A
LM336D
IC1
ADJ
C2_1
100n
R13
10k
C6_1
2k
R9_1
R11_1
11k
R12_1
500k
R7_1
R8_1
C4_1
n.b.
JP7
D5
R12
R10
LED1
red
R68
1k
!BA3472YF
U1_1B
R13_1
R14_1
T2
FZT655
C5_1
22n
C3_1
R8
75
>TP_SIGNAL_NAME
TP11
SJ2
5k
R7
12k3
R6
U2_1
V+
VIN+
VIN-
OUT
INA193AIDBVT
R10_1
Peter Traunmüller
2023_TIA_and_laser_v2.3
10.03.2024 13:42
Sheet: 2/8

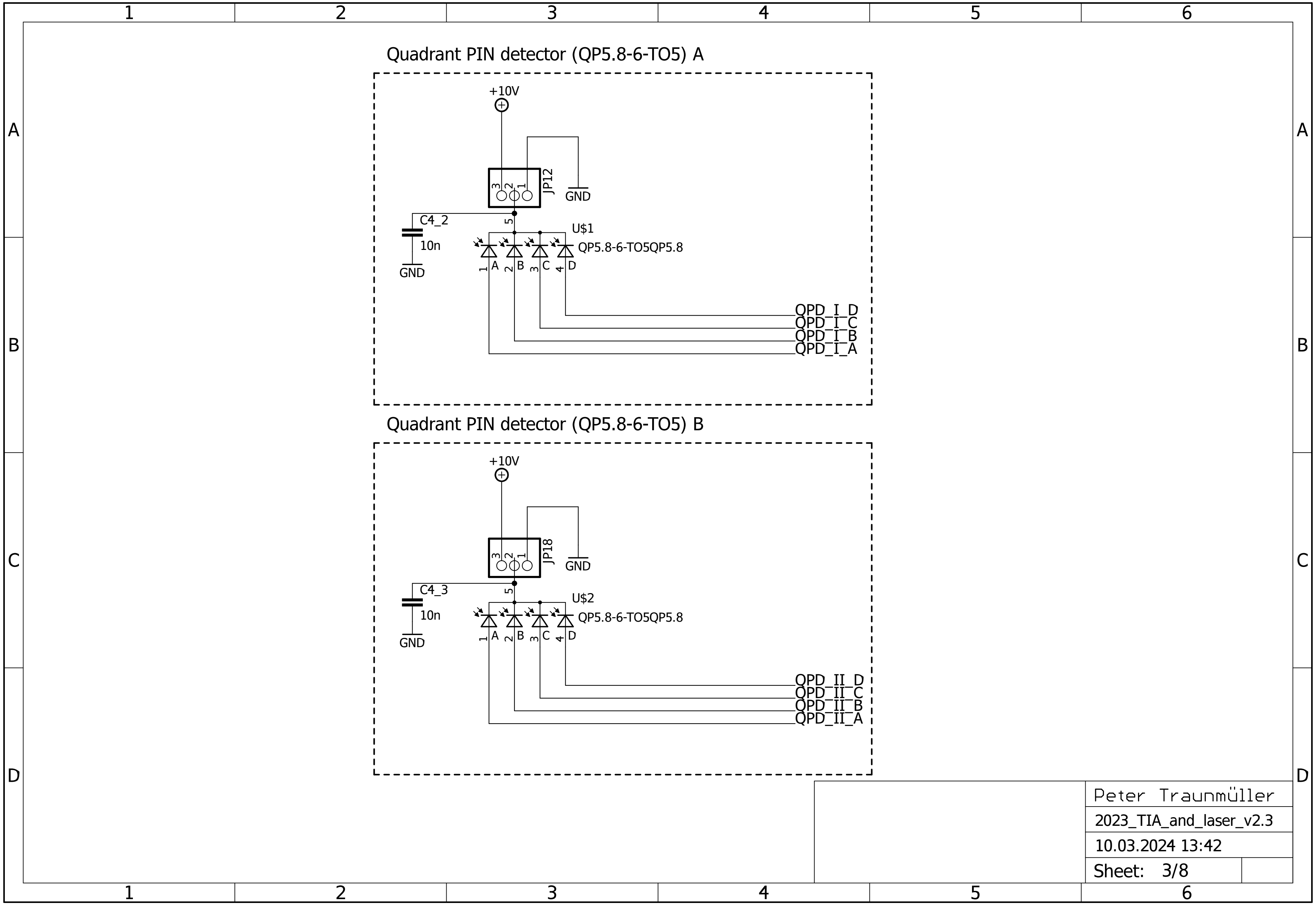
Quadrant PIN detector (QP5.8-6-TO5) A
+10V
JP12
GND
C4_2
10n
GND
U$1
QP5.8-6-TO5QP5.8
A
B
C
D
QPD_I_D
QPD_I_C
QPD_I_B
QPD_I_A
Quadrant PIN detector (QP5.8-6-TO5) B
+10V
JP18
GND
C4_3
10n
GND
U$2
QP5.8-6-TO5QP5.8
A
B
C
D
QPD_II_D
QPD_II_C
QPD_II_B
QPD_II_A
Peter Traunmüller
2023_TIA_and_laser_v2.3
10.03.2024 13:42
Sheet: 3/8

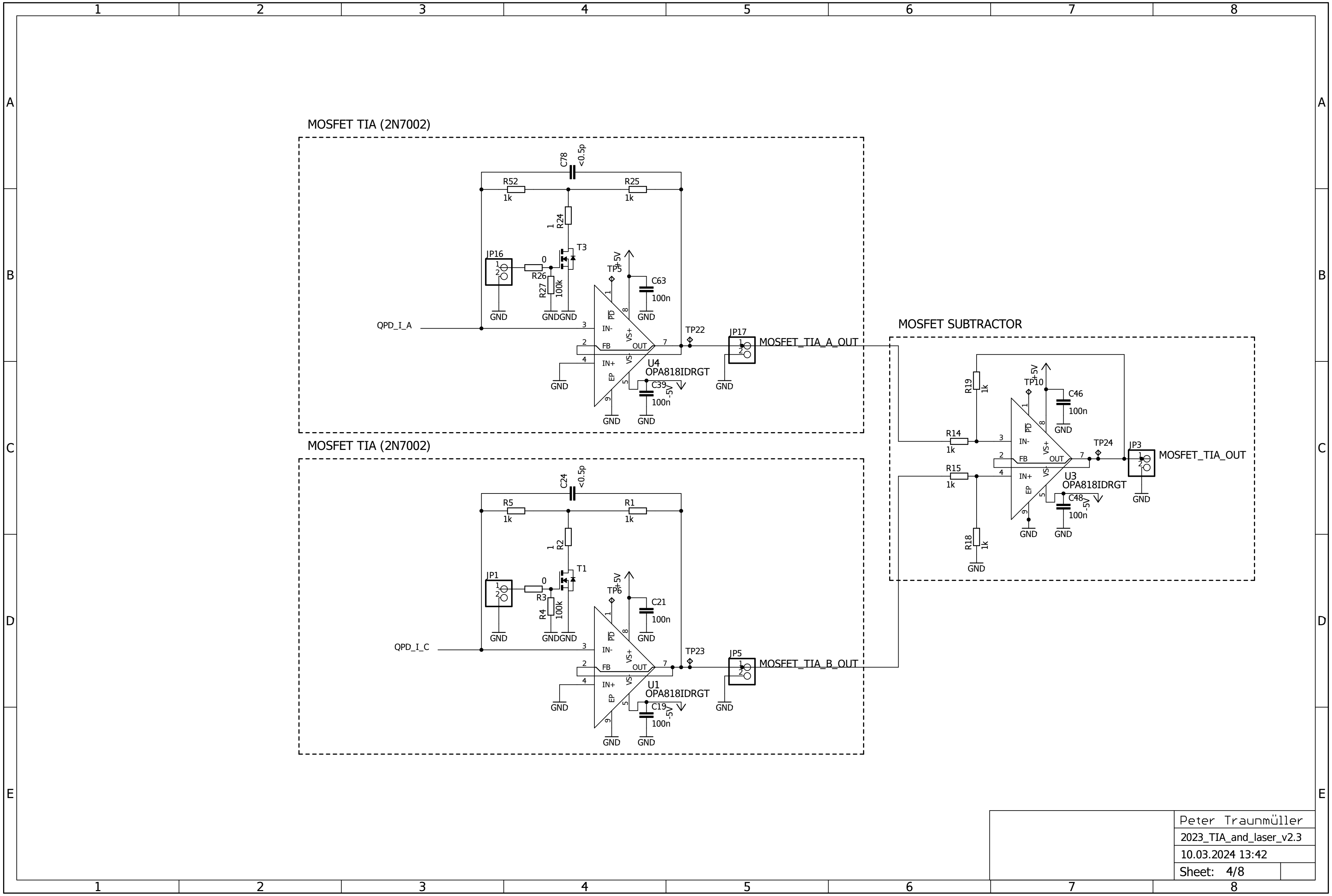
MOSFET TIA (2N7002)
MOSFET TIA (2N7002)
MOSFET SUBTRACTOR
QPD_I_A
QPD_I_C
MOSFET_TIA_A_OUT
MOSFET_TIA_B_OUT
MOSFET_TIA_OUT
C78 <0.5p
C24 <0.5p
R52 1k
R25 1k
R5 1k
R1 1k
R24 1
R2 1
T3
T1
JP16
JP1
JP17
JP5
JP3
R26 0
R3 0
R27 100k
R4 100k
TP5
TP6
TP10
TP22
TP23
TP24
C63 100n
C39 100n
C21 100n
C19 100n
C46 100n
C48 100n
U4 OPA818IDRGT
U1 OPA818IDRGT
U3 OPA818IDRGT
R19 1k
R14 1k
R15 1k
R18 1k
+5V
-5V
GND
Peter Traunmüller
2023_TIA_and_laser_v2.3
10.03.2024 13:42
Sheet: 4/8

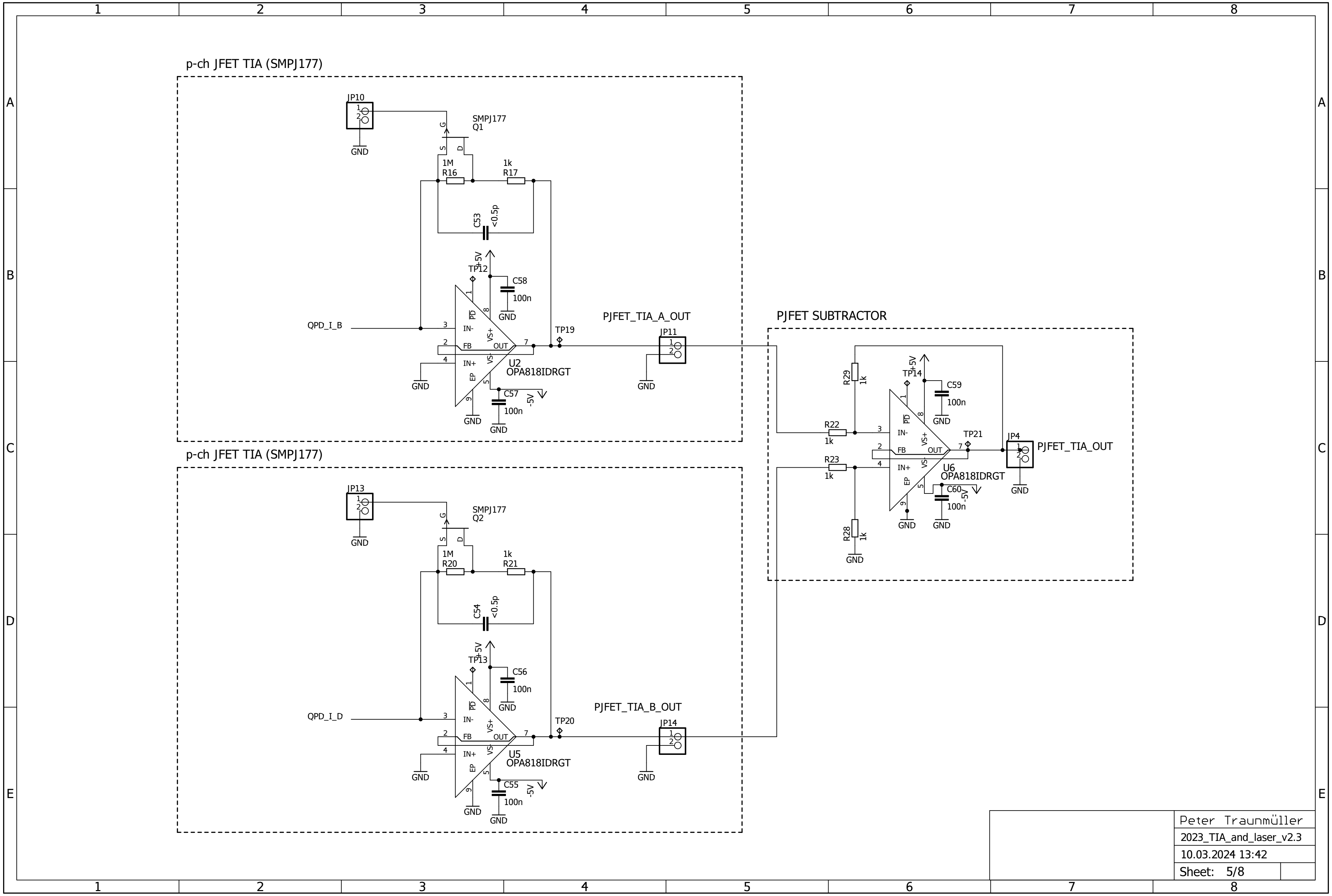
p-ch JFET TIA (SMPJ177)
JP10
SMPJ177
Q1
GND
1M
R16
1k
R17
C53
<0.5p
+5V
TP12
C58
100n
QPD_I_B
IN-
FB
OUT
IN+
EP
VS+
VS-
U2
OPA818IDRGT
C57
100n
-5V
TP19
PJFET_TIA_A_OUT
JP11
p-ch JFET TIA (SMPJ177)
JP13
SMPJ177
Q2
1M
R20
1k
R21
C54
<0.5p
TP13
C56
100n
QPD_I_D
U5
OPA818IDRGT
C55
100n
TP20
PJFET_TIA_B_OUT
JP14
PJFET SUBTRACTOR
R29
1k
TP14
C59
100n
R22
1k
R23
1k
TP21
JP4
PJFET_TIA_OUT
U6
OPA818IDRGT
C60
100n
R28
1k
Peter Traunmüller
2023_TIA_and_laser_v2.3
10.03.2024 13:42
Sheet: 5/8

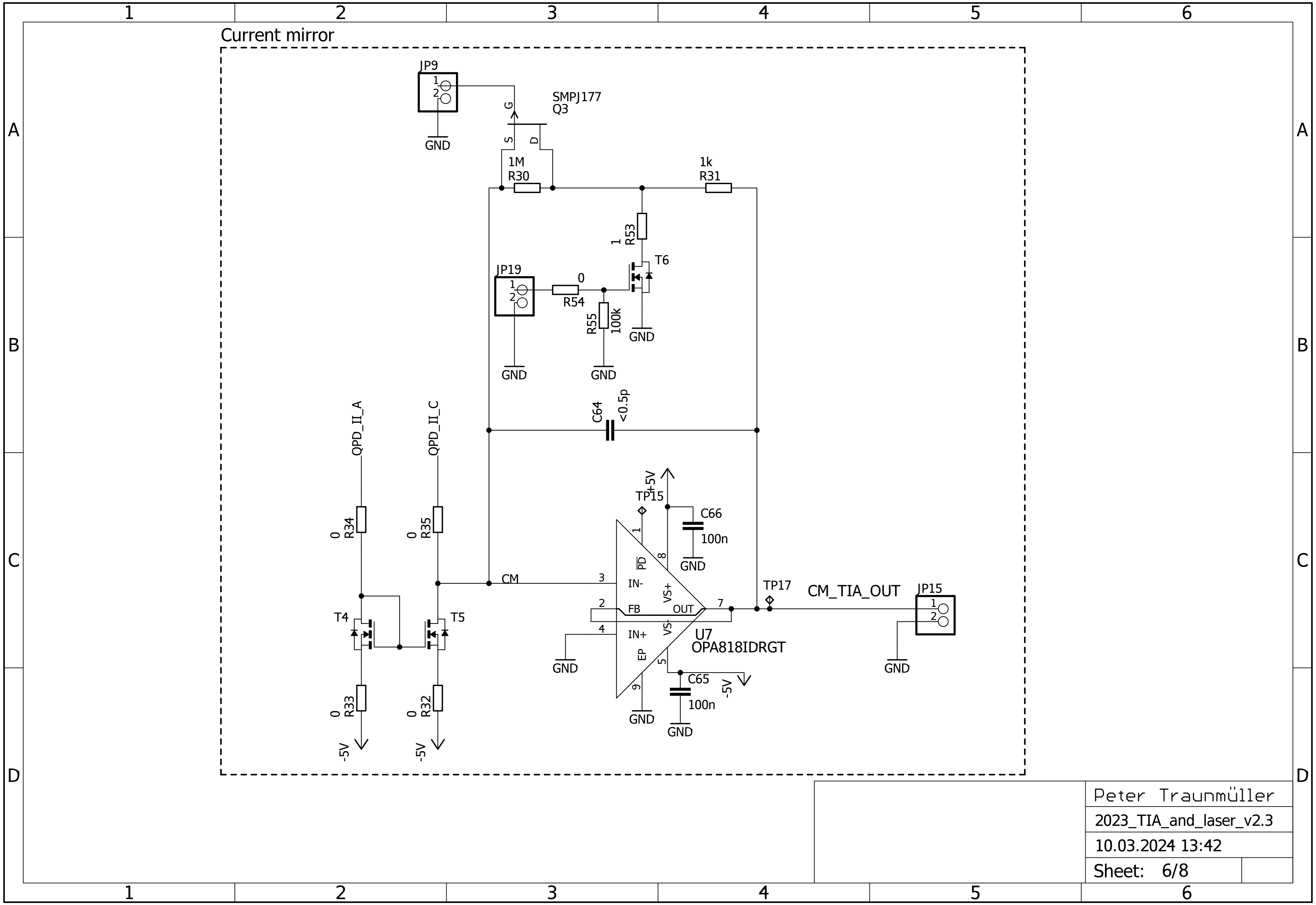
Current mirror
JP9
SMPJ177
Q3
G
S
D
GND
1M
R30
1k
R31
R53
1
T6
JP19
0
R54
R55
100k
GND
GND
GND
C64
<0.5p
QPD_II_A
QPD_II_C
+5V
TP15
C66
100n
GND
R34
0
R35
0
CM
IN-
FB
OUT
IN+
PD
VS+
VS-
EP
U7
OPA818IDRGT
TP17
CM_TIA_OUT
JP15
GND
GND
T4
T5
C65
100n
-5V
GND
GND
R33
0
R32
0
-5V
-5V
Peter Traunmüller
2023_TIA_and_laser_v2.3
10.03.2024 13:42
Sheet: 6/8

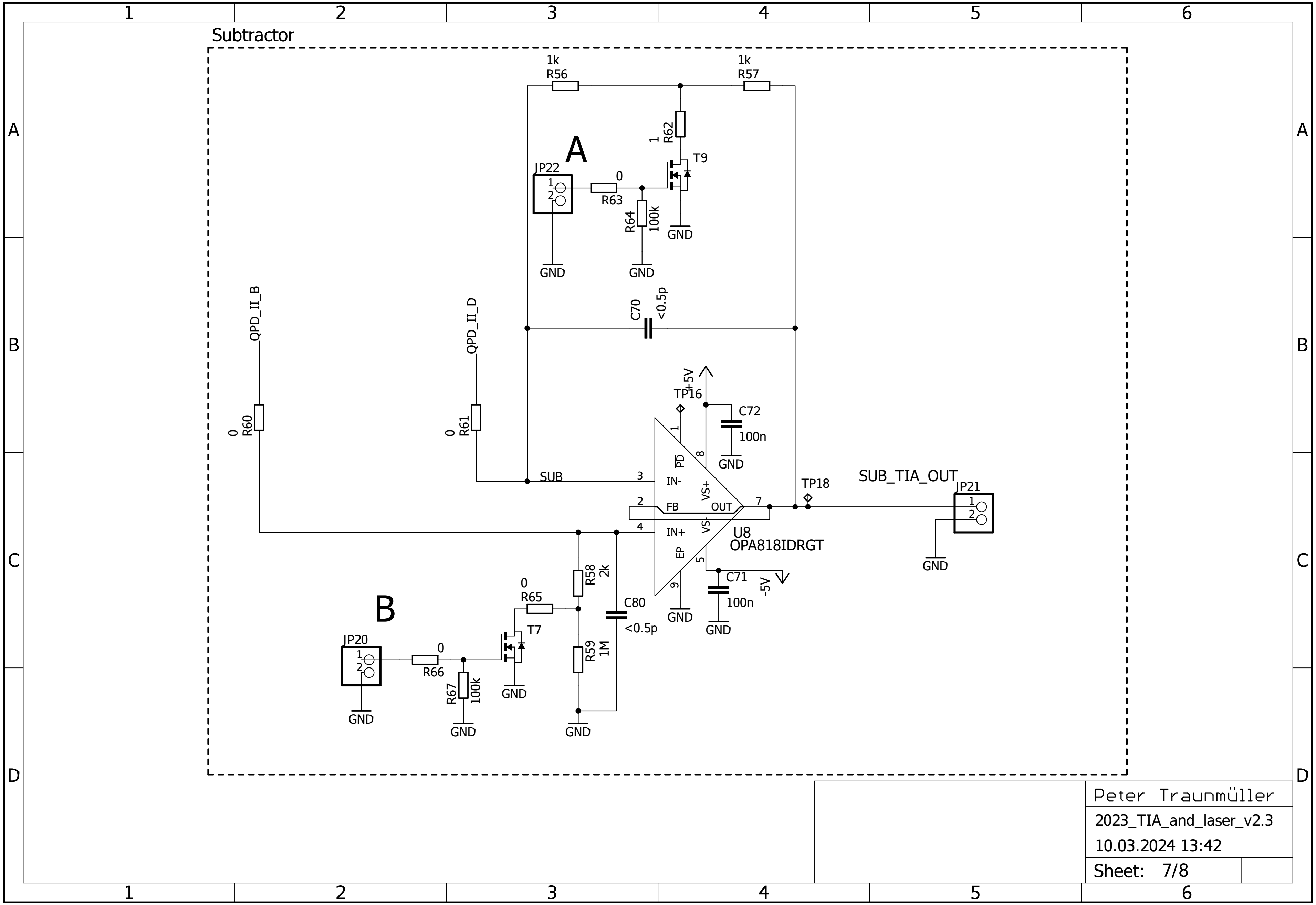
Subtractor
1k
R56
1k
R57
R62
1
T9
A
JP22
0
R63
R64
100k
GND
QPD_II_B
QPD_II_D
C70
<0.5p
+5V
TP16
C72
100n
R60
0
R61
0
SUB
IN-
FB
OUT
IN+
PD
VS+
VS-
EP
TP18
SUB_TIA_OUT
JP21
U8
OPA818IDRGT
R58
2k
C71
100n
-5V
C80
<0.5p
R59
1M
0
R65
T7
B
JP20
R66
R67
100k
Peter Traunmüller
2023_TIA_and_laser_v2.3
10.03.2024 13:42
Sheet: 7/8

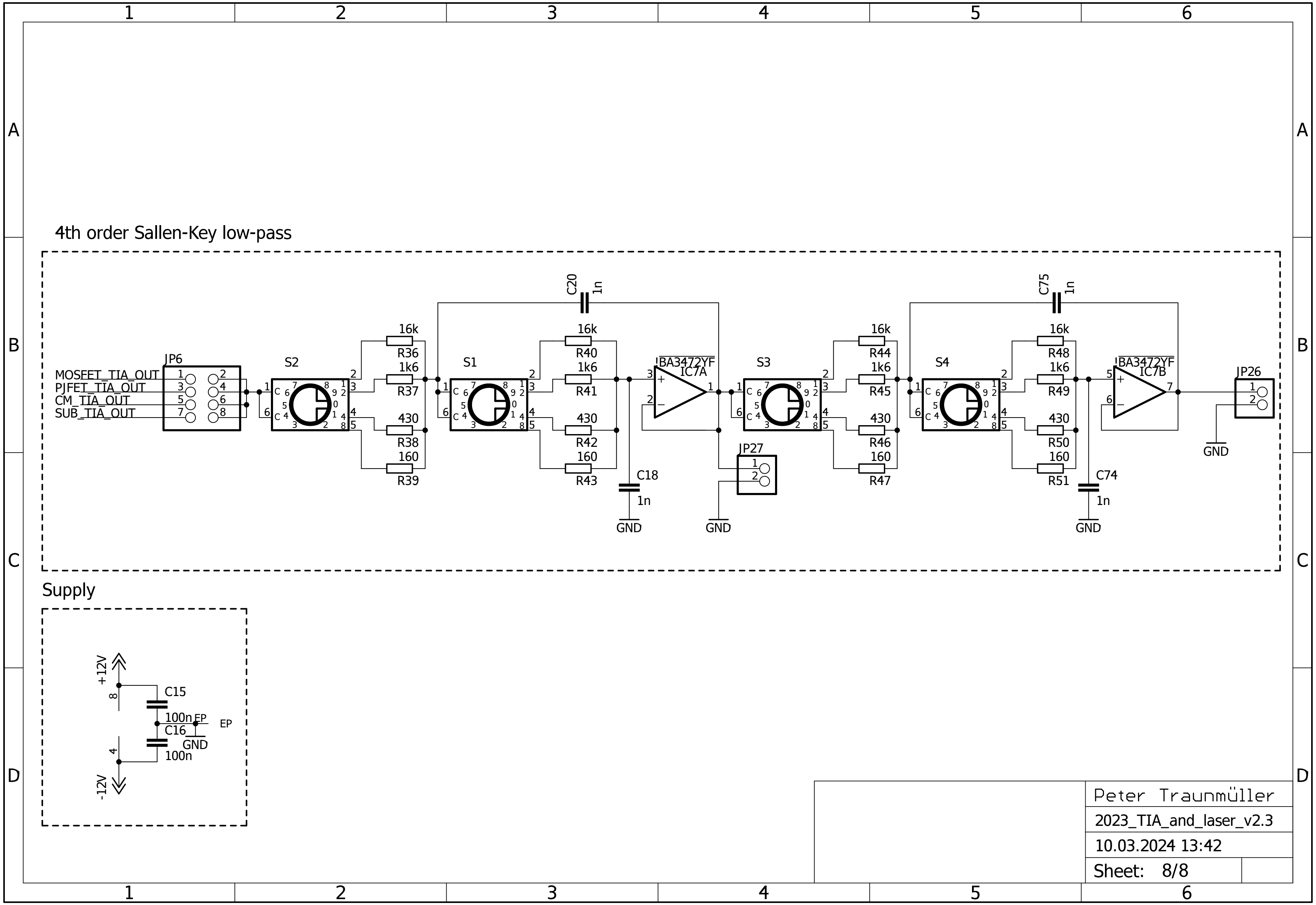
4th order Sallen-Key low-pass
MOSFET_TIA_OUT
PJFET_TIA_OUT
CM_TIA_OUT
SUB_TIA_OUT
JP6
S2
S1
S3
S4
16k R36
1k6 R37
430 R38
160 R39
16k R40
1k6 R41
430 R42
160 R43
16k R44
1k6 R45
430 R46
160 R47
16k R48
1k6 R49
430 R50
160 R51
C20 1n
C75 1n
C18 1n
C74 1n
BA3472YF IC7A
BA3472YF IC7B
JP27
JP26
GND
Supply
+12V
-12V
C15 100n
C16 100n
EP
GND
Peter Traunmüller
2023_TIA_and_laser_v2.3
10.03.2024 13:42
Sheet: 8/8

3 Eidesstattliche Erklärung

Ich erkläre an Eides statt, dass ich die vorliegende Arbeit selbstständig und ohne fremde Hilfe verfasst, andere als die angegebenen Quellen und Hilfsmittel nicht benutzt bzw. die wörtlich oder sinngemäß entnommenen Stellen als solche kenntlich gemacht habe. Zudem bestätige ich, dass keine künstliche Intelligenz (KI) für die Verfassung der Arbeit bzw. für Teile der Arbeit zum Einsatz gekommen ist.

Peter Traunmüller

Ort, Datum

4 Einverständniserklärung zur Plagiatsprüfung

Ich nehme zur Kenntnis, dass die vorgelegte Arbeit mit geeigneten und dem derzeitigen Stand der Technik entsprechenden Mitteln (Plagiat-Erkennungssoftware) elektronisch-technisch überprüft wird. Dies stellt einerseits sicher, dass bei der Erstellung der vorgelegten Arbeit die hohen Qualitätsvorgaben im Rahmen der ausgegebenen der an der TU Wien geltenden Regeln zur Sicherung guter wissenschaftlicher Praxis - "Code of Conduct" (Mitteilungsblatt 2007, 26. Stück, Nr. 257 idgF.) an der TU Wien eingehalten wurden. Zum anderen werden durch einen Abgleich mit anderen studentischen Abschlussarbeiten Verletzungen meines persönlichen Urheberrechts vermieden.

Peter Traunmüller

Ort, Datum